LES of a novel wing/body junction : Anti-fairing

Sampath Kumar R S

Supervisor
Dr. Richard Dwight
Associate Professor
Aerodynamics research group
TU Delft

LES of a novel wing/body junction : Anti-fairing

by

Sampath Kumar R S

to obtain the degree of Master of Science
at the Delft University of Technology,
to be defended publicly on September 26, 2019.

Student number:	4718879	
Project duration:	November, 2018 - September, 2019	
Thesis committee:	Dr. Richard P. Dwight,	TU Delft, supervisor
	Ir. Zeno Belligoli,	TU Delft, daily supervisor
	Prof. dr. -Ing Georg Eitelberg,	TU Delft, supervisor
	Prof. dr. Stefan Hickel,	TU Delft, Chair

TU Delft Delft University of Technology

Acknowledgement

First and foremost, I would like to dedicate my Masters degree to my dear grandfather who sadly passed away before I could finish my Masters. I love you *Thatha* and I'm sure that I always had (and will always have in the future) your blessings throughout my journey in these two years.

Now its time to thank a lot of people. The first thanks is obviously to my parents for their unconditional love and sacrifices. Throughout these two years, it was their everyday phone calls and constant words of support that made me survive the challenging times. I don't think I can express in words the gratitude I feel for everything they have done for me. I would also like to thank my other family members who were always sweet and encouraging to me.

Regarding my thesis, I would like to thank Dr. Richard Dwight, my thesis supervisor, for allowing me to work on this topic and also for guiding me throughout the thesis. Every meeting that I had with you was a learning experience for me and I would cherish them forever. I don't think I could have finished my thesis if not for my daily supervisor Ir. Zeno Belligoli. Whenever I hit any road blocks during my thesis, he was always there for me with his brilliant ideas and suggestions. I'm pretty sure I'll never get such a helpful and considerate supervisor in my professional career. Thanks for everything Zeno. I would like to extend my gratitude to Prof. dr. Stefan Hickel for allowing me to use his LES solver for my thesis and also providing timely help with the simulation setup. I also wish to express my thankfulness to Prof. dr Georg Eitelberg for his insightful comments regarding the results and also for conducting the green light meeting when Richard wasn't available.

Thanks to all the aerodynamics boys (Sid, Vishal, Kushal, Nikilesh, Abhinand, Nikhil, Ankit, Athreya, Shubham, Jatinder, Prayash, Kiran) for all the assignment discussions, random fluid mechanics discussions, games of connect, Italy trip, poker nights, etc. I will forever cherish those memories. And finally a big thanks to my 8th Horcrux gang (Prethvi, Shravan, Sasi, Sandy, Yamuna, Apoorva, Gowtham) for making the stay at van Hasseltlaan such a fun filled and memorable one. I will never forget the extremely long tea session talks, food get togethers, movie nights, Swiss trip, bomb squad games, etc. Special shout out to my wonderful roommate for two years, Prethvi, and Sasi for frequently treating me with authentic Indian food using their amazing culinary skills. Thinking back to two years ago, I never would have thought that my Masters journey would be such an enriching experience for me both academically and personally. I can say without doubt that the decision to come to TU Delft for Masters is one of the best decisions of my life. I look forward to how my future professional career pans out.

Sampath Kumar,
Delft, September 2019.

Abstract

Large Eddy Simulations (LES) of a novel type of wing/body junction called the anti-fairing are performed in the current thesis to study the complex turbulent flow physics involved in the junction area and also to obtain a clear understanding of the drag reduction capabilities of the anti-fairing. In regards to that, two separate LES are performed: one for the baseline case with a Rood wing/flat plate combination and another with the Rood wing/anti-fairing combination. A detailed comparative study is performed between the two cases to observe important differences in junction flow characteristics. Both the simulations are performed on a 25 million immersed boundary Cartesian mesh by solving the incompressible Navier-Stokes equations using the in-house finite volume LES solver called INCA. Results from the LES study confirms the existence of the propulsive pressure mechanism of drag reduction for the anti-fairing case, previously proposed by Belligoli *et al.* However, the results also show that there exists a secondary drag reduction mechanism caused by a combination of increase in approach boundary layer momentum thickness and dampening of the turbulence associated with the horseshoe vortex (HSV) upstream of the wing. This secondary mechanism has been found to be caused by the convex dent present at the start of the anti-fairing geometry. The total drag reduction for the anti-fairing case comes out to be 1.8%. A new parameter called junction drag is defined which accounts for the drag only due to the presence of a junction. The reduction in junction drag obtained for the anti-fairing case is about 6.8%. Apart from the LES analysis, a RANS analysis has also been performed to further investigate the drag reduction capabilities of anti-fairing for different approach boundary layer thicknesses and anti-fairing depths. All the RANS analysis have been performed on a 5 million body-fitted mesh by solving the incompressible Navier-Stokes using the open source finite-volume solver OpenFOAM. Results from the RANS analysis indicate that there exists an optimum depth for the anti-fairing which corresponds to the least drag. Furthermore, it is found that the effect of approach boundary layer thickness is mostly on changing the base drag of the case where no anti-fairing is present, rather than actually affecting the performance of the anti-fairing at different depths.

Contents

List of Figures

List of Tables

Nomenclature

α - Angle of attack (degrees)

BF - Bluntness factor (-)

δ - Boundary layer thickness (m)

δ^* - Boundary layer displacement thickness (m)

ρ_∞ - Density (kg/m^3)

c - Wing chord (m)

C_d - Drag coefficient (-)

C_p - Static pressure coefficient (-)

D - Drag force (N)

k - Turbulent kinetic energy (m^2/s^2)

MDF - Momentum Deficit Factor (-)

q_∞ - Freestream dynamic pressure (Pa)

Q - Q-criterion (s^-1)

Re - Reynolds number (-)

T - Maximum thickness of the wing (m)

θ - Boundary layer momentum thickness (m)

U_∞ - Freestream velocity (m/s)

U_{ref} - Reference velocity (here, equal to freestream velocity) (m/s)

u_τ - Friction velocity (m/s)

u_i' Fluctuating velocity component (m/s)

U - Streamwise velocity component (m/s)

u^+ - Non-dimensional velocity (-)

V - Vertical velocity component (m/s)

W - Spanwise velocity component (m/s)

ω - Vorticity (s^{-1})

X - Streamwise coordinate (m)

Y - Vertical coordinate (m)

y^+ - Non-dimensional wall distance (-)

Z - Spanwise coordinate (m)

1

Introduction

We encounter flow around protrusions very frequently in our daily lives. The situations range from flow around bridge supports to flow around wing/fuselage junction on an aircraft. These types of flows in which the boundary layer developing over a surface encounters an obstacle in its path are called junction flows. Junction flows are an important phenomenon to understand owing to their application in many engineering situations such as external aerodynamics, turbomachinery, submarines, electronic component cooling and river/bridge flows. Especially in the aerospace sector, this is a widely researched topic due to its involvement in the creation of a specific component of drag, called interference drag. This type of drag arises when air moving over two non-parallel surfaces intersect and mix together. The resultant mixing generates increased turbulence locally and causes increased drag.

The incoming fluid experiences a strong adverse pressure gradient due to the presence of the obstacle that triggers the separation of the boundary layer well before the position of the obstacle. This separation is three dimensional and results in complex recirculation zones and strong coherent vortical structures such as the horse-shoe vortices (HSV) [48]. These vortices are highly unsteady except for very low Reynolds number. They cause many undesirable effects such as high turbulence intensities, high surface pressure fluctuations, high heat transfer rates and erosion scour in the nose region of the obstacle [53]. Also,as mentioned above, this HSV is also responsible for the interference drag at the wing/fuselage junction. The subsequent pages of this chapter briefly explains the common flow features of the junction flows and the underlying flow physics involved.

1.1. Common flow features of the junction flow

1.1.1. Horse-shoe vortex

The most common flow feature of these junction flows is the formation of the HSVs (Figure 1.1). This vortical flow structure is obtained due to the combined effects of :

- Rolling up of the incoming fluid due to the adverse pressure gradient caused by the wing [18]
- Skewing and stretching of spanwise vorticity prevalent in the incoming turbulent boundary layer when passing the wing [18]

This HSV is an example of the first kind of Prandtl's secondary flow structure, where the streamwise vorticity is generated by the skewing of an existing mean vorticity in the flow [8].

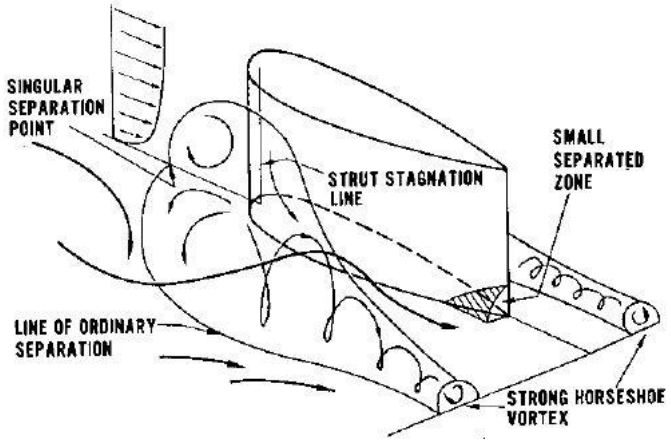

Figure 1.1: Example of HSV [5]

As can be observed from the above figure, each leg of the HSV has its vorticity in opposite directions. This vortex is not steady in terms of position, size or circulation [53]. These entrain high energy fluid along the wing and also increase the drag and heat transfer in the junction area by promoting higher turbulence in the region [14]. Moreover, the turbulent HSV shows coherent, low frequency unsteadiness. It is characterized by a bimodal nature of the velocity probability density functions taken very close to the leading edge of the wing [14]. This unsteadiness of the HSV leads to surface pressure fluctuations which are highly undesirable, as they might compromise the structural integrity of the wing/fuselage junction [53]. It also increases the turbulent stresses in the HSV region by an order of magnitude more than those produced by the classical shear mechanism inside the approaching turbulent boundary layer [14].

Fleming *et al* [18] extensively studied various parameters affecting the strength of the HSV. They concluded that the shape of the wing's leading edge and the approach boundary layer thickness are the two most important parameters governing the strength.

1.1.1.1. Effect of the wing's leading edge

They used a parameter called the Bluntness Factor (BF) to gauge the effect of various geometrical factors of the wing. It is defined as,

$$BF = \frac{1}{2}\frac{R_0}{X_T}\left(\frac{T}{S_T}+\frac{S_T}{X_T}\right), \tag{1.1}$$

where T is the maximum thickness of the wing, X_T is the chordwise position of T, S_T is the distance from the leading edge along the airfoil surface to T and R_0 is the leading edge radius. All these parameters are shown below. It can be seen that a blunt shape with T closer to the wing leading edge has a high BF and a sharp wing with T away from the leading edge has a low BF.

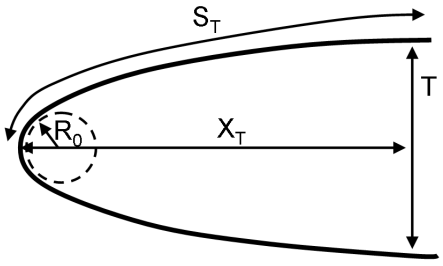

Figure 1.2: Geometric parameters in the BF calculation [20]

According to the experimental results, it was concluded by Fleming *et al* that higher BF caused the primary HSV to be larger and stronger, which consequently leads to higher interference drag, as explained by various authors [15, 29, 53]. They also observed that a sharper wing caused a weaker vortex. Their hypothesis

was that in the case of sharper wing, the HSV was concentrated closer to the surface and so the vorticity was rapidly diffused due to viscous and Reynolds stresses.

1.1.1.2. Effect of the approach boundary layer thickness

Fleming *et al* again introduced a new parameter called the Momentum Deficit Factor (MDF), which is the product of Reynolds numbers based on the momentum thickness of the approach boundary layer (Re_θ) and based on the maximum thickness of the wing (Re_T).

$$MDF = Re_\theta \cdot Re_T, \tag{1.2}$$

It was observed that as MDF increases, the mean vortex core moves closer to the wall and is more concentrated in the near wall region. The vertical distance of the vortex core from the wall is reduced, whereas the spanwise separation is increased. A similar result was obtained by Roach *et al* [46] from their investigations of short cylindrical struts attached to walls. They observed that the incremental drag (ΔD) due to the junction flow is a function of the approach boundary layer displacement thickness, δ^*, freestream dynamic pressure q and the strut thickness, T, *i.e.*

$$\Delta D = 1.9 q \delta^* T, \tag{1.3}$$

They also observed that neither the aspect ratio nor the cross-sectional shape of the strut has much influence on the incremental drag increase.

1.1.2. Lines of separation and low shear

Other common features associated with wing body junction flows are the presence of lines of low shear and separation around the wing. Devenport *et al* [14] performed oil flow visualization around the wing leading edge on a flat plate/Rood wing setup (Figure 1.3a).

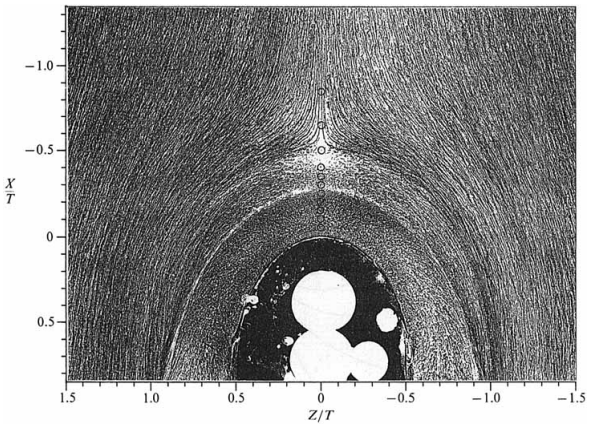

(a) Devenport [14]

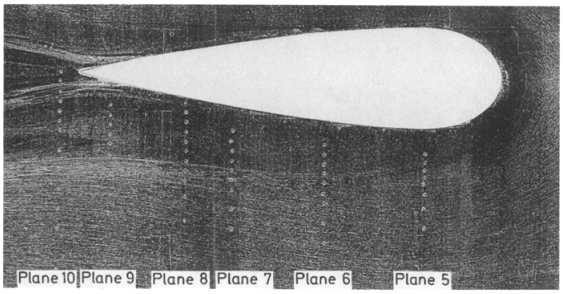

(b) Fleming [18]

Figure 1.3: Oil flow visualizations

Clearly, two separate lines can be observed around the wing. The one which originates at a saddle point ($X/T = -0.47, Z/T = 0$) is the line of separation. This line depicts the path of the fluid as it separates from the plate and travels around the wing. The other line, closer to the wing, is called the line of low shear. It is named as such because this line divides the separated flow into two distinct regions :

- The region closer to the wing of high surface shear stress
- An upstream region of low surface shear stress

The high surface shear is a result of the bimodal nature of the HSV, which will be discussed subsequently. This high stress region is also a region of intense backflow [14, 18]. The presence of these two separate regions were also confirmed by Fleming [18], Barber [5] and Olcmen [41]. Fleming *et al* [18] also observed a "fish tail" wake structure (Figure 1.3b) at the wing trailing edge. This particular structure has been observed by almost

all the authors who studied wing/body junction flows [20, 41, 48, 53]. This is another attribute of the junction flows, specific to wing/body junctions. If there were no junction, the streamlines exiting the wing at zero angle of attack would just exit parallel to the wing chord. However, in the presence of a junction, the above discussed HSV also travels around the wing, which will not be present for the isolated wing case. This HSV induces additional spanwise velocities to the flow exiting the wing at the trailing edge. To this discharged near wall flow, which already has very less momentum streamwise momentum, the induced spanwise velocities are added resulting in a net deflection of the flow which causes the fish-tail structure.

1.1.3. Bimodal behaviour

This is a flow mechanism which explains the increased levels of turbulence in the region of the HSV core. The probability density function (pdf) of velocity fluctuations in a typical turbulent field is Gaussian, with the most probable value centred at zero [39]. However, in a small region within the HSV core, it has been reported by various authors [14, 41, 42, 48, 53] that the pdfs of both streamwise and vertical velocity fluctuations has a double peak, with one peak at a negative value and the other very close to zero. Devenport *et al* [14] called them zero flow mode (zero peak) and backflow mode (negative peak). Interestingly, this behaviour was not observed for spanwise fluctuations. The pdfs of streamwise velocity fluctuations obtained using LDV experiments by Devenport *et al*, at various vertical positions in the region of the HSV are shown in Figure 1.4a. One obvious observation is that the size and shape of each pdf is not the same. However, we clearly see the presence of a zero and a negative peak. It looks to be produced by an addition of two Gaussian distributions. This bimodal behaviour is observed only for $Y/T < 0.05$, corresponding to the mid height of the HSV. Above this, the distribution is approximately Gaussian.

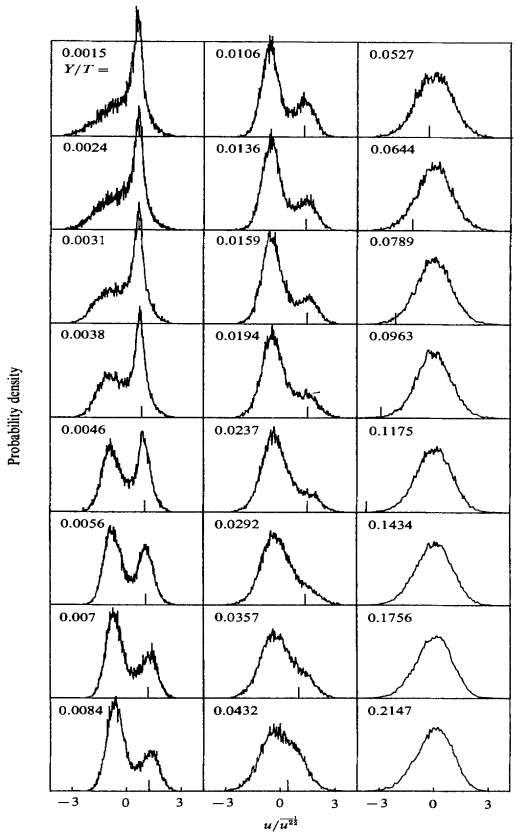

(a) Pdf of U velocity fluctuations. Measurements taken at $X/T = -0.2$ and $Z/T = 0$

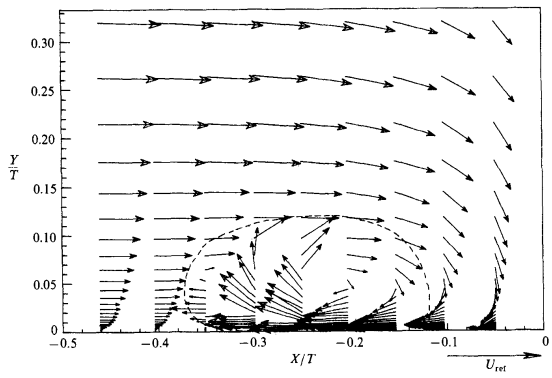

(b) Backflow mode

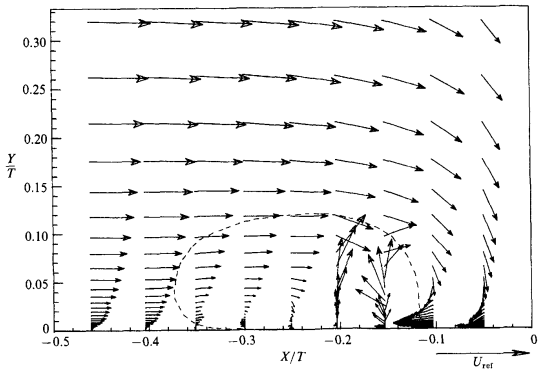

(c) Zeroflow mode

Figure 1.4: Bimodal behaviour [14]

The double peaked distribution of the fluctuations means that the flow has two preferred states: the zeroflow state (1.4c) and the backflow state (1.4b). The chaotic switching between these preferential states of the fluctuations has been characterized as a low frequency phenomenon and has been reported to have a

mean frequency of 38 Hz [14]. The presence of these two preferred states mean that the most probable value of the fluctuations is a non-zero value, which can be positive or negative. This consequently leads to the presence of abnormally high time averaged turbulent stresses in the junction area as reported by various authors [14, 41, 53], since the stresses are direct artifacts of these fluctuations. These increased stresses cause increase in drag and other undesirable effects such as increased surface pressure fluctuations and heat transfer rates.

1.1.4. Corner separation

This is one of the lesser investigated flow phenomena in wing/body junction flows. According to Gand *et al* [20], corner separation is an example of Prandtl's second kind of secondary motion, as opposed to the HSV, which is the first kind. This is because the corner separation is believed to be triggered by the gradients in Reynolds stresses. An example of corner separation is shown in Figure 1.5.

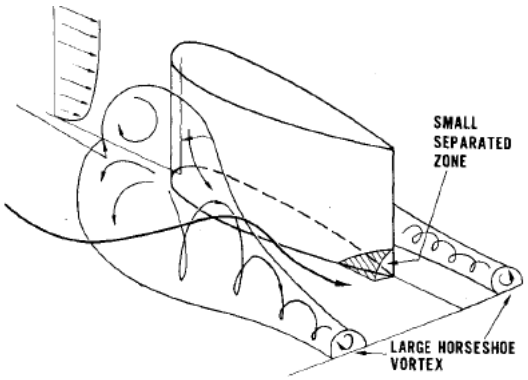

Figure 1.5: Geometric parameters in the BF calculation [20]

Barber *et al* [5] report that just like the HSV, Momentum Deficit Factor and Bluntness Factor govern the formation of this corner separation. They report that a stronger horseshoe vortex which originates from a thick boundary layer prevents the flow from separating in the corner, whereas for a smaller boundary layer and weaker horseshoe vortex, there is a significant corner separation. However, from their experimental studies of Gand *et al*, [20], they conclude that apart from MDF and BF, there are unknown factor which govern the onset of corner separation.

1.2. Drag in junction flows

This chapter discusses the available literature on already existing methods of drag reduction for a wing/plate junction. Generally, total aerodynamic drag is composed of various components of drag. In almost all the practical cases, only certain components play a major role in total drag contribution. These types are shown in Figure 1.6.

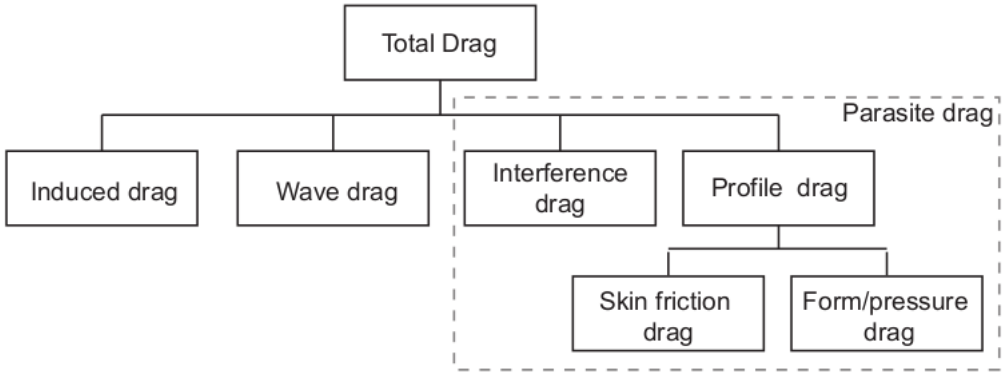

Figure 1.6: Types of aerodynamic drag [34]

Induced drag is caused by the effective change in the angle of attack of the wing, induced by the wing tip vortices, arising due to the pressure difference between the upper and lower surfaces of the wing at the wing tip. Wave drag is only applicable in the supersonic flow regime. It is a consequence of the loss in total pressure over the wing due to the presence of a shock wave. Skin friction occurs due to the slowing down of the fluid by the wall surfaces resulting in viscous shear stresses acting on the wetted area. Form/pressure drag is the resultant of the integration of static pressure forces that act normal to a surface. This drag is a consequence of the static pressure differences caused due to the shape of the object, resulting in a net force in the direction of the drag. Interference drag arises because of the interaction of two boundary layers developing in two different directions. For example, in the case of wing/fuselage junction, interference drag is the result of the interaction between the boundary layers developing on the wing and the fuselage, which are almost perpendicular to each other. Typically, the drag of a wing/fuselage system will be higher than the sum of isolated wing and fuselage. This difference can be attributed to the interference drag. Kubendran *et al* [30] reports that the interference drag in the wing/fuselage junction is made up of three parts:

- Change in the surface shear stress caused by the merging of the two boundary layers and by the distortion of the velocity profiles in the juncture due to the secondary flow
- Induced drag attributable to a loss of energy to the secondary flow in the junction
- Change in pressure drag brought about by the modified growth of the viscous layer in the junction

From the above three points, it is clear that the interference drag is caused due to the presence of this secondary flow structure, which is the HSV. This motivated various researchers to manipulate the junction area to curb and impede the formation of this vortex, and consequently, reduce the interference drag. An overview of the most important works related to such drag reduction mechanisms are discussed below.

1.2.1. Leading edge and upstream devices

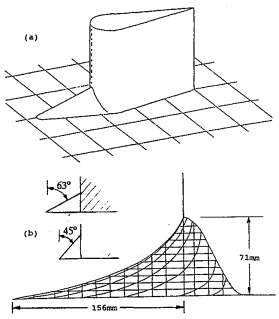

(a) Leading edge fillet [15]

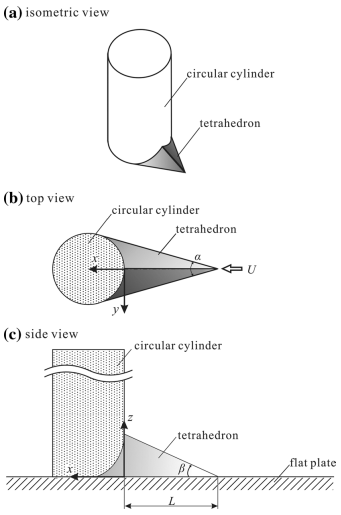

(b) Leading edge tetrahedron [24]

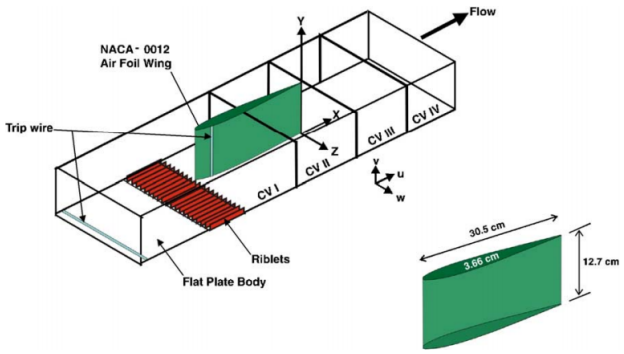

(c) Upstream riblets [26]

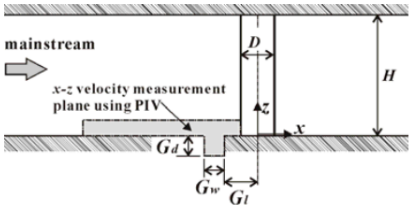

(d) Upstream cavity [27]

Figure 1.7: Examples of leading edge and upstream devices

Leading edge fillets/fairings are passive devices wrapped around the nose of the wing (Figure 1.7a). They are very effective in reducing the interference drag as observed by Devenport *et al* [15]. They studied the effect of having a leading edge fillet wrapped around the wing nose on various features of wing/body junction flows. They observed that the magnitude of the adverse pressure gradient in front of the nose was greatly reduced, thus eliminating the leading edge separation. The formation of HSV was completely curbed and consequently, no bimodal unsteadiness was observed. Cross stream pressure gradients were also reduced and therefore skewing of the incoming boundary layer was lessened. However, when they investigated the effect of these fillets at higher angles of attack, they found that the fillet was far less effective compared to its performance at zero angle of attack. Kubendran *et al* [29] also confirmed the reduction of the adverse pressure gradient due to the use of leading edge fillets for a laminar flow field. They however observed that the use of a small fillet (1 inch) resulted in a net increase in drag since the increase in the viscous drag due to larger wetted area is not compensated enough by the reduction in the interference drag. However, for a large fillet (2 inch) they report that net drag reduction is achieved.

Huang *et al* [24] experimentally investigated the effect of a tetrahedron attached to the upstream corner of a laminar cylinder/flat plate junction(Figure 1.7b). They observed that for the baseline case (without tetrahedron), a single-vortex, dual-vortex or triple-vortex system was formed based on the flow Reynolds number and boundary-layer thickness. They argue that the HSV system obtained with the baseline case will be altered to a characteristic mode of vortical flow, reverse flow, or forward flow due to the presence of the tetrahedron. The type of mode depends on the geometrical parameters of the tetrahedron such as normalized axial length, expansion angle, and tilt angle and also on the Reynolds number of the flow. They observed the presence of vortical flow mode for a small axial length, in which the number of horseshoe vortices reduced by one compared to the baseline case. The forward flow mode appears for a large axial length, in which the upstream boundary layer doesn't separate and thereby, the formation of HSV is eliminated.

Instead of attaching any device to the nose of the wing/cylinder, Kairouz *et al* [26] employed upstream riblets to study their effect on the turbulent HSV around a NACA 0012 wing (Figure 1.7c). They observed that the riblets displaced the HSV away from the corner and also reduced the strength. The turbulent Reynolds stresses near the corner were lessened in magnitude. They also observed that the riblets resulted in a reduced secondary flow, which was accompanied by reduced mean streamwise vorticity.

Kang *et al* [27] investigated the variation in the strength of HSV around a cylinder with an upstream slot on the plate (Figure 1.7d). No mass addition or reduction was employed through the cavity. They observed that the two vortex system they observed for the baseline case was changed to a single vortex system because of the cavity. They concluded that the strength of the primary vortex weakened due to the recirculation zone in the cavity, which also resulted in the diffusion of the mainstream flow.

1.2.2. Boundary layer suction and blowing

Other common methods of reducing the interference drag are active flow control techniques such as boundary layer suction/blowing to manipulate the flow in the junction area. Philips *et al* [44] experimentally investigated the effect of applying boundary layer suction to the upstream boundary layer on the strength and

size of the HSV. Their idea was to eliminate the spanwise vorticity in the boundary layer, thereby mitigating the formation of HSV. They observed that the technique was successful in reducing the strength of the HSV, although not completely eliminating it. However, they also observed the addition of streamwise vortices arising due to the cut on the tunnel wall through which suction was applied.

Seal *et al* [51] studied the effect of suction on a cylinder junction flow using PIV. They also confirmed the effectiveness of the suction in reducing the strength of the HSV. They observed that the spatially limited suction weakens both the instantaneous and time averaged vortex-surface interactions. They also report that the time averaged Reynolds stress levels were reduced in both the symmetry and the downstream planes.

Johnson *et al* [25] studied the effect of both the suction and blowing of the upstream boundary layer on the wing/fuselage junction vortex. They observed that vortex attenuation was achieved due to the removal of the boundary layer by suction, but there was a very weak vortex formed even at the highest suction rate due to the no slip boundary condition. As the angle of incidence was increased, they observed that the vortex moved to the pressure side of the airfoil and thus the suction was less effective. Also, surface normal blowing was found to attenuate the vortex formation by energizing the boundary layer and preventing the separation. However, it was reported that too high a blowing rate could cause flow structures that are much larger than the junction vortex, thereby causing higher drag.

Barberis *et al* [6] compared the effectiveness of a fillet shaped addon device attached at the junction and boundary layer suction. They concluded that for the case with suction, the size of the vortex was much smaller and the separation point was much closer to the wing compared to the case with fillet. The presence of the fillet did decrease the strength of the vortex, but did not significantly change the magnitude. However, they observed a greater decrease of turbulent kinetic energy near the wall in the vicinity of the junction for the case with fillet compared to the suction case. The increase in suction rate brought the junction vortex more closer to the leading edge of the wing and there was also a gradual decrease in the size of the vortex. It was inferred that suction results in absorption of the boundary layer and consequently reducing the near wall vorticity. This behaviour resulted in greater reduction in the size of the vortices.

The above reviewed literature shows that the use of leading edge devices and active flow control could indeed be an efficient tool to reduce or eliminate the secondary flow structure, reduce the turbulent stresses associated with it and consequently reduce the interference drag. As for the active flow control techniques, although they show greater promise, practically, it is not always easy to integrate them into a wing/fuselage system. Also, careful consideration should be given to the placement of the leading edge devices as well as the position and the rate of active flow control application in order to obtain a net drag reduction. In the case of add-on devices, there is always a possibility of increased skin friction overpowering the decreased interference drag, resulting in a net drag increase, as observed by Kubendran *et al.* It is also not clear how these leading edge devices would perform in different flow situations such as different angles of attack and higher Mach numbers. As reported by Devenport *et al*, the performance of these devices might deteriorate at greater angles of attack. Most of these problems stem from the fact that the size, shape and location of these devices were arrived upon by means of a trial and error approach, because of which there is always a chance of a better design of the same device. This drawback can be overcome using aerodynamic shape optimization.

1.2.3. Aerodynamic optimization

One of the main objectives of the current thesis is the investigation of the performance of a new, unconventional type of drag reduction methodology. The main idea is based on redesigning the shape of the flat plate/fuselage in the region around the wing's point of contact through aerodynamic optimization. With the advent of adjoint methods, the computational costs of gradient-based optimization have come down drastically [7]. Various authors have used this technique to arrive at an optimized design of the junction.

Brezillion *et al* [9] used an adjoint-based gradient optimization approach to efficiently reduce the flow separation onset at wing–fuselage intersection. The optimization was carried out on a DLR-F6 wing/body configuration. They could successfully reduce the region of separation within a limited number of flow computations The optimized fairing, which had a double-dented shape on the fuselage, resulted in a drag reduction of 7.1% for the complete configuration.

For the same configuration of DLR-F6 wing/fuselage intersection, Xu *et al* [62], performed a CAD-based shape parameterization using a RANS based adjoint solver. They too obtained substantial suppression of junction flow separation for the redesigned fuselage, which interestingly had two distinct bumps, as opposed to the dents obtained by Brezillon *et al.* They could effectively get a drag reduction of 4.4%.

Peigin *et al* [43] used aerodynamic optimization on a wing–body fairing for a generic business jet configuration at realistic transonic cruise flight conditions. The method they used was driven by accurate, complete Navier–Stokes evaluations of the objective function, with the optimization engine based on genetic algorithms. From their redesign of the fairing, they could achieve significant drag reduction over a range of Mach numbers.

Song *et al* [55] used a novel two level optimization applied to a wing-body-fairing geometry. They defined B-spline curves which represent the fairing geometry and used surrogate models to optimize its shape for minimum drag at a particular lift coefficient. They could obtain a total drag reduction of about 6.3 drag counts for the wing-fuselage system.

A similar technique was applied by Sasaki *et al* [50] for a Supersonic Transport (SST) wing-body configuration. Their objectives were to reduce the aerodynamic drag and also the sonic boom intensity by optimizing the wing/fuselage junction. They used structured multiblock grids to represent the wing-body configuration and defined 131 design variables for optimization. They had used a solver which solved the Navier-Stokes equations in the Euler form [3] to obtain the solutions for the compressible flow parameters. A thicker fuselage was obtained to lower the sonic boom but it had poor aerodynamic performance. They concluded that to reduce both the boom intensity and the drag, the lifting surface should be distributed in an innovative manner, resulting in an unconventional wing-fuselage configuration.

Lyu *et al* [33] used RANS based aerodynamic optimization to redesign a blended wing-body aircraft. They employed a gradient-based optimization algorithm along with a discrete adjoint method to calculate the derivatives of the aerodynamic forces. A total of 273 design variables were considered with the objective of minimizing the drag coefficient in cruise condition and subjected to lift, static margin, trim and bending moment constraints. By enforcing a small static margin of 1% and including the centre of gravity position as a design variable, they could obtain the best compromise between stability and performance of the aircraft. The optimized configuration had a trimmed configuration which exhibited a nearly elliptical lift distribution. Also, a combination of washout and reflex airfoils which were determined as the best by the optimizer were employed in the design.

1.2.3.1. The Anti-fairing

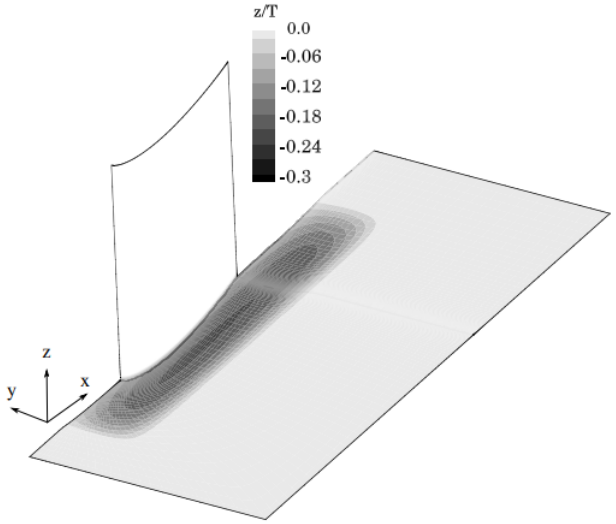

Figure 1.8: The anti-fairing [7]

Belligoli *et al* [7] used a similar optimization algorithm to redesign a wing/flat plate configuration with one main difference compared to the above discussed literature. Unlike other studies, the optimization was performed only on the flat plate region around the wing, with the wing excluded from the redesigning. This made it possible in the current thesis to test different wing types for the same redesigned flat plate region. The initial configuration used by them consisted of a NACA0015 wing at zero angle of attack, mounted on a flat plate perpendicularly. A RANS gradient based optimization was performed on this with the objective being the minimization of the drag force at the junction. The CFD solver SU2 was used, which had the capability to solve both RANS and the corresponding adjoint equations. The obtained optimized shape had the form of a shallow, concave dent in the flat plate (Figure 1.8). Since the shape is a complete opposite of a conventional fairing, it was named as the anti-fairing.

To gauge its effectiveness on the drag reduction, the anti-fairing was investigated both experimentally and numerically. Experimental investigation was done using PIV and the numerical investigation employed a more refined RANS analysis (11.5 million cells) than the one used in the optimization (1.6 million cells). The results of the anti-fairing were also compared to more conventional designs such as the 'short' and 'long' fairings from Oudheusden *et al* [59]. Figure 1.9 shows the normalized streamwise velocity plots in the wake of the wing for all the cases.

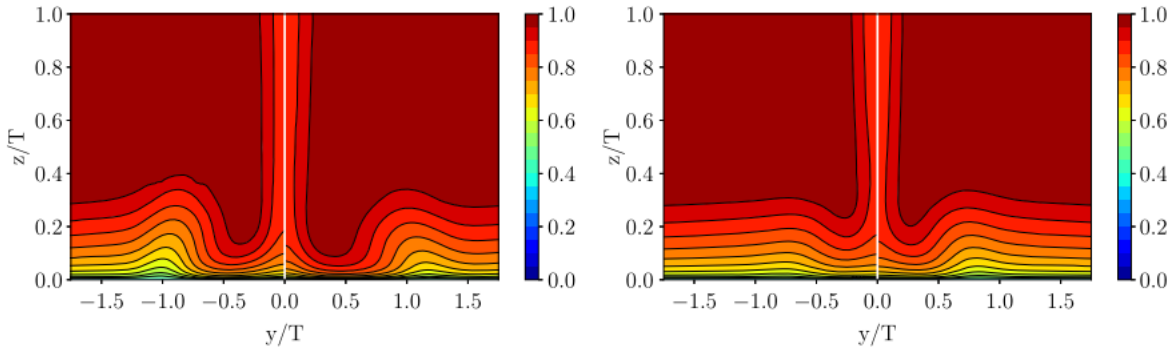

a) Streamwise velocity fields from the BS (left) and AF (right) configurations

b) Streamwise velocity fields from the LF (left) and SF (right) configurations

Figure 1.9: Mean normalized streamwise velocity contours in the wake of BS (baseline), AF (anti-fairing), SF (short fairing) and LF (long fairing) cases. [7]

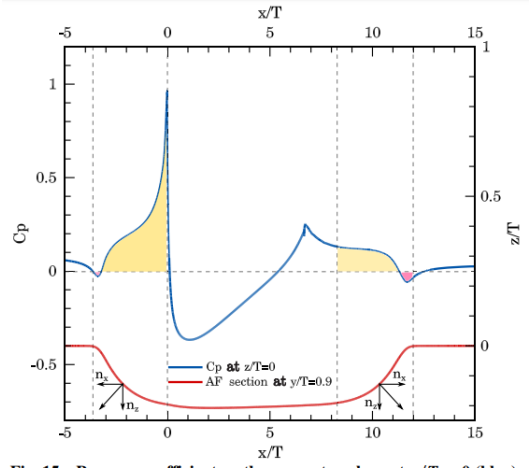

(a) Cp on the symmetry plane at $z/T = 0$ (blue), Anti-fairing cross-section (red). [7]

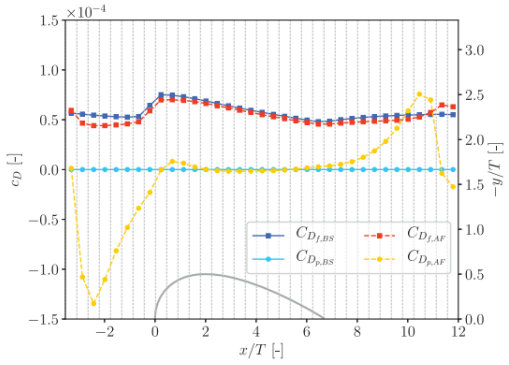

(b) Near field drag breakdown of the baseline and anti-fairing cases [7]

Figure 1.10: Drag reduction mechanism of the anti-fairing

The footprint of the HSV is marked by the lump in the velocity contour. It can be observed that both

the baseline and the anti-fairing case has significant warping of the contour, with the HSV size being slightly smaller for the AF case. In the case of conventional fairings, the short fairing has a weak HSV footprint, whereas it is virtually non-existent in the LF case. It was concluded that unlike the conventional fairings, the drag reduction mechanism of the anti-fairing did not involve curbing the formation of HSV.

To understand the exact mechanism, near wall pressure coefficient in the symmetry plane and the near field drag breakdown for the anti-fairing was investigated (Figure 1.10). It can be seen from Figure 1.10a that the pressure in front of the wing is much higher. But this actually happens even for the baseline case. The difference here is that due to the concave shape of the anti-fairing, the normal to the surface is inclined at an angle as shown. This means that the pressure force acting on the surface has a component in the direction opposite to that of the drag. This can be observed from Figure 1.10b, where a negative pressure drag is observed for the anti-fairing case. In the wake of the wing, the anti-fairing shape is such that the pressure force acts in the direction of the drag. Thus there is an increase in the pressure drag in the wake. However, the pressure in front of the wing will always be much higher than the pressure in the wake because of the incomplete pressure recovery over the wing. Also, there's negligible difference in the viscous drag between the baseline and the anti-fairing case. This means that the net effect of the anti-fairing is a positive propulsion force or a negative pressure drag force on the wing. Belligoli reported a drag reduction of approximately 6 drag counts for the anti-fairing, compared to 0.2 and 0.1 drag counts for the long and short fairings respectively. However, PIV results showed a drag reduction of 7.8 drag counts for the anti-fairing.

Thus, from the reviewed literature, it can be seen from the preliminary analysis that anti-fairing has much better drag reduction capability compared to the conventional methods. Also, using anti-fairing as a means of drag reduction is advantageous due to the fact that it doesn't involve any extra addon device or an active flow control mechanism integrated with the wing. However, although the results reported by Belligoli [7] and Koers [28] look promising, they report varying drag reduction capacities from the experiments and CFD. This might be due to the fact that the CFD analysis was conducted using a steady RANS solver, which is not a good choice to capture such highly unsteady flow physics in the junction. Moreover, since they used the Spalart-Allmaras RANS model, which is a one equation eddy viscosity model, none of the turbulent stresses were captured by them. Therefore, it is still not clear how these turbulent quantities are affected because of the use of anti-fairing. This forms the motivation to conduct a further, elaborate study of the anti-fairing using more accurate CFD methods.

1.3. Numerical studies on wing/body junction

Apsley *et al* [4] conducted an extensive wall-resolved study of different RANS models for a generic wing/plate junction case. The study included 5 linear Eddy Viscosity Models (EVM), 3 Non-Linear Eddy Viscosity Models (NLEVM) and 4 Differential Stress Models (DSM). The simulations were run for the same case used in the experimental study of Devenport [14] and all the results were compared to their experimental data. Their final conclusions were that none of the RANS models are sufficient to accurately capture the near wall turbulence of the junction or the shape and location of the HSV. Nevertheless, they observed that the DSMs performed the best overall, with $k-\omega$ SST model giving the best prediction of the mean flow quantities among all the EVM variants. However, they also observed that the SST model predicted a further upstream location of separation compared to the experimental results, which was attributed to the high sensitivity of the ω equation to adverse pressure gradients.

Paik *et al* [42] tried to simulate the wing/flat plate junction flow using a variant of LES called the Detached Eddy Simulation (DES), also called hybrid RANS/LES methods. They used Spalart Allmaras based DES model, where the SGS model used was an one-equation model, that solves a transport equation for subgrid scale viscosity. They had tried two variants of the DES model; a standard DES model and an adjusted DES model. When standard DES model was used they observed premature laminar like flow separation upstream of the wing. They attributed this to the fact that the LES mode of the solver was prematurely activated in the attached region, instead of solving the URANS equations. To overcome this, an adjusted DES length scale was used which enforced solving URANS equations regardless of local grid refinement near the wall. This adjusted model seemed to capture the bimodal dynamics better and also eliminated the laminar like separation. However, the adjusted model predicted the location of the HSV core to be far more upstream than the one in experimental. They postulate that it could be solved by using a different RANS model or by using a

time-varying inflow boundary condition.

The inaccuracy in the prediction of the HSV core location when using DES was also reported by Fu *et al* [19] in their investigation of the Rood wing/flat plate junction flow. Unlike Paik *et al*, they had used two equation $k-\omega$ SST variant in their hybrid RANS/LES model. They too had observed earlier flow separation and vortex breakdown. However, they had observed that using Delayed Detatched Eddy Simulation (DDES) greatly improved the prediction of the HSV location and strength. According to Spalart [57] DDES detects the boundary layers and prolongs the RANS mode, despite having a smaller wall parallel grid spacing. In other words, it delays switching on the LES mode of the solver. Spalart also reports that DDES solves the issue of grid induced separation and modeled stress depletion. These two were the primary problems of the standard DES model of Paik *et al*.

Ryu *et al* [48] performed LES of a Rood wing/Flat plate junction flow. They had performed a coarse grid (5 million) and a fine grid (47 million) wall-resolved LES and studied the effect of the grid refinement. Also, a precursor RANS ($k-\omega$ SST) simulation was performed on the coarse grid to use the results as the initial flow field for the LES simulation. Vreman model was used to compute the subgrid scale stress tensors. Their results were compared to the results from the experimental results of Devenport [14]. They observed that both the coarse and fine grid LES captured the presence of secondary structures quite accurately, with the coarser grid simulation predicting them weaker in comparison to the experimental results. The RANS did not show any presence of these. They attribute this to the fact that the linear eddy-viscosity RANS models do not resolve the anisotropy in the normal Reynolds stresses and hence fail to predict these structures. They conclude that the rich, highly unsteady bimodal flow dynamics of the junction flow are satisfactorily captures by the refined LES. They also report that though RANS poorly predicts the second order moments and vorticity components, mean flow quantities such as pressure and velocity are captured quite accurately.

Another extensive study was conducted by Gand *et al* [20] which involved an experimental investigation of a NACA0012 wing/plate junction, RANS simulations and LES of the same case. The main aim was to test the effectiveness of the numerical simulations compared to the experimental results. Various types of RANS models were considered: Spalart Allmaras (SA), the $k-\omega$ Wilcox model, Menter SST $k-\omega$ model and the SSG Reynolds Stress Model (RSM). For LES, the selective mixed scales subgrid scale model of Lenormand *et al* [31], a type of SGS model for compressible wall-bounded flow was used. They too reported a superior prediction of the flow features when LES was used. They observed that RANS models erroneously predict a corner separation in the aft part of the wing, which is not seen in the experiment. LES, however gave a better picture, with the skin friction lines and the total pressure contours in the wake accurately matching the experimental results. They also arrive at a similar conclusion as Ryu *et al* : though RANS models give a bird's eye view of the flow physics of the junction flow, its complex three dimensional nature can be better resolved using LES.

From all the reviewed literature, it is clear that RANS simulations are not sufficient to capture the flow physics of wing/body junction. Important flow parameters such as separation location, location of the HSV core, upstream and wake turbulent quantities are not satisfactorily resolved by RANS. However, given its comparatively low computational resource requirements, it may be a good choice to opt for, provided one is just interested in resolving the mean velocity and pressure quantities or integrated loads, since they give fairly good prediction of these, as observed by Apsley. DES seems to be a better alternative compared to RANS, but that too has its fair share of problems with predicting the vortex locations, as observed by Paik, Fu, Spalart. Therefore, if one has to completely capture the unsteady dynamics of the junction flow along with accurate description of quantities in the junction, LES seems to be the best available option. The only foreseeable drawback of LES compared to RANS or DES is the higher computational resource requirements, which is inevitable if accurate description of flow features is needed.

1.4. Research objective:

The anti-fairing design discussed in the previous sections shows great potential for drag reduction. But all the numerical analysis done till now [7, 28] have been using RANS. As has already been established a lot of times, the flow physics in the vicinity of the wing/body junction is quite complicated and using RANS to capture the flow physics is not a good option as it doesn't resolve the highly turbulent and unsteady nature of the flow. Therefore, the research objective and sub-objectives can defined as follows:

Perform a numerical study of a novel design of wing/body junction, the Anti-Fairing, using Large Eddy Simulations and elucidate the complex turbulent phenomenon involved.

- Validation of the order of magnitude of drag reduction of the anti-fairing reported by Belligoli [7]
- Validation of the drag reduction mechanism postulated by Belligoli
- Investigate the effect of anti-fairing on the unsteady and turbulent nature of the flow in the junction
- Analysis of the effect of different approach boundary layer thicknesses and different anti-fairing thicknesses on the drag reduction capability of anti-fairing

1.4.1. Research questions:

Based on the discussed literature study, the following research questions are formulated to aid in achieving the above mentioned research objective:

- How does capturing the unsteady dynamics change the reported drag reduction magnitude of anti-fairing ?
- How are the turbulent Reynolds stresses in the junction area and in the wake affected by the presence of anti-fairing?
- How are the location, size and the bimodal nature of the HSV affected by the anti-fairing ?
  - How do they affect the interference drag of the system ?
- What are the main characteristics of the flow in the anti-fairing region?
  - How different are the flow characteristics compared to a normal junction flow?
  - How much is the drag reduced and how does it compare to the existing mechanisms ?
- What are all the flow parameters that define the drag reduction capability of anti-fairing ?
  - How does varying the anti-fairing thickness affect the drag reduction ?
  - How does varying the inlet boundary layer thickness affect the drag reduction ?

2

Numerical methodology

This chapter gives a brief description of the methodology involved in setting up and successful running of the CFD simulations. The CFD analysis performed in the current study consists of two stages: the first stage is performing Large Eddy Simulation (LES) for the wing/flat plate junction (baseline) and the wing/anti-fairing junction. As mentioned in the research objectives section, the motivaion to perform LES was to investigate the effect of anti-fairing on the unsteady and turbulent nature of the flow in the junction. The flow parameters were taken from the experimental study of wing/plate junction by Devenport *et al* [14] so that their results would serve as validation for the baseline case. The performance of the anti-fairing is then gauged by comparing the LES results of the baseline and the anti-fairing cases. The second stage of the analysis involves performing RANS simulations for various anti-fairing depths and approach boundary layer thicknesses to observe their effect on the performance of the anti-fairing. The simulation setups employed for both these stages of CFD analysis are explained further in detail in the subsequent pages.

2.1. Large Eddy Simulation

2.1.1. Governing equations

For an incompressible, Newtonian fluid, the equations which describe the fluid flow are the Navier-Stokes (NS) equations. These are given as:

$$\frac{\partial U_i}{\partial x_i} = 0, \tag{2.1}$$

$$\frac{\partial U_i}{\partial t} + \frac{\partial U_i U_j}{\partial x_j} = -\frac{1}{\rho}\frac{\partial P}{\partial x_i} + \frac{\partial}{\partial x_j}\left[\nu\left(\frac{\partial U_i}{\partial x_j} + \frac{\partial U_j}{\partial x_i}\right)\right], \tag{2.2}$$

where U_i denote the velocities along the three Cartesian axes, P denote the pressure, ρ denote the density and ν denote the kinematic viscosity. The first equation is the continuity equation denoting the mass conservation. The second equation represents the momentum conservation in the three coordinate directions. Turbulent flows are characterized by the presence of different scales of turbulent motion. These range from the a size comparable to the geometrical length scale of the flow to much smaller scales. According to Richardson's hypothesis [45], kinetic energy enters the turbulence through the production mechanism at the largest scales of motion, which are then transferred to smaller and smaller scales through the energy cascade process until, at the smallest scales, this energy is dissipated by viscous action. Therefore, to obtain the LES equations, the flow quantities are first separated into scales which contain most of the turbulent energy, called the resolved scales and scales which contain the remaining lesser energy called the unresolved scales. This separation is obtained by employing a filter, whose width is typically a function of the cell size of the computational mesh used [45, 49]. Thus the total flow quantities (U_i, P) are given as the sum of resolved scales $(\overline{U}_i, \overline{P})$ and the unresolved scales (u_i'', p'').

$$U_i = \overline{U}_i + u_i'', \tag{2.3}$$

$$P = \overline{P} + p'', \tag{2.4}$$

The resolved scales are computed directly and represent the solution of an LES, whereas the unresolved scales and their effects need to be modelled. Substituting this decomposition and applying the filtering operation to all the above equations yield the filtered LES equations.

$$\frac{\partial \overline{U}_i}{\partial x_i} = 0, \tag{2.5}$$

$$\frac{\partial \overline{U}_i}{\partial t} + \frac{\partial \overline{U}_i \overline{U}_j}{\partial x_j} = -\frac{1}{\rho}\frac{\partial \overline{P}}{\partial x_i} + \frac{\partial}{\partial x_j}\left[\nu\left(\frac{\partial \overline{U}_i}{\partial x_j} + \frac{\partial \overline{U}_j}{\partial x_i}\right)\right] - \frac{\partial \tau_{ij}}{\partial x_j}, \tag{2.6}$$

All the terms except the last term on the right can be computed directly from the resolved flow quantities obtained directly from the LES solution. To close this set of equations, τ_{ij} needs to be modelled. This is called the subgrid scale stress (SGS) tensor and various types of LES models differ based on the formulation of this SGS tensor. This is given as [49]:

$$\tau_{ij} = \overline{U_i U_j} - \overline{U}_i \overline{U}_j, \tag{2.7}$$

Two major classifications of the modelling of SGS tensor are the explicit method and the implicit method. Explicit SGS models provide explicit approximations or estimations of the unclosed SGS terms obtained after filtering [2]. These require the explicit computation of SGS-stress approximations during time advancement. Examples of such models include the famous dynamic Smagorinsky model [21], WALE model [17], Vreman model [61]. The current LES study however was performed using an in-house LES solver called INCA which employs an implicit method of modelling the SGS tensor. Implicit LES (ILES) works based on the assumption that "the action of subgrid scales on the resolved scales is equivalent to a strictly dissipative action" [49]. This is a valid assumption since the smaller unresolved scales get their turbulent kinetic energy from the higher energy carrying resolved scales (energy cascade) and the effect of the SGS tensor is to model the amount of energy lost to these smaller scales. ILES uses dissipation terms which are generally introduced in the framework of the upwind schemes used for the convective terms. The truncation error that arise due to the discretization of the convective terms is directly used to model the SGS tensor. The LES solver used in the current study involves using a specific type of discretization scheme called Adaptive Local Deconvolution Method (ALDM) [2] which aids in implementing ILES.

2.1.2. Wing junction geometry

The wing used in the current LES study is a Rood wing, which has a 3:2 elliptical nose and a NACA 0020 tail. This wing type was chosen to mimic the wing used by Devenport *et al* [14] in their experiments of wing/plate junction. The wing has a chord length of $c = 0.305m$ and a maximum thickness of $T = 0.0717m$. The baseline case has the wing protruding from a flat plate, whereas in the anti-fairing case, the wing is mounted onto the anti-fairing geometry. These wing and the surface geometries are shown in Figure 2.1. Also the front and side view of the anti-fairing are shown in Figure 2.2.

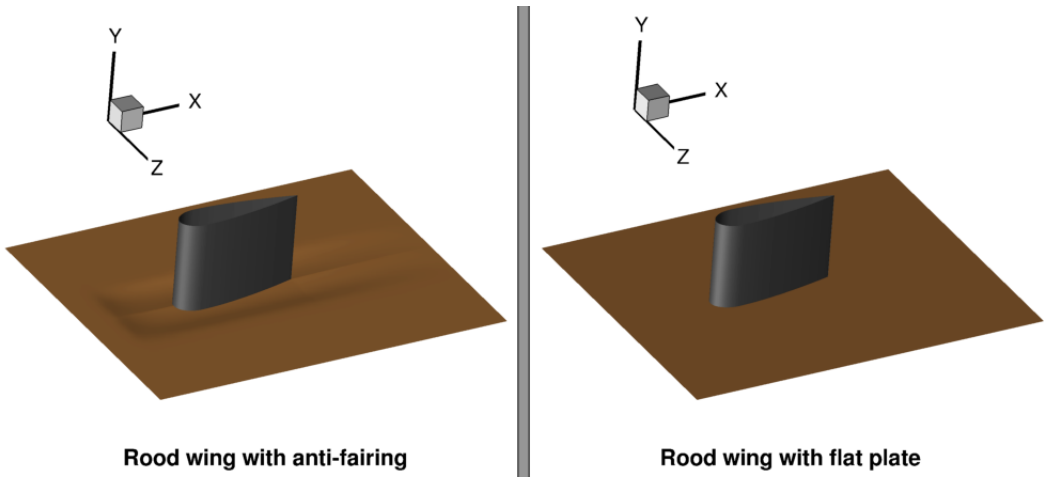

Figure 2.1: Comparison of wing/antifairing and wing/plate configuration

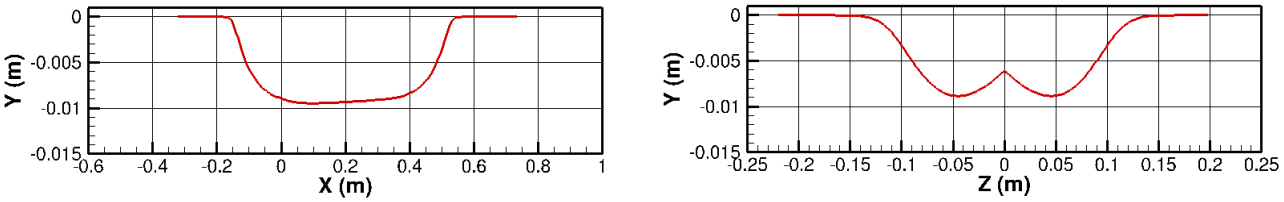

(a) Front view along a line drawn at $Z = 0.04m$

(b) Side view along a line drawn at $X = 0.365m$

Figure 2.2: Geometry of the anti-fairing

2.1.3. Computational domain

The domain under study consists of a rectangular bounding box within which the wing is immersed. The inlet plane is situated $2.3c$ upstream of the wing nose while, the outlet of the domain is located $3.3c$ downstream of it. The front and the back planes are both situated at $1.5c$ in front and back of the wing tip respectively. Finally the top plane of the domain is at $y = 0.2151m$. The domain used is identical for both the baseline and the anti-fairing cases with the only difference being the bottom surface geometry. The front, back and top plane positions are taken to mimic the domain used by Ryu *et al* [48] in their LES study of Rood wing/flat plate junction flow. The inlet and outlet plane positions are slightly extended compared to the domain used by Ryu *et al* to ensure these planes are far away from the anti-fairing. Also, the inlet boundary condition used in the present work necessitates the upstream position of the inlet plane used here. The details of this boundary condition are discussed below.

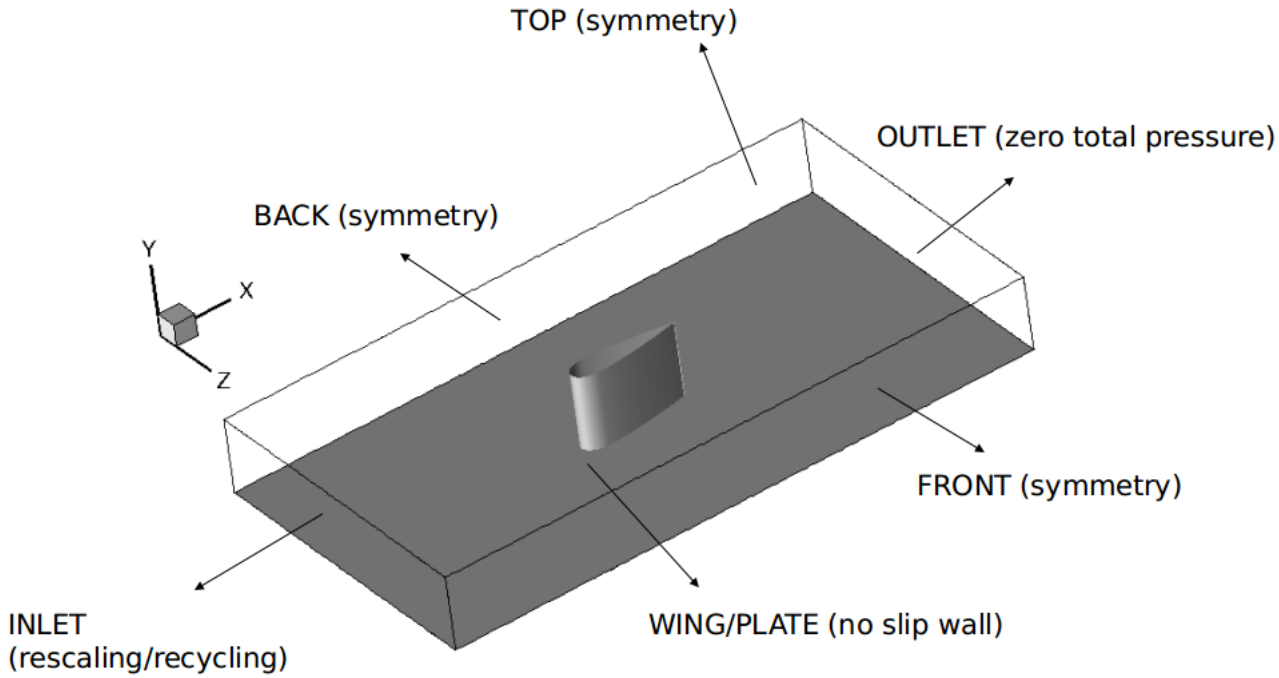

Figure 2.3: Computational domain used for LES

2.1.4. Boundary conditions

Choosing appropriate boundary conditions is indispensable in any CFD simulation. The choice of the turbulent inflow boundary condition for an LES simulation greatly affects the accuracy of the results, since the downstream flow dynamics greatly depend on the inflow fluctuations. Ideally, one would like to have a long domain length in which the flow starts developing from a laminar state and transitions to a fully turbulent state. But this would exponentially increase the computational costs, and is therefore rarely used. Dhamankar *et al* [16] discusses three methods of generating turbulent inflow boundary conditions :

- **Library based methods :**

This method relies on an external turbulence database which has the necessary instantaneous inflow plane data. This type of database can either be a preexisting library or it can be obtained precursor/concurrent simulation.

- **Synthetic inflow generators :**
  This method involves synthesizing a realistic turbulent inflow based on given data at the inlet, such as the mean flow, Reynolds stress.

- **Rescaling/recycling boundary condition :**
  The final method aims to generate an appropriate turbulent inflow boundary layer by recycling and rescaling the velocity data from a downstream plane based on similarity laws [32, 56].

The first method was rejected straightaway, since running a precursor simulation is very expensive. Also, a database of all required flow parameters could not be found. Even if found, it must be interpolated to the mesh that is used in the current study, which might lead to inaccuracies. The second method necessitates the presence of turbulence data such as Reynolds stresses and kinetic energy to build an accurate inflow generator. As with the first case, such data, even if found, would suffer from interpolation issues due to the use of different computational grid. Therefore, the best option available was the rescaling/recycling boundary condition. The necessary condition to be satisfied to use this type of boundary condition is to have the downstream recycle plane at least $7\delta_{in} - 10\delta_{in}$ away from the inlet plane [32]. As explained by various authors [16, 32, 56] having the recycle plane too close to the inlet results in spurious low frequency oscillations added to the mean flow field.

The inlet boundary layer thickness was defined to have $Re_\theta = 6700$ at $2.15T$ upstream of the wing for the baseline case, where Re_θ is the momentum thickness based Reynolds number. This is done to mimic the same flow conditions as the experimental study of Devenport [14]. The boundary layer thickness at the inlet was obtained using the relations from Choi *et al* [12] for flat plate boundary layer growth:

$$\frac{\delta}{x} = 0.16 Re_x^{-1/7}, \tag{2.8}$$

$$\theta = \frac{7}{72}\delta, \tag{2.9}$$

where Re_x is the Reynolds number based on an equivalent length of the flat plate if the boundary layer starts growing from $x = 0$. Based on the above relations the inlet boundary layer thickness necessary was obtained to be $\delta_{in} = 0.02819m$. Thus the location of the recycle plane was fixed $10\delta_{in}$ away from the inlet plane, which satisfies the condition necessary for the rescaling/recycling boundary condition. Also, the recycle plane is well away from the start of the anti-fairing dent and so the boundary layer won't experience any influence from the geometry.

The other boundary conditions are more straightforward. The outlet plane is given a boundary condition which fixes the total pressure in the entire plane to zero, *i.e.* $P^{out}_{total} = 0$. The front, back and the top planes are taken as symmetry planes as taken by Ryu *et al* [48]. Finally, the wing and the bottom plane are given no slip, no penetration boundary condition. A summary of the boundary conditions is shown below:

Table 2.1: Boundary conditions used - LES simulation

Surface	**Boundary condition**
Inlet	Rescaling/recycling, δ_{in} = 0.02819 m
Outlet	$P_{total} = 0$
Top	Symmetry
Front	Symmetry
Back	Symmetry
Wing	No slip wall
Bottom	No slip wall

2.1.5. Grid

The solver used for the current LES studies, INCA, uses Cartesian grids which facilitate automatic grid generation and adaptive local grid refinement [37]. One advantage of the Cartesian grids is the fewer computational operations per grid point compared to body-fitted or unstructured grids [11]. However, the geometric boundaries do not generally coincide with the grid lines, due to which, implementing boundary conditions at the interfaces is not straightforward. To tackle that, a cut-cell based method immersed boundary method is used, which is suitable for any non-uniform staggered Cartesian grid [37]. The intersection of the solid obstacle with the Cartesian grid produces a set of cells that are cut by the boundary. The finite volume discretization is locally modified in these cells such that it only accounts for the part of the cells in the fluid regime. The method used in this solver is called Conservative Immersed Interface Method. A detailed description of this method is available in [11, 37].

Since an immersed boundary method is used, identical meshes can be used for both the baseline and anti-fairing cases, by only changing the immersed obstacle. Thus, any mesh related differences between the two cases are prevented, thereby, aiding in error cancellation. The mesh is generated using the built-in feature of the solver, called, Adaptive Mesh Refinement (AMR). This feature allows for selective mesh refinement around the region of interest, based on user defined criteria such as wall distance, boundary layer thickness. In the present work boundary layer thickness is used as the AMR criterion, which primarily tries to fit a minimum number of cells around the immersed body, within the region between the body and a normal distance specified by the user. Apart from the specified criterion, the levels of refinement can be controlled using two other parameters called AMR_RATIO and MAX_LEVEL. AMR_RATIO defines the extent of successive levels of refinement. For example, in the present work, AMR_RATIO is taken as 3, which implies that the successive levels of refinement is achieved by splitting each cell into three. This is shown in Figure 2.4. MAX_LEVEL defines the number of iterations of the refinement levels specified by AMR_RATIO. For example, if MAX_LEVEL = 2, the refinement process is carried out twice, thus doubling the total number of cells in the region of interest. Therefore, the basic procedure is to start with a very coarse mesh in which the body of interest is immersed, which is then successively refined in specific regions of interest based on the parameters AMR criterion, AMR_RATIO and MAX_LEVEL to obtain the required mesh size and refinement. As shown in Figure 2.4, the maximum refinement region can be concentrated very close to the wing and the bottom plane so that the junction flows features can be accurately captured.

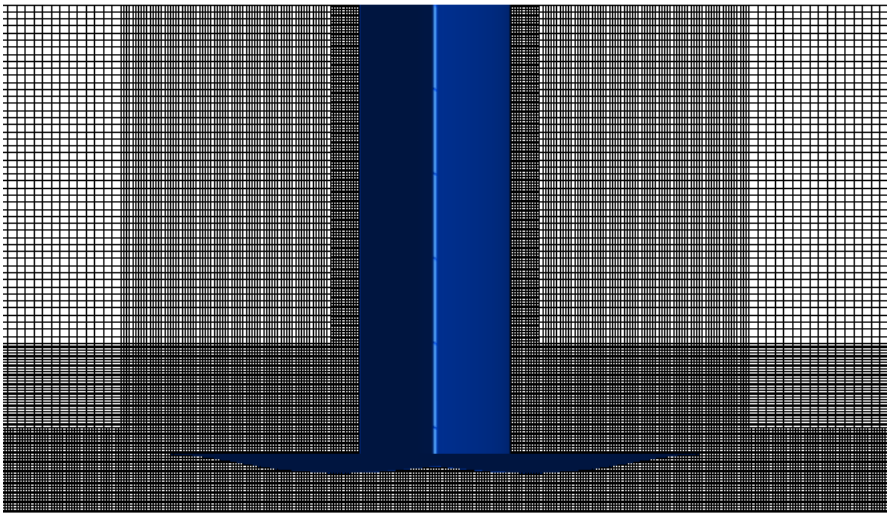

Figure 2.4: Three levels of refinement around the wing

To finalize the mesh size required, a preliminary grid point estimation technique was employed based on the relations provided by Choi *et al* [12]. The relations given are applicable for the boundary layer development over a flat plate. To use these relations on the current computational domain, the domain is split into

regions of approximate flat plates, as shown in Figure 2.5. Also, the wing is assumed to be composed of two flat plates whose width and length are taken as the wing chord and span respectively. The estimation was done for both wall-modeled (N_{wm}) and wall-resolved (N_{wr}) LES. According to the relations, the minimum number of points required for each case is given as:

$$N_{wm} = 54.7 \frac{L_z}{L_x} n_x n_y n_z Re_{L_x}^{2/7} \left[\left(\frac{Re_{L_x}}{Re_{x0}} \right)^{5/7} - 1 \right], \tag{2.10}$$

$$N_{wr} = 0.021 \frac{n_y}{\Delta x_w^+ \Delta z_w^+} \frac{L_z}{L_x} Re_{L_x}^{13/7} \left[1 - \left(\frac{Re_{x0}}{Re_{L_x}} \right)^{6/7} \right], \tag{2.11}$$

where L_z and L_x are the lengths of the flat plates in x and z direction respectively, Re_{L_x} is the Reynolds number based on the length of the flat plate, Re_{x0} is the Reynolds number at the inlet of the flat plate, $x0$. $n_x n_y n_z$ in the case of N_{wm} is the number of grid points required in each direction to resolve the computational volume of δ^3, where δ is the boundary layer thickness at a streamwise location. However, n_y in the case of N_{wr} is the number of grid points in the vertical direction required to resolve a vertical distance of $y+ = 100$. Δx_w^+ and Δz_w^+ are the assumed uniform grid spacing in the streamwise and spanwise directions respectively to resolve the near wall region.

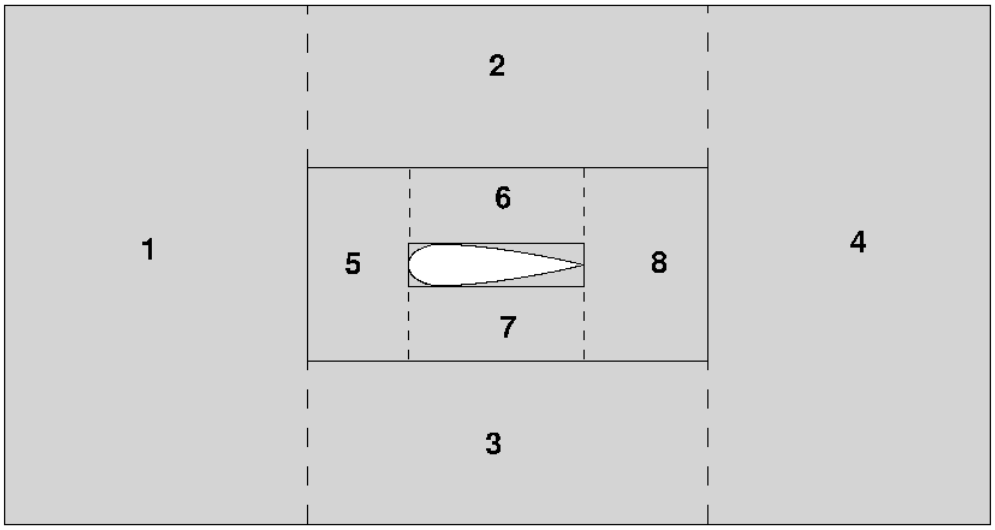

Figure 2.5: Top view of the LES domain which shows splitting of the domain into regions of flatplate to estimate the required grid points. Image is not to scale

Based on these relations, the minimum required grid points for each case was found to be N_{wm} = 11 million and N_{wr} = 73 million. Taking the available computational resources into account, 73 million was found to be too expensive to run both the baseline and anti-fairing LES cases. Therefore, wall-modeled LES is chosen for the current study. The grid used for the current studies consists of 24.3 million cells in the entire domain, which is higher than the computed minimum grid points for wall-modeled LES. The near wall cell size (taken as the length of the first cell normal to the wall) of both the wing and the bottom plane is $y = 1.1 \times 10^{-3}$, which corresponds to a dimensionless wall distance of $y^+ = 78$. This means that the first cell is within the logarithmic layer of the universal law of wall bounded turbulence (Figure 2.6). A unified wall function, which is applicable over the entire inner layer of wall bounded flows (viscous sublayer, buffer layer and inertial sublayer), called the Generalized Wall Function is used to model the near wall stresses and velocities. This formulation was proposed by Shih *et al* and is valid for various pressure gradients, complex flows with acceleration, deceleration and recirculation [52].

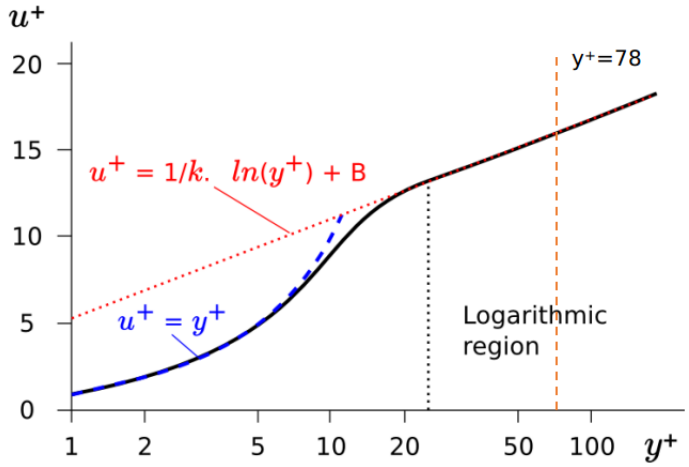

Figure 2.6: Universal law of wall bounded turbulence

2.1.6. Solver details

Both the LES are solved using a finite volume LES solver called INCA. Incompressible filtered Navier Stokes equations are solved on a staggered mesh, where time integration is done using a 3rd order explicit Runge-Kutta method. Standard second-order centered differences are used to discretize the viscous fluxes. The advective terms are discretized using a disceretization scheme called Adaptive Local Deconvolution Method (ALDM), which facilitates the use of implicit LES modelling. As explained previously, in implicit LES, the truncation error of the convective terms acts as the SGS model necessary to close the filtered Navier-Srokes equations. The ALDM scheme uses a discretization based on solution-adaptive deconvolution where parameters are determined specifically in such a way that the truncation error properly models the subgrid-scale energy transfer [36]. This type of modelling negates the necessity of a separate SGS model, since it directly provides the necessary closure model from the discretization error, which is an inherent part of any discretization scheme. The solver has been validated through various cases as presented in [11, 36, 64].

Dynamic time stepping is used to ensure that the CFL number is equal to 1 at every time step. CFL number is defined as,

$$CFL = \frac{U\Delta t}{\Delta x}, \tag{2.12}$$

where U is the instantaneous velocity within a cell, Δt is the time step size and Δx is the cell size. To ensure stability of the simulation, CFL must be maintained less than or equal to 1 [13]. This is ensured in the present work by assigning the time step size to the minimum of time step sizes of all the cells, which are calculated from the above formula by taking $CFL = 1$. The average time step size over all the time steps of the simulation is around $\Delta t = 2\times10^{-5}$. The simulation is initially run for 100 chord-based flow throughs (c/U_{ref}) to eliminate the starting transients and transients due to the rescaling/recycling boundary conditions. To ensure statistical stationarity, time averaged and instantaneous values of all the three components of velocity and pressure were monitored at various locations. These are shown below for two locations.

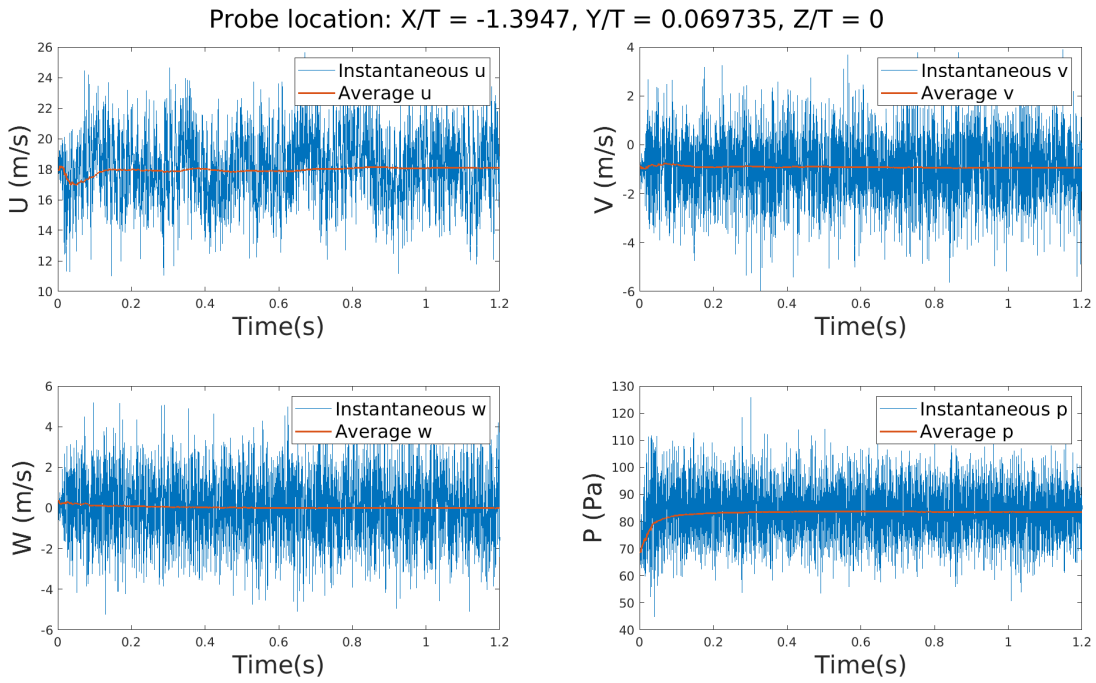

(a)

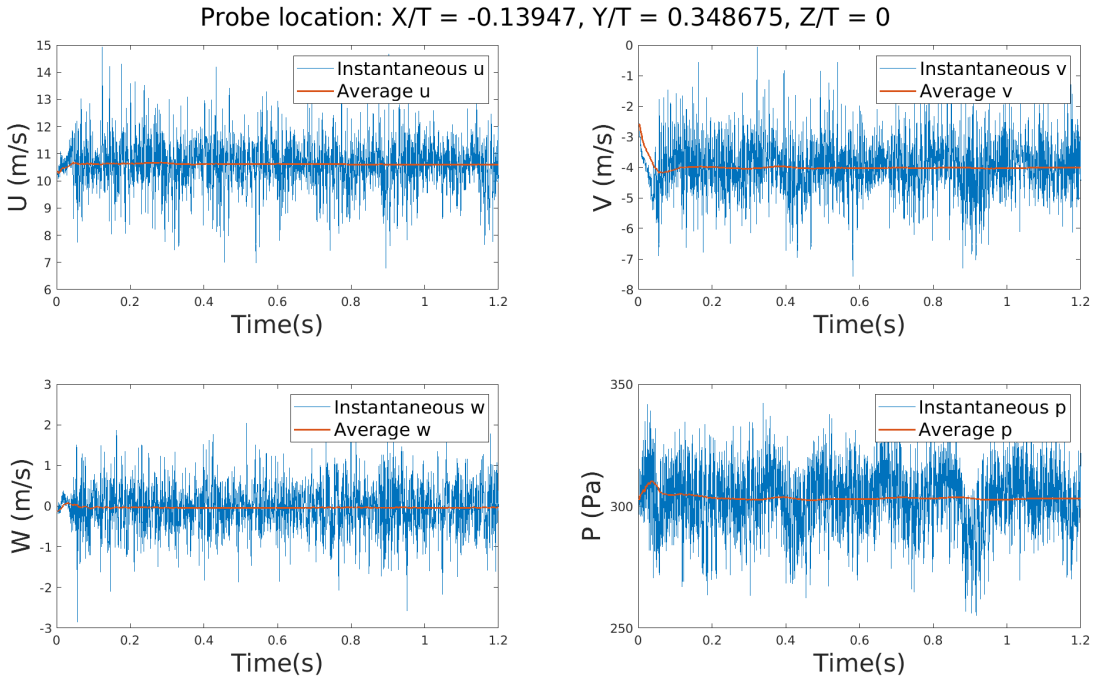

(b)

Figure 2.7: Average and instantaneous flow quantities at various locations

As can be observed, all the flow parameters are approximately stationary well before 1.2 s. The wing leading edge is at $X/T = 0$. The first probe location is thus well away from the wing but very close to the bottom wall, which is marked by the high frequencies in the instantaneous flow parameters. These higher frequencies and fluctuations are an indication of the near wall turbulence. The second probe location is taken much closer to the wing compared to the first, whereas the vertical coordinate is away from the bottom surface. Consequently, the velocities are much smaller, while the pressure is much larger for the second probe. Once the transient stage is done, the simulation is run for another 100 chord based flow throughs to gather the statistics of the flow parameters. The norm of residuals of the continuity equation was ensured to

be less than 10^{-5} at every time step.

2.2. RANS simulation

2.2.1. Governing equations

To derive the RANS equations, we again start from the Navier-Stokes (NS) equations for an incompressible, Newtonian fluid:

$$\frac{\partial U_i}{\partial x_i} = 0, \tag{2.13}$$

$$\rho\frac{\partial U_i}{\partial t} + \rho\frac{\partial U_i U_j}{\partial x_j} = -\frac{\partial P}{\partial x_i} + \frac{\partial}{\partial x_j}\left[\mu\left(\frac{\partial U_i}{\partial x_j} + \frac{\partial U_j}{\partial x_i}\right)\right], \tag{2.14}$$

The RANS equations are obtained from these by applying Reynolds decomposition to the velocity and pressure terms and finally applying averaging to the entire equation. The decomposition is given as :

$$U_i = < U >_i + u_i', \tag{2.15}$$

$$P = < P > + p', \tag{2.16}$$

where $< \phi >$ represents the mean component and ϕ' denotes the fluctuating part of the flow variable. Substituting these into the NS equations and applying the averaging operator to them results in the RANS equations. These are shown below. Note that the time varying term is dropped, thus representing the steady state RANS equations.

$$\frac{\partial < U_i >}{\partial x_i} = 0, \tag{2.17}$$

$$\rho\frac{\partial(< U_i >< U_j >)}{\partial x_j} = -\frac{\partial < P >}{\partial x_i} + \frac{\partial}{\partial x_j}\left[\mu\left(\frac{\partial < U_i >}{\partial x_j} + \frac{\partial < U_j >}{\partial x_i}\right)\right] - \rho\frac{\partial < u_i' u_j' >}{\partial x_j}, \tag{2.18}$$

The only term that is different from the NS equation is the last term on the right. This term represents the gradients of Reynolds stresses ($-\rho < u_i' u_j' >$) that is present due to the turbulent, fluctuating nature of the flow. To close these set of equations the Reynolds stresses need to be modelled. In the current study, a variant of the eddy viscosity model is used to close the RANS equations. Eddy viscosity model was chosen because this was the model of choice of various authors [4, 42, 48] in their RANS analysis, given its relatively lesser computational expenses and reasonable accuracy. This type of modelling makes use of the Boussinessq approximation, which gives a method to approximate the Reynolds stresses using the strain rate tensor (S_{ij}). This is given as:

$$-\rho < u_i' u_j' > + \frac{2}{3}\rho k\delta_{ij} = \mu_t\left(\frac{\partial < U_i >}{\partial x_j} + \frac{\partial < U_j >}{\partial x_i}\right) = 2\mu_t S_{ij}, \tag{2.19}$$

where k is the turbulent kinetic energy and μ_t is called the eddy viscosity or turbulent viscosity. Substituting this into the steady RANS equation,

$$\rho\frac{\partial(< U_i >< U_j >)}{\partial x_j} = -\frac{\partial P_{eff}}{\partial x_j} + \frac{\partial}{\partial x_i}\left[\mu_{eff}\left(\frac{\partial < U_i >}{\partial x_j} + \frac{\partial < U_j >}{\partial x_i}\right)\right], \tag{2.20}$$

where $\mu_{eff} = \mu + \mu_t$ is the effective viscosity and $P_{eff} = < P > + \frac{2}{3}\rho k$ is the modified mean pressure. The above equation is now exactly same as the steady NS equations, with $< U >$ instead of U, μ_{eff} instead of μ and P_{eff} instead of P. However, μ_t still needs to be modelled to solve the equation. Various models exist based on the method of computing μ_t. The current study uses Menter's SST variant of $k-\omega$ model [35], which involves solving two additional transport equations for turbulent kinetic energy (k) and specific dissipation rate (ω) to represent the eddy viscosity (μ_t). These transport equations can be found in [35].

2.2.2. Wing junction geometry

The Rood wing was chosen for LES to validate the baseline case with the experimental results by Devenport *et al* [14]. However, for the RANS analysis, two different wing geometries are considered:

- The first is the same Rood wing with the exact dimensions as the one used in LES analysis. The analysis using this wing serves two purposes:
  - To validate the RANS solver parameters and discretization schemes by comparing with the LES results
  - To also compare the LES and RANS results and thereby comment on the differences between the two
- A NACA 0015 which will be used to perform the study of different approach boundary layer and anti-fairing thicknesses.

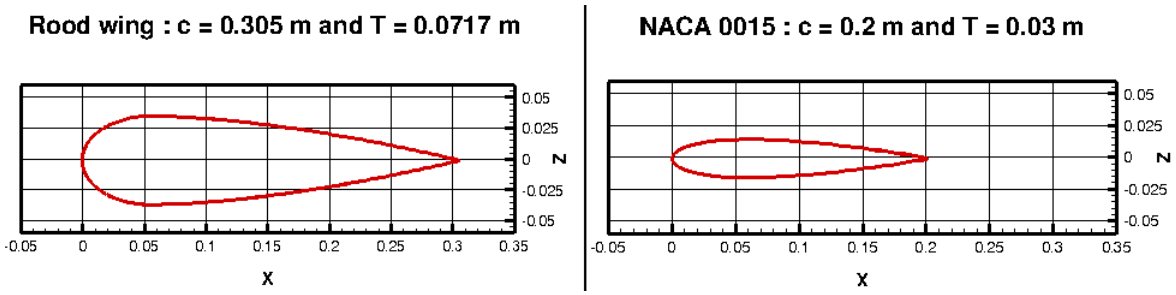

Figure 2.8: Cross sections of the Rood wing and NACA 0015 wing used in the current RANS study

The cross sections of the two wings are shown in Figure 2.8. NACA 0015 is chosen as the wing geometry because the results could be added to the existing works of Belligoli [7] and Koers [28], since both of them had used the same wing in their analysis. Moreover, the Rood wing is a significantly thicker wing, which is rarely used in practical applications nowadays. The NACA 0015 wing has a wing chord length of $c = 0.2m$, with the maximum thickness as 15% of the chord, *i.e.* $T = 0.03m$. As for the anti-fairing geometry, the shape and size of the baseline anti-fairing case is exactly the same as the one used in the LES study. Different depths of the anti-fairing are obtained by scaling the geometry of the anti-fairing only along the vertical direction. Table 2.2 shows different anti-fairing depths investigated in the current study. Also an example of two different anti-fairing thicknesses are shown in Figure 2.9. Different depths are studied to gauge the drag reduction performance of the anti-fairing at each of these depths. The anti-fairing depth is chosen as a parameter to study because the primary drag reduction mechanism proposed by Belligoli *et al* [7] is due to the higher pressure on the upstream dent of the anti-fairing, thus it would be interesting to study the effect of varying the depth of this dent on the drag reduction capacity of the anti-fairing.

Table 2.2: Different anti-fairing depths investigated

S.no	Case name	Maximum depth of anti-fairing (m)
1	AF_0.5	0.00312
2	AF_0.75	0.00468
3	AF_1 (baseline)	0.00624
4	AF_1.25	0.00780
5	AF_1.5	0.00936

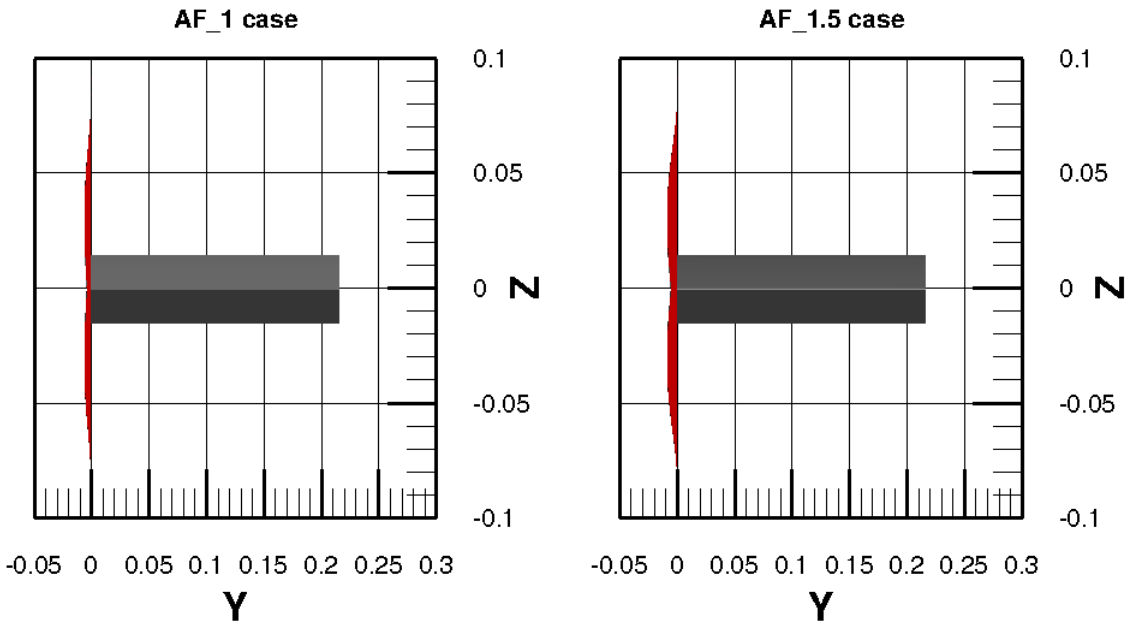

Figure 2.9: Example of two different depths of anti-fairings used in the current RANS study

2.2.3. Computational domain

The domain considered is again a rectangular box which encloses the wing (Figure 2.10). The inlet plane is located $1.53c$ upstream of the wing leading edge, while the outlet plane is $2.8c$ downstream of it. The front and the back planes are situated $2.2c$ in front and back of the wing tip respectively. The top plane is located at $y = 0.2151m$, while the bottom plane, which has the anti-fairing has a variable location, depending on the case investigated. As for the Rood wing analysis, the computational domain considered is exactly the same as the one used for LES. This is to ensure same wetted surface area of the wall regions, such that the integrated loads could be directly compared.

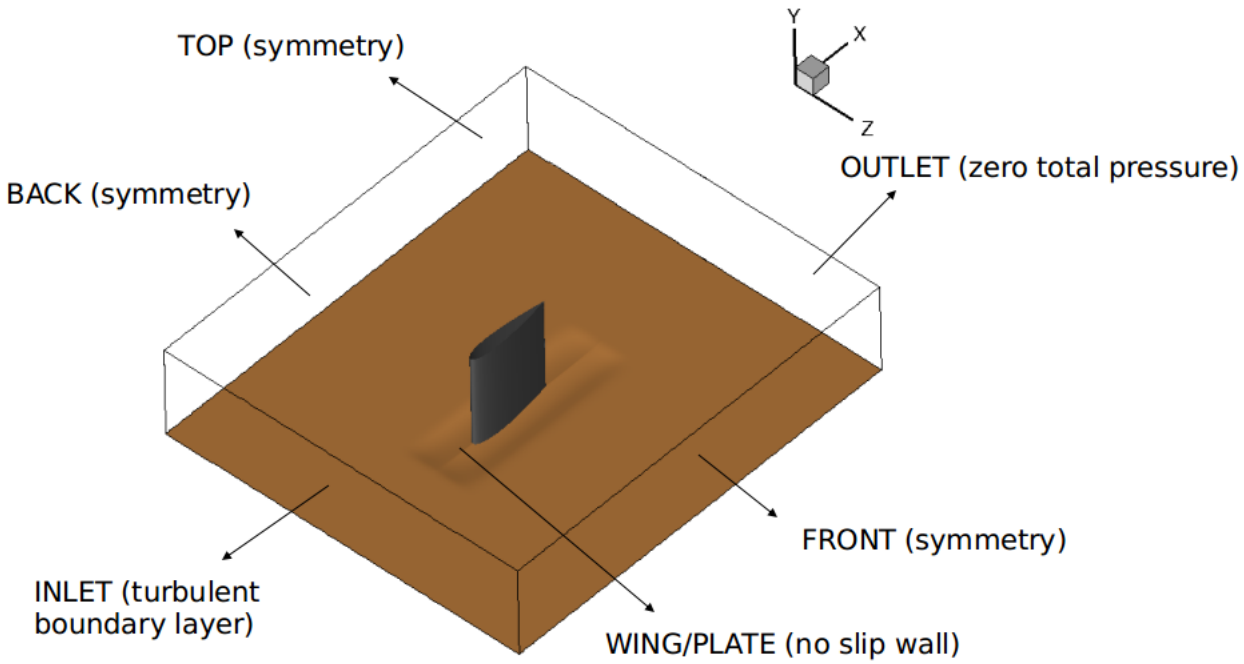

Figure 2.10: Computational domain used for RANS

2.2.4. Boundary conditions

Unlike the LES simulation, it is not necessary to have a time varying inlet boundary condition for a steady RANS simulation. A fixed turbulent inlet boundary layer is given as the inflow condition, where the velocities are constant in the spanwise direction and only vary along the vertical direction. The inlet boundary layer thickness is fixed for the baseline anti-fairing case (AF_1) such that the momentum thickness based Reynolds number, $Re_\theta = 6700$ at $2.15T$ upstream of the wing, as given by Devenport *et al* [14]. As with the LES case, the relations by Choi [12] is used to calculate the thickness value. Using these relations, the inlet boundary layer thickness for the AF_1 case came out to be $\delta = 0.0331m$. As with the anti-fairing depth, inlet boundary layer thickness is also chosen as a varying parameter to study the effect on the drag reduction capacity of anti-fairing. Other cases with different inlet boundary layer thicknesses are obtained by scaling the value corresponding to the AF_1 case. If the inlet boundary layer thickness is varied, the boundary layer developing over the anti-fairing also changes, thus facilitating the study of the effect of different boundary layer thicknesses developing over the anti-fairing on its drag reduction capabilities. All the inlet boundary layer thicknesses investigated in this study are shown in Table 2.3.

Table 2.3: Different inlet boundary layer thicknesses investigated

S.no	Case name	Inlet BL thickness (m)
1	BL_0.5	0.01655
2	BL_0.75	0.024825
3	BL_1 (baseline)	0.0331
4	BL_1.25	0.041375
5	BL_1.5	0.04965

For the Rood wing analysis, the inlet boundary layer thickness is the same as the one used for LES, *i.e.* $\delta_{Rood} = 0.02819m$. To generate the boundary layer, implicit relation for flat plate boundary layer development proposed by Spalding [58] are used, which is given by:

$$y^+ = u^+ + 0.1108\left[e^{0.4u^+} - 1 - 0.4u^+ - \frac{(0.4u^+)^2}{2!} - \frac{(0.4u^+)^3}{3!} - \frac{(0.4u^+)^4}{4!}\right], \tag{2.21}$$

$$y^+ = \frac{yu_\tau}{\nu}, \tag{2.22}$$

$$u^+ = \frac{u}{u_\tau}, \tag{2.23}$$

where y is the wall normal coordinate, u_τ is the wall friction velocity and u is the streamwise velocity at every y-location. The y coordinates of all the cell centres of the inlet plane are extracted from the mesh data. Then, using a MATLAB script, velocities (u) at every y location is obtained using the above implicit relations. The wall friction velocity is obtained for a given δ using the flat plate relations given by Choi [12]:

$$c_f = 0.02Re_\delta^{-1/6}, \tag{2.24}$$

$$u_\tau = \sqrt{1/2U_{ref}^2 c_f}, \tag{2.25}$$

Figure 2.11 shows the boundary layer generated for $delta = 0.02819$ and it is compared with the one from LES, which was obtained from the rescaling/recycling boundary condition. The shape of the Spalding boundary layer matches the one from LES, with the velocities slightly over predicted in the Spalding case.

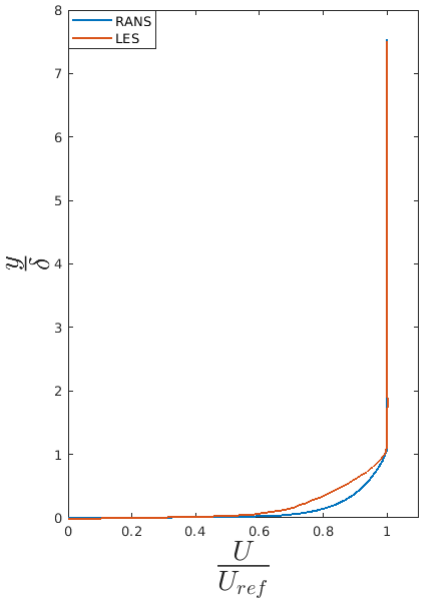

Figure 2.11: Example of inlet turbulent boundary layer generated using Spalding's law ($\delta = 0.02819m$)

Other boundary conditions are the same as given in the LES case. The outlet has zero total pressure boundary condition and all other variables are extracted from the specified pressure value. The top, front and back planes are given as symmetry boundary conditions and finally, the wing and the bottom surface are given no slip wall boundary condition. All the boundary conditions are summarized in a table below.

Table 2.4: Boundary conditions used - RANS simulation

Surface	**Boundary condition**
Inlet	Fixed turbulent boundary layer, δ_{in} = 0.0331 m (for AF_1 case)
Outlet	$P_{total} = 0$
Top	Symmetry
Front	Symmetry
Back	Symmetry
Wing	No slip wall
Bottom	No slip wall

2.2.5. Grid

All the meshes required for the RANS simulations are generated using the commercial meshing software ANSYS ICEM CFD [1]. A structured grid with selective mesh refinement around the wing and the bottom plane is created, which comprises completely of hexahedral cells. The selective refinement is made possible by dividing the entire domain into several blocks and refining only the blocks surrounding the wing and the bottom plane. Also, special care was taken to bias the spacing of the cells such that cells closer to the wall regions are much smaller and satisfy the required first cell size which corresponds to a $y^+ = 50$ (Figure 2.12).

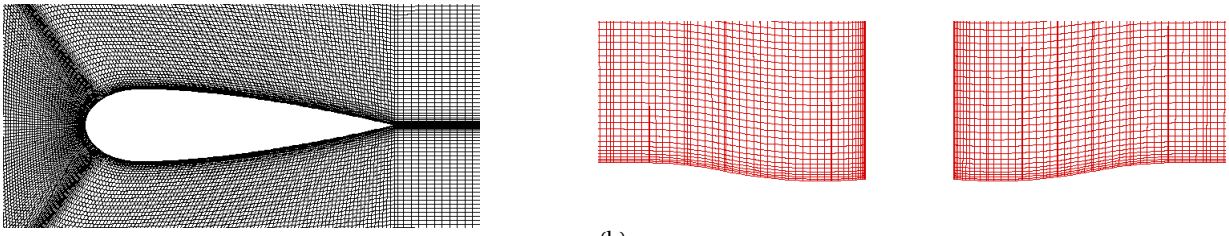

(a) (b)

Figure 2.12: Overview of mesh near the wall regions

To decide the number of cells required to conduct the RANS analysis, a grid convergence study is conducted on the AF_1 anti-fairing case. The study is conducted based on the proposed method by Roache [47]. Different grids considered for the study are listed in the table below. The Grid Convergence Index (GCI) is calculated using two parameters, the total lift and the total drag force, to make sure the selected mesh is in the asymptotic range of convergence. Though five grids are used in the study, GCI is computed only using GRID_1, GRID_2 and GRID_4, which have a constant refinement ratio of $r = 1.5$. The other grids are just used for plotting the lift and the drag values and study the change in them. Assuming the average grid spacing for the finest grid (GRID_1) is $h = 1$, the average grid spacings for the grids GRID_2 and GRID_4 normalized by the grid spacing of the finest grid are $h = 1.5$ and $h = 2.25$ respectively. First, the order of convergence p is calculated:

$$p = ln\left(\frac{F_4 - F_2}{F_2 - F_1}\right) / ln(r), \tag{2.26}$$

where F_i is the load value obtained using the grid GRID_i. Once p is determined, the theoretical value of the load if the grid spacing asymptotically reaches zero, is calculated using the Richardson extrapolation:

$$F_{h=0} \approx F_1 + \frac{F_1 - F_2}{r^p - 1}, \tag{2.27}$$

The theoretical zero grid spacing values are obtained for both the lift and drag forces. These forces, along with the forces obtained for other grids are non-dimensionalized using the reference dynamic pressure ($0.5\rho U_{ref}^2$) and reference area (Tc) and are plotted in Figure 2.13. It should be noted that both the forces comprises of the complete wing/anti-fairing system. Both these plots are shown below.

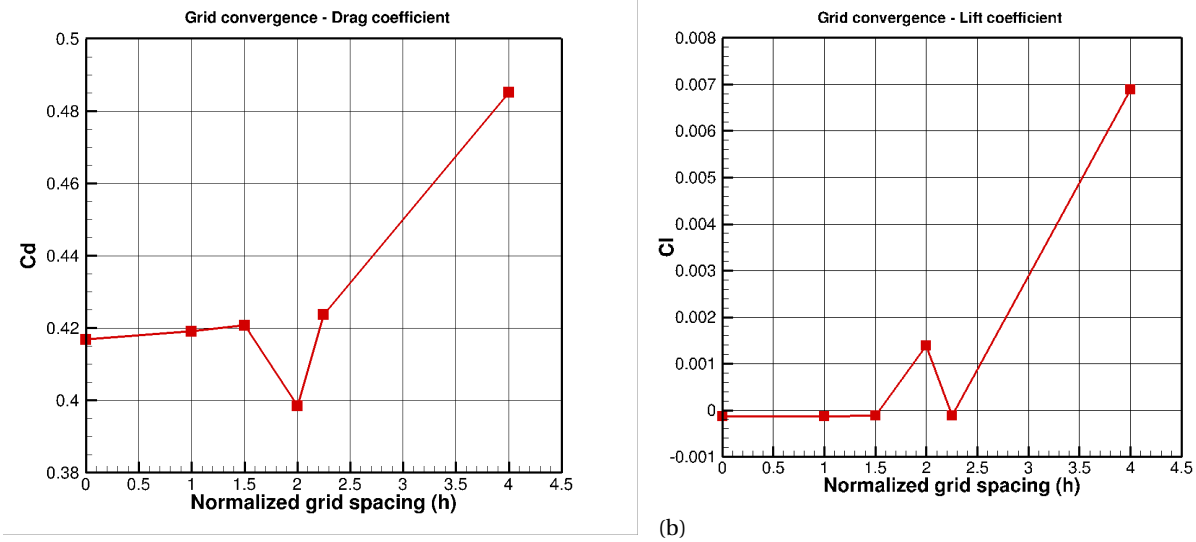

(a) (b)

Figure 2.13: Grid convergence study for RANS. $h = 0$ indicate the Richardson-extrapolated value

It is clearly seen that both the plots shown asymptotic convergence for the finest grid GRID_1. To ensure this, GCI is calculated between GRID_1 and GRID_2 using both the lift and drag forces. Thus,

$$GCI(\%) = 100\frac{F_s|\epsilon|}{r^p - 1}, \tag{2.28}$$

$$\epsilon = \frac{F_2 - F_1}{F_1}, \tag{2.29}$$

where the recommended factor of safety (F_s) to calculate GCI is taken as 1.25 for three or more grids [47]. The safety factor can be thought of representing a 95 % confidence bound on the estimated relative error [47]. Using the above relations, $GCI_{drag} = 0.63\%$ and $GCI_{lift} = 0.64\%$. These indicate that on further refinement of the grid (with a ratio of 1.5), the change in the drag and lift force values are approximately 0.63% and 0.64 % respectively, which are reasonably small. Hence the fine grid GRID_1 is used for all the RANS simulations.

2.2.6. Solver details

All the RANS simulations in the current study are performed using the open source finite-volume solver, OpenFOAM. The steady, incompressible RANS equations are solved using the built-in solver called Simplefoam. It solves the fully turbulent RANS equations in which the pressure-velocity coupled equations are solved using the SIMPLE (Semi-Implicit Method for Pressure Linked Equations) algorithm [10]. $k-\omega$ SST turbulence closure model has been used to close the RANS equations. This is chosen because it has been reported by Apsley *et al* [4] that SST models capture the mean flow features better among all the eddy-viscosity models for junction flows. Also, this was the model of choice for the RANS analysis done by Ryu $etal$ [48]. For all the simulations, 2000 iterations were carried out to obtain the necessary convergence. The solution was assumed to be converged if all the residuals of the flow parameters (U, V, W, p, k, ω) are in $O(10^{-5})$, as can be seen in Figure 2.14. Also, the change in the total drag force coefficient on the wing/anti-fairing junction for every iteration was monitored (Figure 2.15). It can be seen that the Cd values showed negligible difference ($O(10^{-9})$) after about 600 iterations.

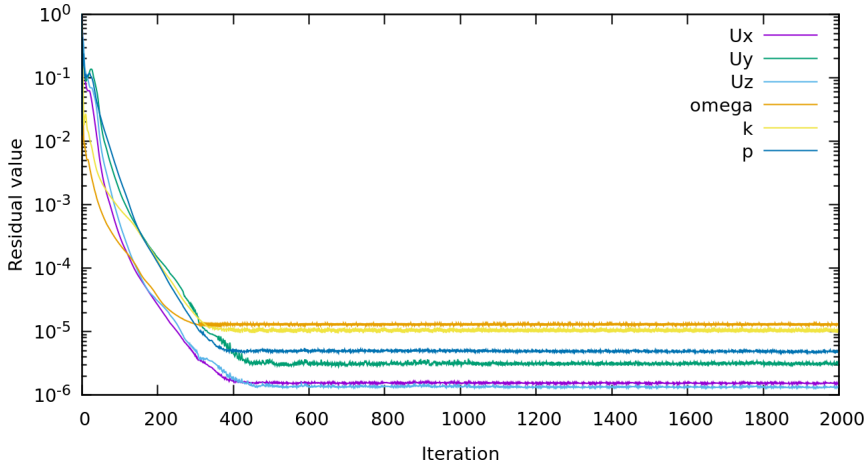

Figure 2.14: Residuals obtained for RANS analysis of AF_1 case

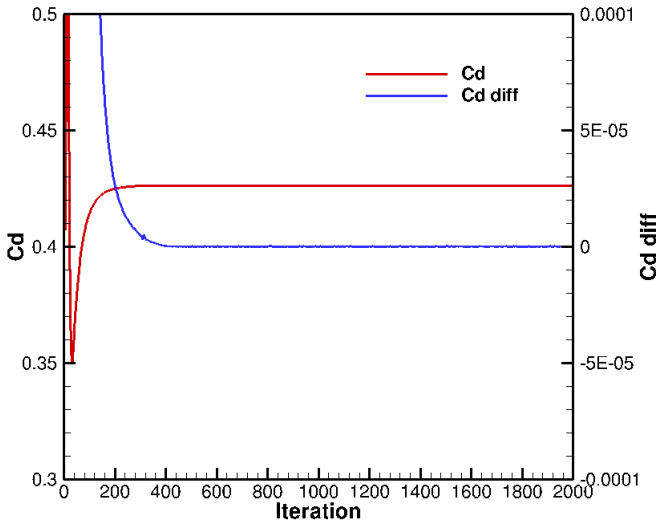

Figure 2.15: Drag coefficient convergence obtained for RANS analysis of AF_1 case. Left vertical axis denotes the value of Cd and right vertical axis denotes the absolute difference in Cd between successive iterations

3

Results and discussion: LES

This chapter discusses the results obtained from the LES for both the baseline and the anti-fairing cases. First, the baseline case is validated with the results from the available literature. Once, that is done, a comparison study is done between the baseline and the anti-fairing cases to observe the effect of the presence of the anti-fairing.

3.1. Comparison of baseline case with literature

3.1.1. Upstream boundary layer profiles

The first comparison is the boundary layer profiles at various locations upstream of the wing location. This comparison is done to make sure that the inlet boundary condition results in a realistic turbulent boundary layer that is comparable to the upstream boundary layers from the experiments of Devenport *et al* [14]. All the profiles are obtained from the symmetry plane ($Z = 0$), which cuts the wing into two halves. These are shown below in Figure 3.1. It should be noted that the velocity is non-dimensionalized with the reference velocity ($U_{ref} = 27\ m/s$) and the X and Y coordinates are non-dimensionalized by the maximum thickness of the wing $T = 0.0717m$

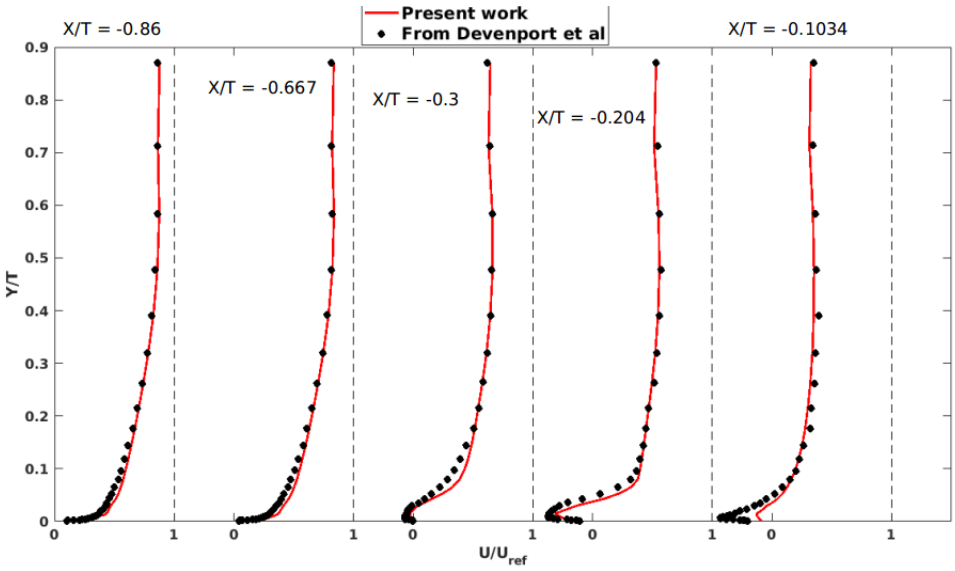

Figure 3.1: Boundary layer comparison at different upstream locations in the symmetry plane

It can be seen that overall, there is very good agreement between the LES and the experimental results. Moving closer to the wing, which is at $X/T = 0$, regions of backflow can be observed near the wall. This is due to the flow separation and subsequent flow reversal that occurs because of the strong adverse pressure

gradient imparted by the wing. According to Devenport *et al*, flow separates at $X/T = -0.47$ and further downstream, flow reversal occurs. This is nicely captured by the LES, as can be seen from the last three stations. For the region closest to the wall, the backflow velocity is slightly under predicted by the LES. This is because of using wall-modelled LES, due to which not many cells are present very close to the wall to perfectly capture the complete reversed flow region. Agreement in the boundary layer profiles confirms that the rescaling/recycling boundary condition used at the inlet of the domain has given realistic turbulent boundary layers.

3.1.2. Contours of *Cp* near the junction

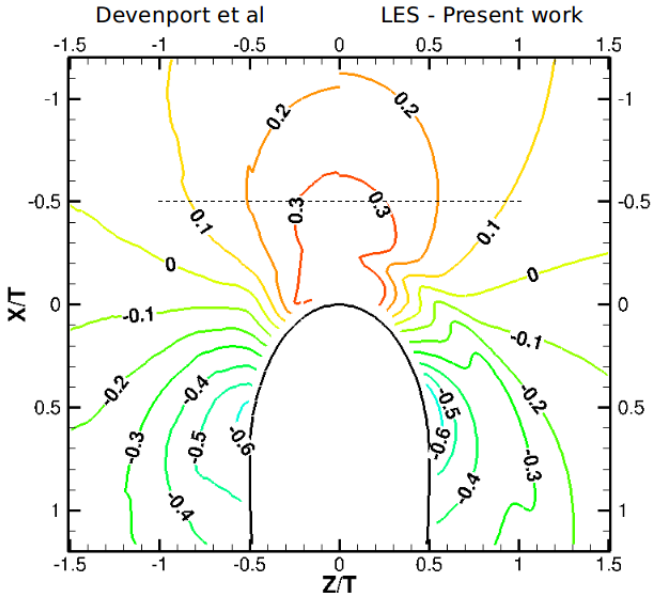

Figure 3.2: Comparison of the mean pressure coefficient contour on the flat plate - Left: Experimental results from Devenport *et al* [14] and Right: Present work. Dashed line shows the line along which C_p values are quantitatively compared in Figure 3.3

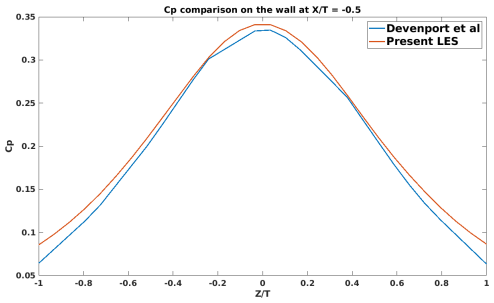

Figure 3.3: Quantitative comparison of C_p values along the dashed line shown in Figure 3.2

To validate the pressure values near the junction, contours of the time averaged pressure coefficient (C_p) near the wing/plate junction obtained from LES are compared with the experimental results of Devenport [14]. C_p is defined as:

$$C_p = \frac{< P > - P_\infty}{q},$$

$$q = \frac{1}{2}\rho U_\infty^2,$$

where $< P >$ and P_∞ are the mean local and freestream static pressures respectively, q is the freestream dynamic pressure calculated from freestream velocity, U_∞ and the density, ρ. From Figure 3.2, a reasonable qualitative agreement between the present work the experimental results can be observed. Notable difference

is the presence of kinks in almost all the contour lines of the present work visible close to the wing surface which are not that significant in the experimental results. Ryu *et al* [48] report the presence of similar kinks in the contour lines of their RANS results, which they attribute to being numerical artifacts. However, they do not report the presence of kinks in their wall-resolved LES results. Moreover, similar kinks were also observed by Paik *et al* in their DES results [42], for which they haven't reported any particular reason. Presence of these in the RANS and DES indicate these could be an artifact of the wall model used in the current LES. The fact that the wall-resolved LES results of Ryu *et al* do not have these further strengthens the suspicion that these kinks are caused due to not resolving the near wall region. Apart from these kinks, other differences between the two are the slight over-estimation of the pressure values at spanwise locations further away from the wing. This is marked by a slight offset in the end position of the contour lines. To obtain a quantitative comparison, C_p values are plotted for both the cases on the wall along a straight line (shown in Figure 3.2) slightly upstream of the wing at $X/T = -0.5$. This is shown in Figure 3.3. The variation obtained from the present work matches quite well with that of the experimental results. The peak C_p is slightly under predicted by the LES, whereas the pressure is over-estimated at further spanwise locations away from the wing, as observed from the contour lines. Apart from the above mentioned points, there are no drastic differences between the present LES results and the literature. Overall, the near junction pressure field appear to be predicted with satisfactory accuracy.

3.1.3. Contours of time averaged spanwise vorticity

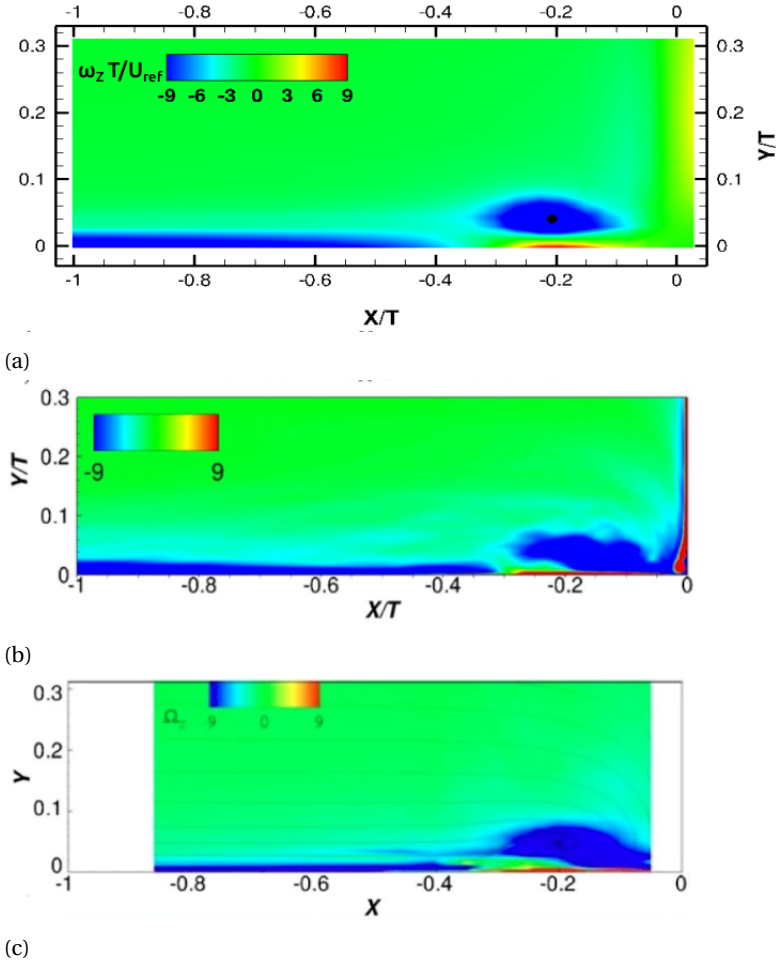

Figure 3.4: Mean spanwise vorticity comparison in the symmetry plane: a) Present work b) Fine grid LES from Ryu [48] c) Experimental results from Devenport [48]. Wing is at $X/T = 0$.

Contours of time averaged spanwise vorticty are extracted from the symmetry plane and are again compared with the LES results of Ryu and the experimental results of Devenport. This is a good indicator of the presence

of the HSV upstream of the wing leading edge. The contours are shown in Figure 3.4. Note that the vorticity is non-dimensionalized using T and U_{ref}. The location of the HSV is marked by the elliptical lump of negative vorticity centered approximately at $X/T = -0.2$, $Y/T = 0.5$ (black dot in the contour of the current LES study). As can be observed, the shape and the magnitude of the HSV is very nicely captured by the LES. Also, the small region of positive vorticity below the HSV structure is also predicted. The positive vorticity is the result of the intense backflow induced by the HSV, which was seen in the boundary layer plots shown in Figure 3.1. Apart from this, a trail of positive vorticity very close to the wing leading edge can be seen in the LES results of Ryu, which is not captured in the current study. This is again the result of not having enough cells near the wing region. Ryu *et al* had used a wall resolved simulation, which would bunch quite a number of cells near the wall regions, thus allowing to capture the highly localized positive vorticity.

3.1.4. Contours of time averaged turbulent kinetic energy

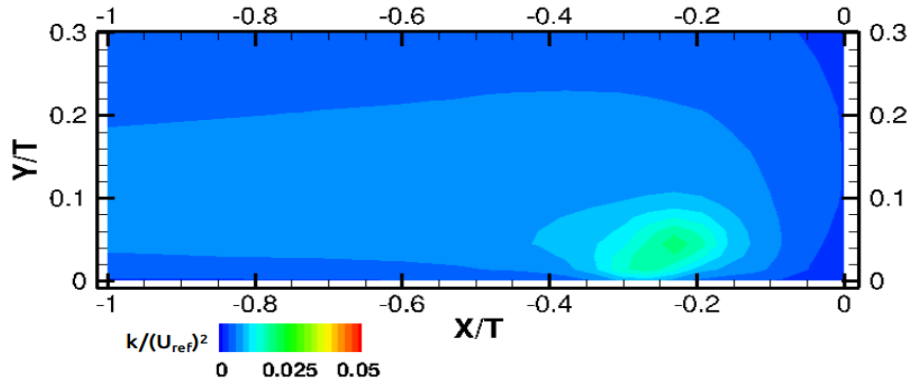

(a)

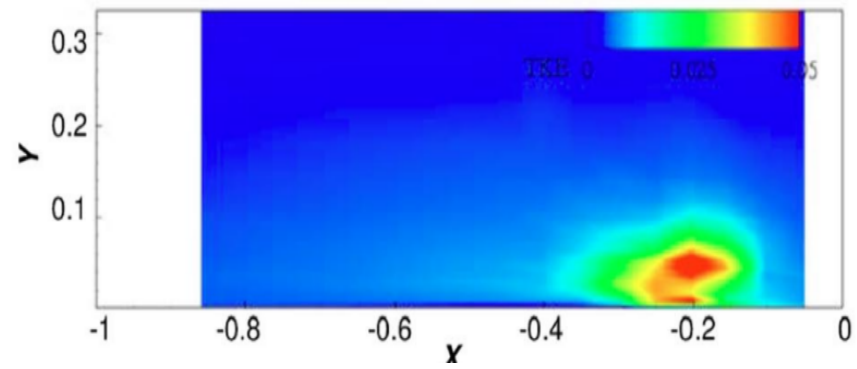

(b)

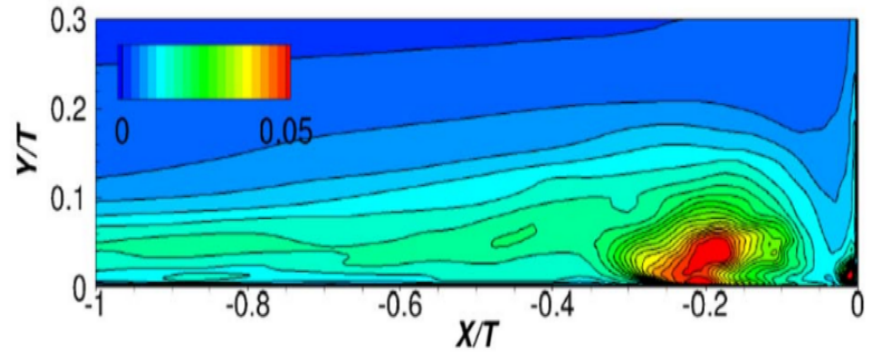

(c)

Figure 3.5: Mean turbulent kinetic energy comparison in the symmetry plane: a) Present work b) Experimental results from Devenport [48] c) Fine grid LES from Ryu [48]. Wing is at $X/T = 0$.

Figure 3.5 shows the comparison of contours of mean resolved turbulent kinetic energy (k, which does not include the subgrid scale kinetic energy) in the symmetry plane near the junction. The kinetic energy values are non-dimensionalized by U_{ref}^2. The region of high turbulence levels approximately coincides with the location of the HSV core, which can be seen in the current LES results as well. However, the current LES study under predicts the peak levels of the kinetic energy. The predicted peak value is about $k/U_{ref}^2 = 0.02$, whereas the results from Ryu *et al* and Devenport *et al* report $k/U_{ref}^2 = 0.05$. A similar under prediction was observed in the DES results of Paik *et al* [42] as well. This suggests that the under prediction could be a result of having modelled the near wall flow. It can be seen from the figure that the turbulent kinetic energy is concentrated very close to the wall. Since the near wall dynamics of the flow are not well resolved, the most of the energy carrying eddies might not have been captured by the wall model, resulting in an under prediction of the kinetic energy. Moreover, the region is dominated by flow reversal and separation and it has been reported by many authors [49, 57] that wall models always lack the necessary accuracy in predicting the turbulence in these regions.

Thus, all these comparisons with the available literature show that the LES results can be trusted for further analysis with the anti-fairing. The main flow feature of the junction flows is the location and magnitude of the HSV, which is very nicely captured by the present LES. Also, the boundary layer comparison clearly shows that the LES captures the region of intense backflow upstream of the wing, though the magnitude is slightly under predicted. The pressure contour comparison also show satisfactory validation of the present work. As for the turbulent kinetic energy comparison, the peak location in the symmetry plane matches with the literature, whereas the magnitude is greatly underestimated. However, further analysis only involves comparison between the baseline and anti-fairing cases, thus the absolute magnitude of kinetic energy is not much of a concern. Since exact same meshes are used for both the cases, it can safely assumed that both the cases will have similar under prediction of the near wall turbulent kinetic energy and comparisons can be done between the cases to draw physical conclusions on the performance of the anti-fairing. Thus, on the whole the LES results can be assumed to be validated.

3.2. Comparison between baseline case and anti-fairing

Now that the results of the baseline case has been validated, a comparison study is done between the baseline case (BL) and the anti-fairing case (AF) to observe the effects of the anti-fairing on various flow quantities.

3.2.1. Surface pressure coefficient contours

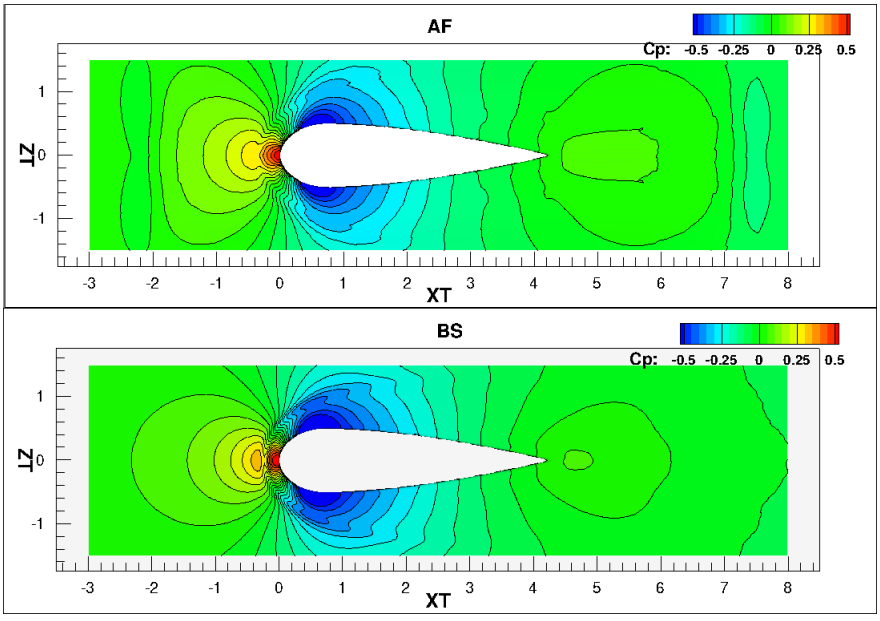

Figure 3.6: Surface pressure coefficient comparison

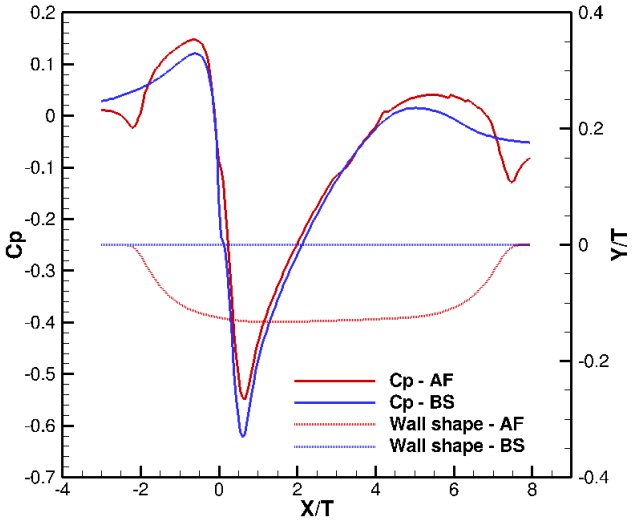

Figure 3.7: Surface pressure coefficient comparison on a line drawn at $Z/T = 0.6$

Figure 3.6 shows the comparison between surface pressure coefficient for the anti-fairing and the baseline cases. As expected, the pressure keeps increasing as we move towards the wing leading edge, where a stagnation point is formed. For the anti-fairing case, this increase is higher compared to BS, which is marked by the higher pressure in front of the wing. This is because, in front of the wing the surface is not flat as in the BS case, but has a convex dent (Figure 2.1). Within this dent, the flow is slowed down, thereby increasing the pressure in front of the wing. A clearer picture can be obtained by looking at Figure 3.7, which shows Cp comparison on a line just outside the wing ($Z/T = 0.6$). The shape of the bottom wall is also highlighted for both the cases. The higher pressure in the region front of the wing leading edge ($X/T = 0$) is quite apparent. Also, as explained in the previous chapter, this increase in pressure in front of the wing is the main reason for the drag decrease obtained for the anti-fairing. Around the wing, there does not seem to be much difference in Cp values between the two cases, as the anti-fairing is almost flat in this region. The flow is accelerated up to the thickest point of the wing and then decelerates further, which is marked by the rise in pressure from $X/T = 0.7$. In the wake of the wing, due to incomplete pressure recovery, the pressure is recovered gradually in the baseline case, whereas in the AF case, the pressure remains almost constant till the start of the concave dent. Within this dent, the pressure continues decreasing till the point where the anti-fairing reattaches the flat plate region. This is marked by the locally low pressure at $X/T = 7.5$. A similar low pressure region is present at the start of the anti-fairing as well, around $X/T = -2$. These two local low pressure zones can be attributed to the convex curvatures at the ends of the anti-fairing. The flow turning along the convex curvature results in an positive pressure gradient normal to the wall which is matched by the centripetal force. This positive gradient is achieved by a reduction in surface pressure along the convex curvatures. Similar observations were reported by Smits *et al* [54] in their study of flow over convex surfaces. Once the flow moves over the convex surface and reaches the flat plate region, pressure recovery starts to occur, which is marked by the increasing pressure from $X/T = 7.5$. The overall behaviour is exactly the same as reported by Belligoli *et al* [7], which confirms their theory of drag reduction due to the propulsive force upstream of the wing.

3.2.2. Flow quantities in the symmetry plane

Figure 3.8 shows the comparison of non-dimensional spanwise vorticity contours in the symmetry plane close to the junction. A drastic difference in the size, shape, magnitude and location of the vortex can be observed. In the AF case, the HSV seems to be concentrated in a region very close to the wall and its vertical span is significantly less compared to the baseline. Moreover, the magnitude of peak vorticity values are slightly less compared to the BS case. This consequently induces less backflow below the HSV core and thus a less positive vorticity is obtained for the AF case. Another interesting observation is the change in location of the advent of flow ejection from the wall surface. In the baseline case, this flow ejection from the wall occurs around $X/T = -0.4$, which corresponds to the break in the vorticity contour between the wall vorticity and the HSV. However, in the AF case, this location seems to have moved further upstream, around $X/T = -0.55$. Also, the HSV core centre seems to have moved from $X/T = -0.2$ for BS to $X/T = -0.32$. Thus, it can be seen that almost all aspects of the HSV such as the size, shape, magnitude and location seems to have been

significantly affected by the presence of the anti-fairing.

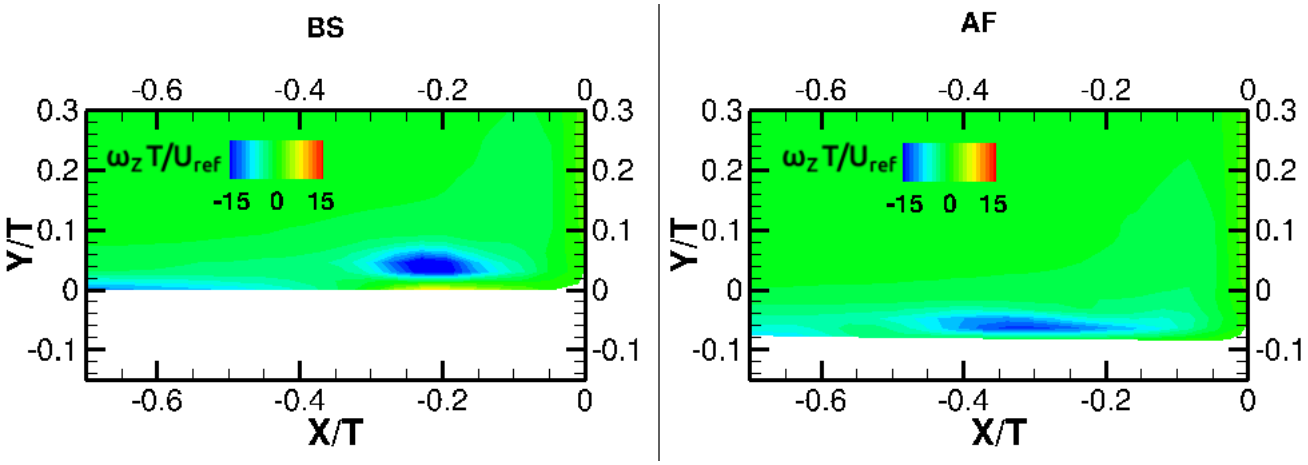

Figure 3.8: Normalized mean spanwise vorticity comparison in the symmetry plane

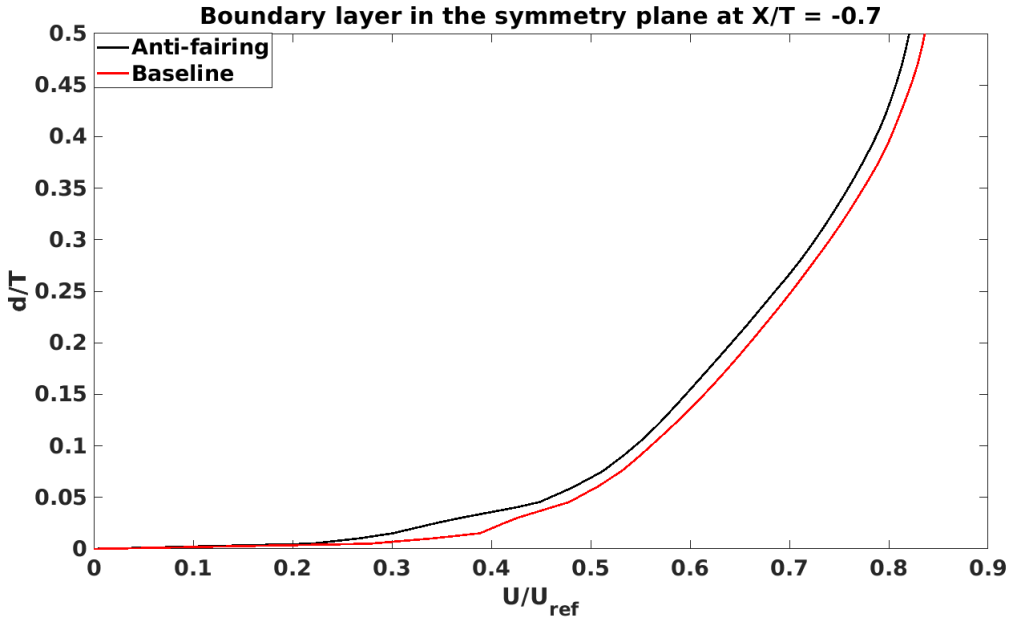

Figure 3.9: Upstream boundary layer comparison i the symmetry plane. The vertical axis denotes the non-dimensional distance from the wall d/T and not the vertical coordinate

To explain the reasons for these effects of anti-fairing on the HSV, it would be helpful to look at the upstream boundary layer profiles of both the cases before separation. This comparison is shown in Figure 3.9. It should be noted that the boundary layers are plotted with respect to distance from the wall (d) instead of the vertical coordinate since the bottom walls of these two cases are at different vertical positions. From the comparison plot, it is apparent that the boundary layer in the AF case has greater momentum deficit compared to the BS case, since the velocity is less in the AF case. This would mean that the AF case has greater approach momentum thickness compared to BL, and consequently greater Momentum Deficit Factor (MDF) (refer Equation 1.2). As reported by Fleming *et al* [18], as MDF increases, the HSV get concentrated much closer to the wall and its vertical extent above the wall is reduced. This is exactly the scenario for the AF case, which can be observed from the symmetry plane vorticity contour plot in Figure 3.8. The lesser momentum in the boundary layer should also be the reason for the shift in the separation location further upstream for the AF case. The weaker boundary layer in the case of AF has lesser energy to withstand the adverse pressure gradient exerted by the wing, thereby separating earlier compared to the baseline case. The increase in the

momentum thickness can be attributed to the shape of the anti-fairing in front of the wing. The convex shape of the anti-fairing slows down the fluid within the dent, which is also accompanied by the increase in surface pressure, as observed in Figure 3.7. Thus, it can be concluded that the presence of the anti-fairing results in decreasing the approach momentum thickness of the flow which consequently results in reduction of the HSV size and upstream shift of the HSV core and separation location.

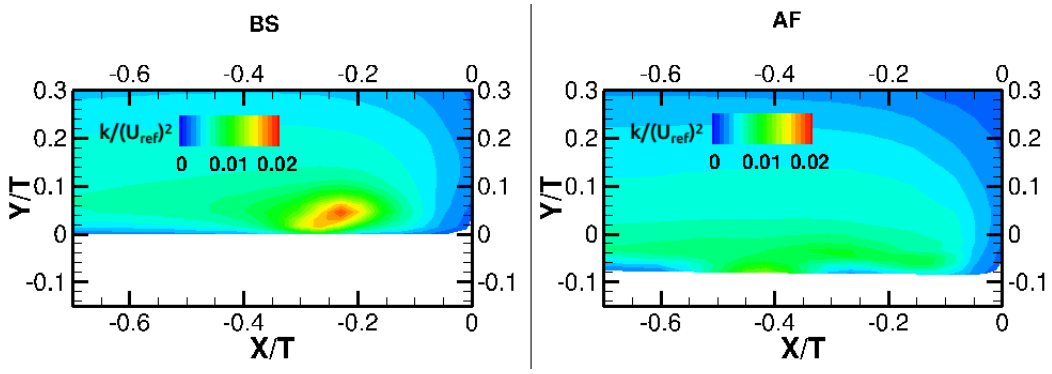

Figure 3.10: Normalized mean turbulent kinetic energy comparison in the symmetry plane

The next comparison is between the contours of mean turbulent kinetic energy in the symmetry plane near the junction for both the cases. These are shown in their non-dimensional form in Figure 3.10. As expected, high turbulent kinetic energy is localized to the region of the HSV, with the peak values around the respective centres of the HSV structures shown previously. An obvious observation is the significant dampening of the peak values of kinetic energy in the AF case. The peak value has reduced from $k/U_{ref}^2 = 0.02$ in the BS case to $k/U_{ref}^2 = 0.012$, amounting to a reduction of about 40%. It can be clearly seen that the reduction in the size and magnitude of the HSV in the junction is accompanied by a reduction in peak turbulence values. This behaviour has been reported for various conventional drag reduction mechanisms discussed previously, where active flow control or leading edge devices were used to curb the HSV. The reduction in turbulent kinetic energy is again believed to be an effect of the convex curvature of the anti-fairing upstream of the wing. The extent of this curvature is shown in Figure 3.11a, marked by a negative spatial derivative at the start of the anti-fairing. Turbulent boundary layer flows over such a convex surface has been shown by various authors [22, 40, 54] to significantly dampen the turbulence production.

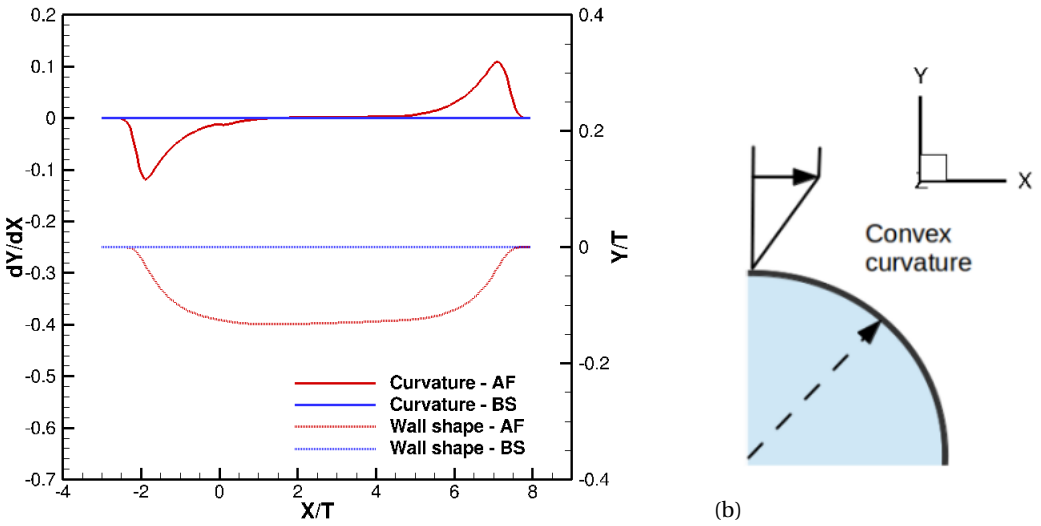

Figure 3.11: (a) Curvature of the anti-fairing denoted by the spatial derivative of the vertical coordinate (b)Example of a 2D turbulent boundary layer over a convex surface

To understand the mechanism of this reduction in turbulent kinetic energy, consider a simple 2D tur-

bulent boundary layer developing over a convex surface as shown in Figure 3.11b. For this 2D boundary layer, from the Reynolds stress transport equations, the production of the three components of the Reynolds stresses are given by [45]

$$P_{11} = \quad -2\langle u'v'\rangle \frac{\partial\langle u\rangle}{\partial y} \qquad \left(\text{Prod. } \langle u'^2\rangle\right) \tag{3.1}$$

$$P_{21} = -\langle u'^2\rangle \frac{\partial\langle v\rangle}{\partial x} - \langle v^2\rangle \frac{\partial\langle u\rangle}{\partial y} \quad \left(\text{Prod. } \langle u'v'\rangle\right) \tag{3.2}$$

$$P_{22} = \quad -2\langle u'v'\rangle \frac{\partial\langle v\rangle}{\partial x} \quad \left(\text{Prod.}\langle v'^2\rangle\right) \tag{3.3}$$

$$P = \frac{1}{2}\left(P_{11}+P_{22}\right) = -\langle u'v'\rangle\left(\frac{\partial\langle v\rangle}{\partial x}+\frac{\partial\langle u\rangle}{\partial y}\right) \quad \left(\text{Prod.TKE} = \frac{1}{2}\left(\langle u'^2\rangle+\langle v'^2\rangle\right)\right) \tag{3.4}$$

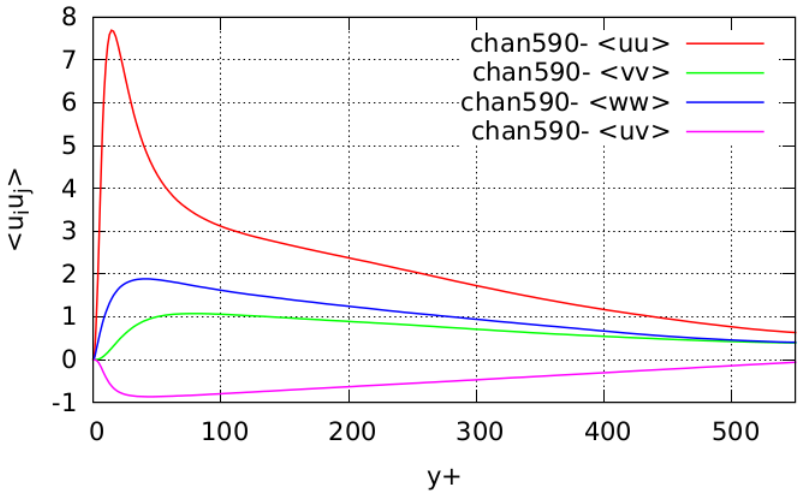

Figure 3.12: DNS results of Reynolds stresses within the boundary layer adapted from Moser *et al* [38]. Pink line indicated the negative values of $< u'v' >$ along the boundary layer.

where <> indicates ensemble averaging, $< u >$ and $< v >$ denote streamwise and vertical mean velocities respectively. The X and Y axes are aligned as shown in Figure 3.11b. Within the boundary layer, the Reynolds shear stress component ($\langle u'v'\rangle$) has been shown to be negative along the entire boundary layer as shown in Figure 3.12 (Pink line). This implies that ($-\langle u'v'\rangle$) is positive for both the flatplate and the convex curvature cases. For the baseline case with no curvature, both the vertical velocity gradient $\frac{\partial\langle v\rangle}{\partial x}$ and the streamwise velocity gradient $\frac{\partial\langle u\rangle}{\partial y}$ are positive at the wall, because of no slip condition. Therefore, all the three terms of the production of turbulent kinetic energy P are positive. However, in the case of convex curvature $\frac{\partial\langle u\rangle}{\partial y}$ is positive whereas, $\frac{\partial\langle v\rangle}{\partial x}$ is negative as the flow turns downwards along the curvature. This implies that the production term P is reduced in magnitude owing to the negative gradient $\frac{\partial\langle v\rangle}{\partial x}$. Therefore, it is clear that convex curvature results in a net reduction of turbulent kinetic energy. In the anti-fairing case, it can be hypothesized that when the flow turns over the convex surface at the start of the anti-fairing, the production of TKE is significantly dampened compared to the baseline case. This reduction in the turbulent kinetic energy directly reflects in the smaller peaks in the kinetic energy of the HSV core. The reduction in the kinetic energy actually happens well before the formation of the HSV. Thus, apart from increasing the approach momentum thickness, the convex curvature of the anti-fairing also reduces the turbulent kinetic energy within the boundary layer. The reduction in turbulence within the HSV core also results in a net viscous drag reduction, which is shown in the drag analysis section.

3.2.3. Flow quantities around the wing

To investigate differences in the mean flow characteristics along the wing for the two cases, contours of mean streamwise velocity are plotted for different streamwise locations for both the cases. Four streamwise locations around the wing have been chosen: $X/T = 0, 1.4, 2.8, 4.2$. The first location corresponds to the wing leading edge and the last one is very close to the trailing edge. The velocity contours are normalized using U_{ref} and are shown in Figure 3.14. The blanked regions in the contours denote the region occupied the wing. It should be noted that the contour levels are the same for the AF and BF cases, they are set to different values for different streamwise locations. This is done to make the difference between the two cases very obvious and apparent. All the subsequent contours will have the same setup. Also, only one side of the wing is shown in the figure, since the vortex appear to be symmetrical along the symmetry plane ($Z/T = 0$).

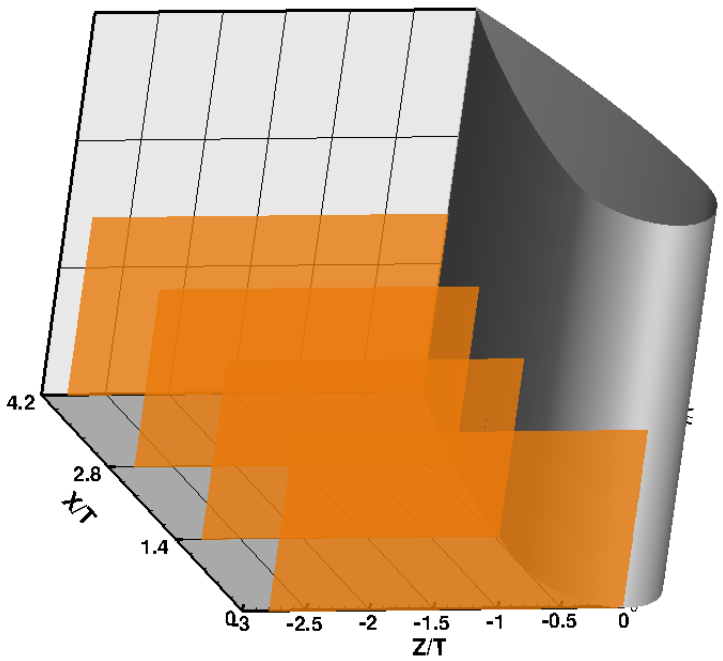

Figure 3.13: Overview of the four streamwise slices considered

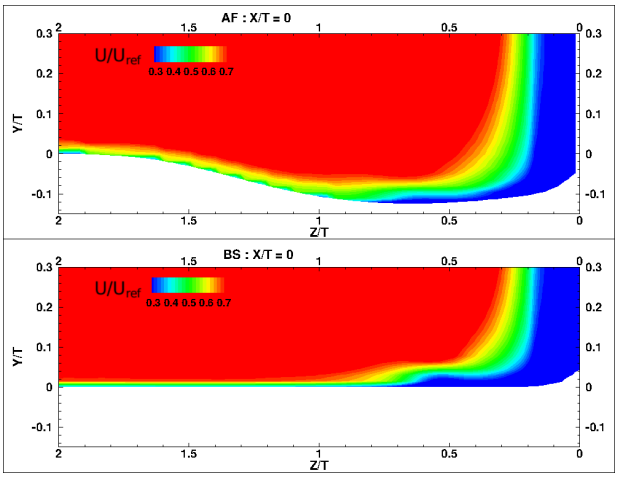

(a) $X/T = 0$

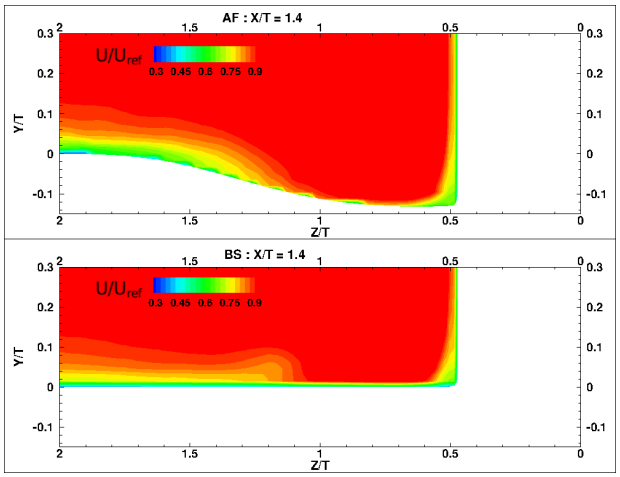

(b) $X/T = 1.4$

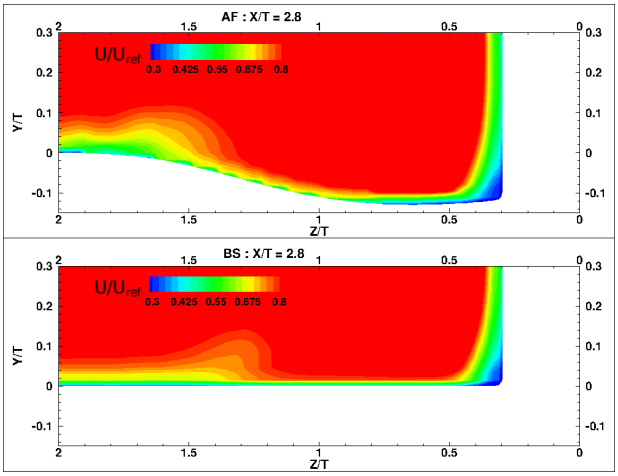

(c) $X/T = 2.8$

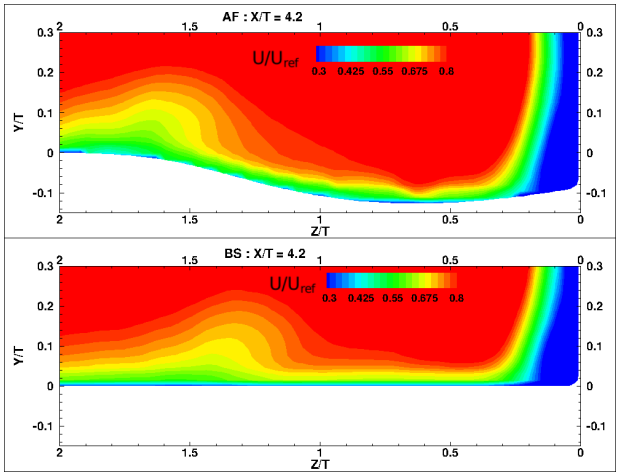

(d) $X/T = 4.2$

Figure 3.14: Normalized mean streamwise velocity comparison around the wing at various streamwise locations

The footprint of HSV is marked by a distinct lump in the velocity contours. This lump is a result of intense flow ejections and recirculation of the mean flow by the vortex such that the flow is lifted up from the boundary layer. On observing the two cases, there are significant differences between them. At all the streamwise locations, the footprint of HSV in the AF case seems to be further away from the wing in the spanwise direction compared to BS. This means that the HSV is pushed further away from the wing in the case of anti-fairing, an observation which was previously made for the anti-fairing by Belligoli*et al* [7] in their work. Moreover, the lump in the BS case seems to be more pronounced in the first two locations compared to the AF case. This indicates that the extent of recirculation caused by the HSV is less for the AF case compared to the BS, which typically means that the magnitude of vorticity in the case of AF is less compared to BS at these two locations. On the contrary, at the last two locations, the lump seems to be more pronounced for the AF case compared to BS, suggesting that the vorticity magnitude is lesser for BS case at these two locations.

To test if the trend observed above holds and also to gain insight into how the HSV travels around the wing, contours of mean streamwise vorticity are compared at the same streamwise locations. The reported streamwise vorticity is non-dimensionalized as $\omega_x T/U_{ref}$ and are shown in Figure 3.15.

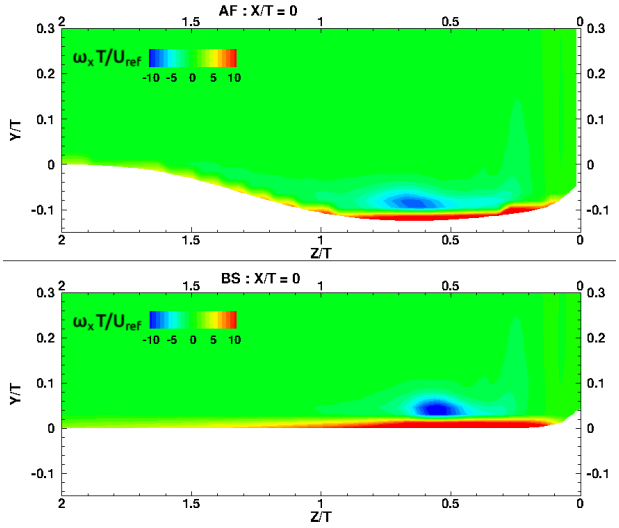

(a) $X/T = 0$

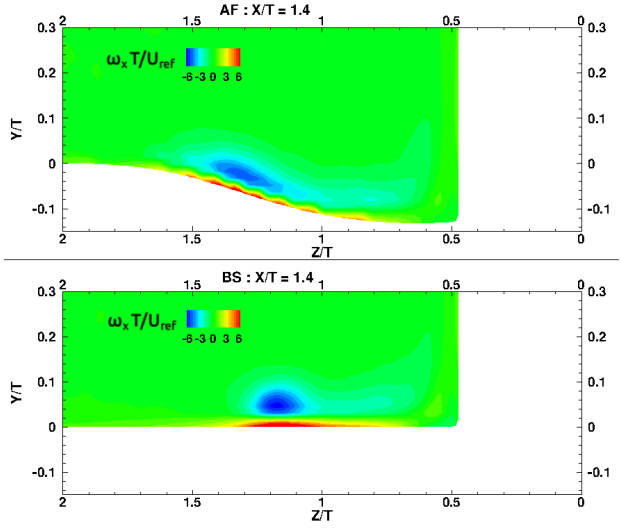

(b) $X/T = 1.4$

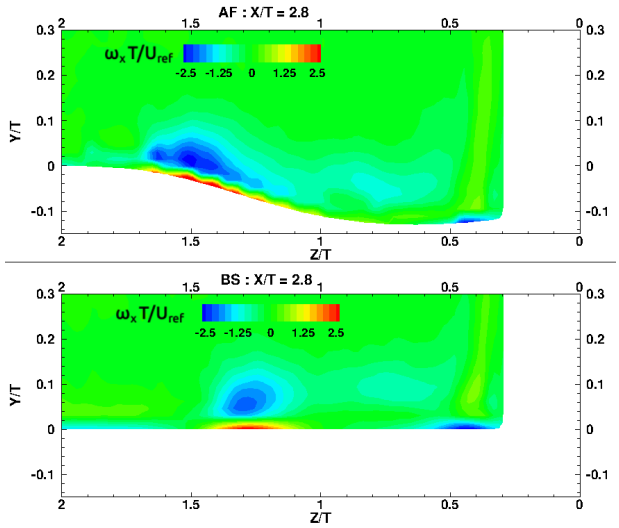

(c) $X/T = 2.8$

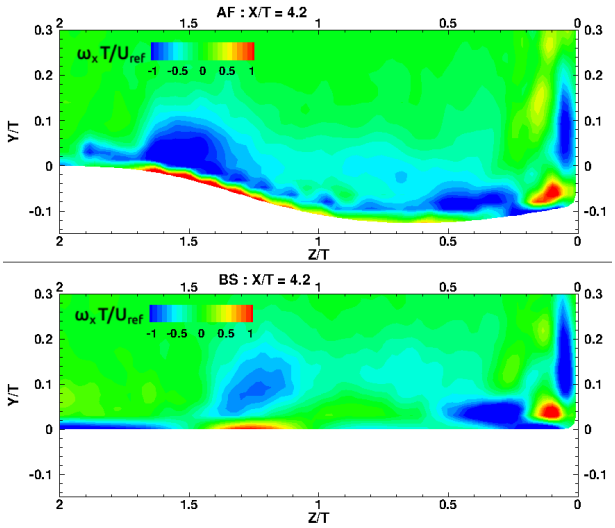

(d) $X/T = 4.2$

Figure 3.15: Normalized mean streamwise vorticity comparison around the wing at various streamwise locations

The HSV which originates in the symmetry plane upstream of the wing is pushed in the spanwise direction and convected downstream by the mean flow. Moving downstream along the wing, the vortex core location continues getting displaced along the spanwise direction. This can be observed in both the cases, where different spanwise positions of the HSV are seen for each streamwise location. On comparing the AF and the BS cases, the HSV core position is displaced further along the span for the anti-fairing case than the baseline, which is analogous to the observation made from the velocity contours. A similar observation was made by Fleming *et al* [18] in their study of Rood wing/flat plate junction. They report that the spanwise separation of the HSV legs increases for higher Momentum Deficit Factor (MDF). As was already observed in Figure 3.9, one of the effects of anti-fairing is to increase the upstream boundary layer momentum thickness (θ), thereby increasing the value of MDF. From the results of Fleming *et al* this directly translates to an increase in the spanwise separation of HSV for the anti-fairing case. The same effect of anti-fairing was also reported by Belligoli *et al* [7] in their work. Looking at the magnitude of the peak vorticity levels of the HSV of the two cases in Figure 3.15 , the trend observed previously seems to be confirmed. At the first two positions, the peak vorticity magnitude of HSV is higher for the baseline case compared to AF, which is analogous to the symmetry plane vorticity seen before. Further downstream, it can be seen that the peak level of AF case is slightly higher. This would mean that the rate at which the peak vorticity magnitude get dissipated due to viscosity is lower for the AF case compared to the baseline. To test this, the magnitude of peak vorticity within the HSV are plotted against different streamwise location. This plot is shown below in Figure 3.16. The different rates of reduction in the peak vorticity magnitude is quite apparent. Owing to the lesser decrease in the peak values for the AF case, after $X/T = 2.1$, the peak values are greater than the baseline case. The reasons for this kind of behaviour are discussed in the subsequent pages.

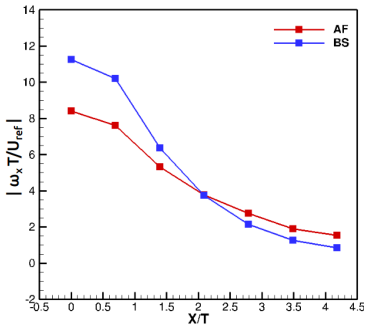

Figure 3.16: Variation in the magnitude of peak streamwise vorticity within the HSV core for different streamwise locations

Another interesting observation from Figure 3.15d is the presence of significant negative vorticity very

close to the wing trailing edge position, which seems to be present for both the cases. This type of vortex structure resembles a vortex obtained from the onset of corner separation. To investigate the presence of corner separation, surface streamlines are drawn on the surface of the wing close to the trailing edge junction. This is shown in Figure 3.17. Interestingly, both the cases show the presence of corner separation. This is quite surprising because, for this particular Rood wing case, no reports of corner separation have been mentioned in the LES results [20, 48], DES results [42] or the experimental results [14, 18, 41] from the literature reviewed by the author. However, Gand *et al* [20] does mention that RANS models erroneously predict a non-existent corner separation, whereas wall resolved LES gives an accurate description of flow in the corner and doesn't show corner separation. They report no particular reason as to why RANS models incorrectly predicts the corner flow. Moreover, similar corner separation was also observed by Koers [28] from her RANS analysis of the wing/anti-fairing junction. This inaccurate prediction in the present work could be due to the application of wall-modeled LES, since previous LES works on wing/body junction flows have all been wall-resolved simulations. However, this needs to be further investigated. Nevertheless, the vortex that emanates from this corner separation is short-lived and gets rapidly diffused after certain streamwise distance, as will be shown in the wake investigation. Also, since this corner vortex is unphysical, no further investigation is done for this. Only the HSV and its characteristics are investigated.

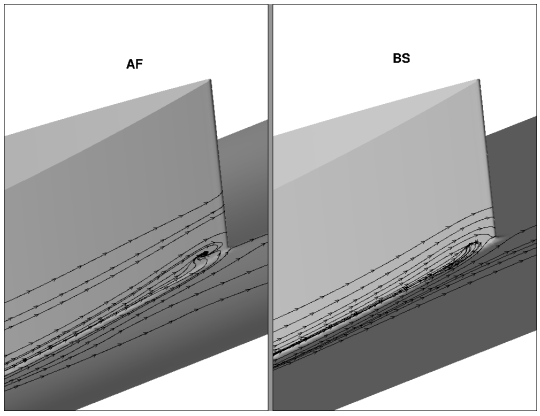

Figure 3.17: Surface streamlines on the wall surface to investigate corner separation

Another important flow feature, which can be used to explain this trend in the vorticity is the turbulence kinetic energy within the HSV. Contours of mean turbulent kinetic energy are observed at the same streamwise locations. The normalized kinetic energy plots are shown in Figure 3.18.

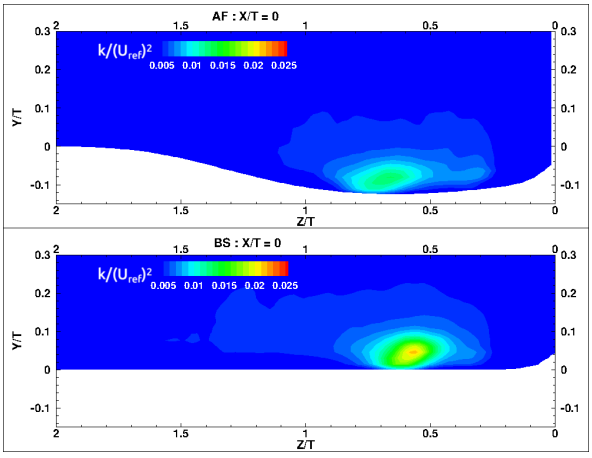

(a) $X/T = 0$

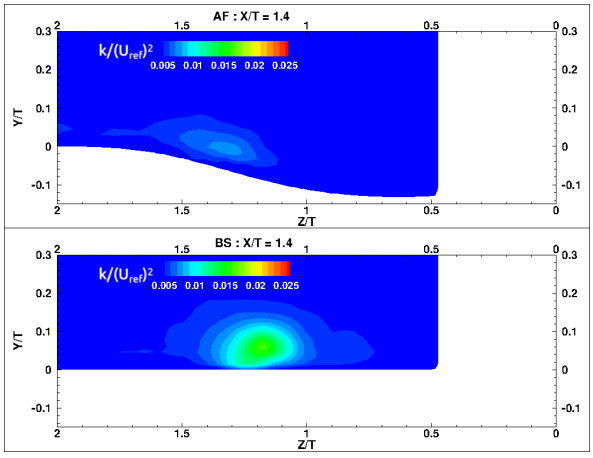

(b) $X/T = 1.4$

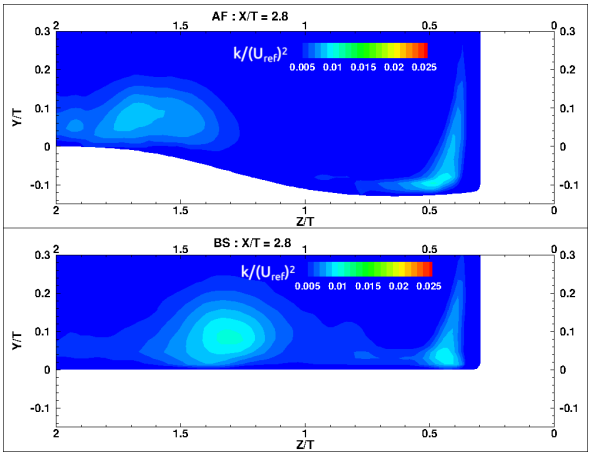

(c) $X/T = 2.8$

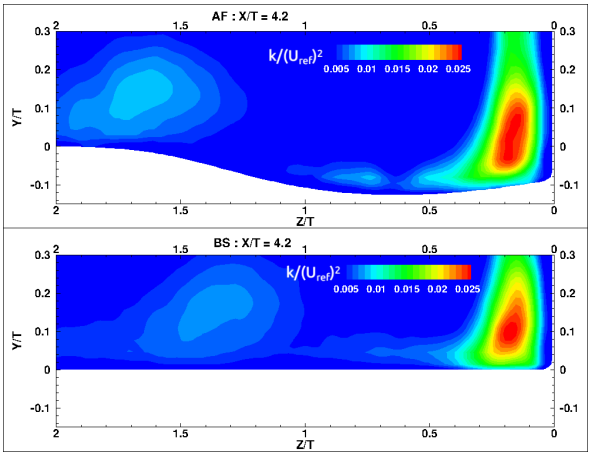

(d) $X/T = 4.2$

Figure 3.18: Normalized mean turbulent kinetic energy comparison along the wing at various streamwise locations

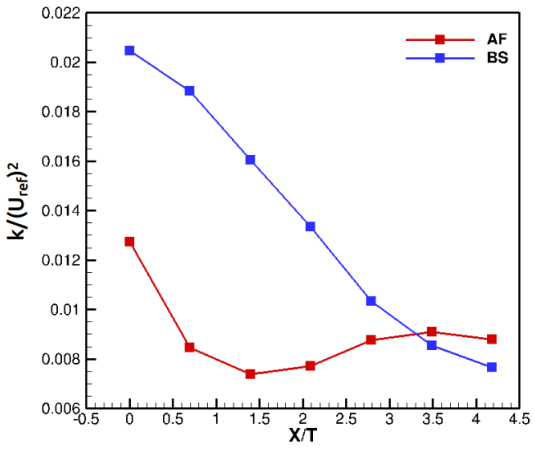

Figure 3.19: Variation in the magnitude of peak turbulent kinetic energy within the HSV core for different streamwise locations

One striking feature of the kinetic energy plot is for the last location, the peak kinetic energy values are significantly higher in the corner vortex compared to the HSV. However, as mentioned above, this corner vortex rapidly diffuses in the wake and thus the primary concern is only with the HSV. On comparing the two cases, at the first two positions, the peak kinetic energy values of the AF case are significantly lesser in the HSV core compared to the BS case. This trend seems to continue from the symmetry plane contours observed previously. However, at the last two locations, the two cases seem to have almost equal peak values of kinetic energy. This would again mean that the rate of change of the peak kinetic energy values along the streamwise locations are not the same for the two cases. Therefore, to check the trend of this variation, peak values of turbulent kinetic energy within the HSV are plotted for various streamwise locations along the wing and is shown below in Figure 3.19. The plot shows some interesting features. For the baseline case, a continuous decrease of the kinetic energy till the trailing edge location can be seen. However, in the AF case, the kinetic energy decreases till $X/T = 1.4$, after which it starts to slightly increase for further downstream locations, before stabilizing in the last two. It seems that there exists a turbulent kinetic energy production mechanism within the HSV as it is convected around the wing.

It would also be helpful to investigate the Reynolds shear stress component ($- < uv >$) within the HSV at these streamwise locations. The other stresses are not shown here because it has been reported by Devenport *et al* [14] that within the HSV, Reynolds shear stress contributes the maximum toward the turbulent kinetic energy production compared to other components of the turbulent stresses. In regards to that, the contours of $- < uv >$ are normalized using U_{ref}^2 and are shown in Figure 3.20 for both the cases. The con-

tours seem to follow the exact trend of the peak streamwise vorticity magnitude observed previously. At the first two locations the peak Reynolds shear stresses are higher for the BS case compared to the AF. At the last two locations, this trend is reversed and the baseline cases have lesser turbulent shear stresses compared to AF. This can also be observed in the plot of normalized peak Reynolds shear stress values for different streamwise locations shown in Figure 3.21. The location where the turbulent shear stress value increases for the AF case exactly coincides with the peak turbulent kinetic energy increase shown in Figure 3.19.

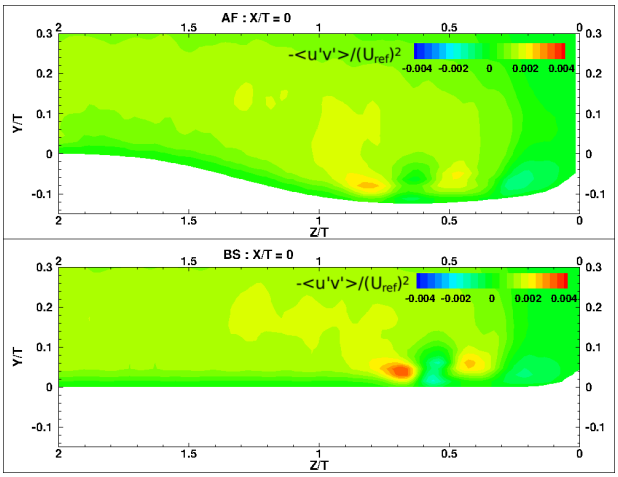

(a) $X/T = 0$

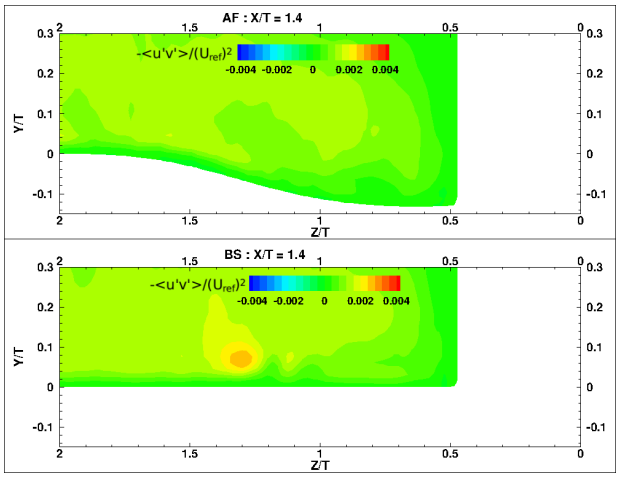

(b) $X/T = 1.4$

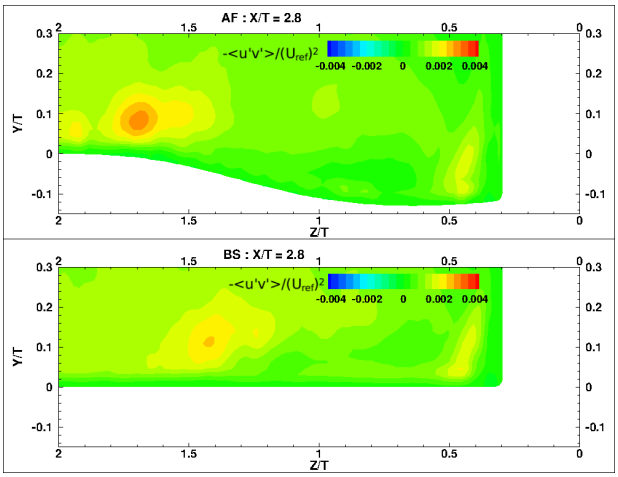

(c) $X/T = 2.8$

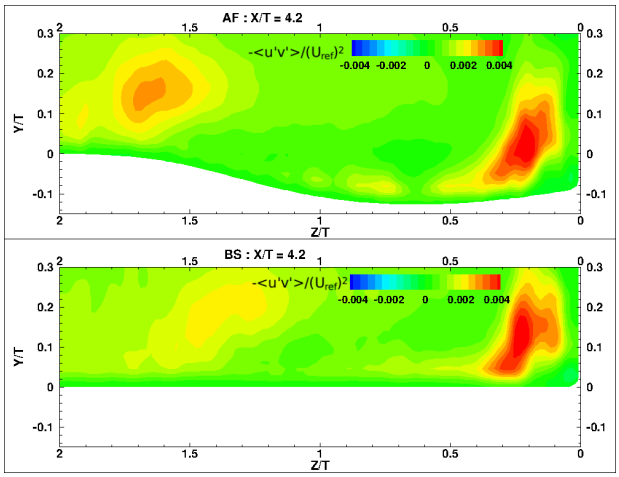

(d) $X/T = 4.2$

Figure 3.20: Normalized mean turbulent shear stress comparison along the wing at various streamwise locations

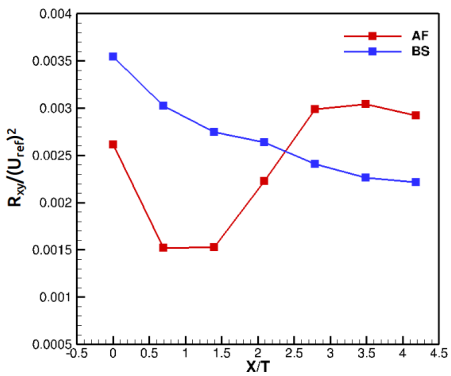

Figure 3.21: Variation in the magnitude of peak turbulent shear stress within the HSV core for different streamwise locations

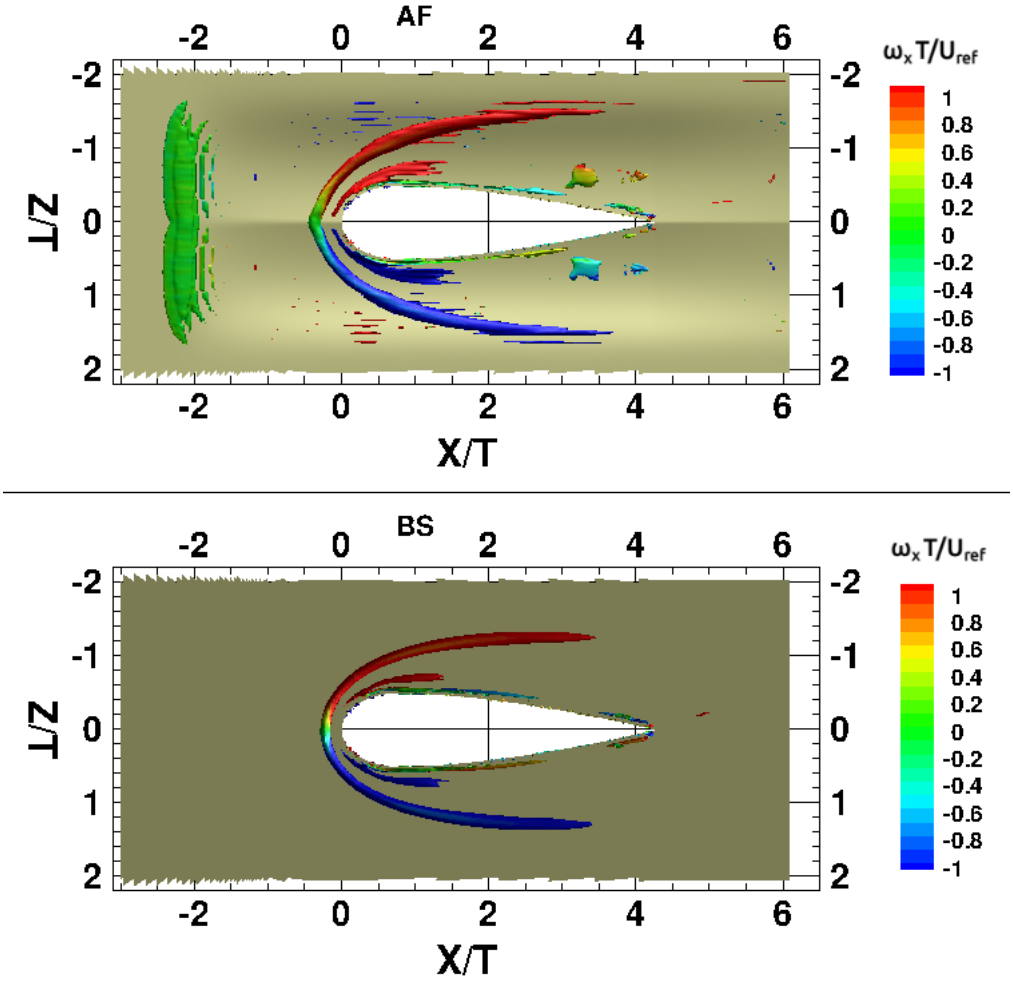

Figure 3.22: Isosurfaces of normalized Q-criterion $Q/(U_{ref}/T)^2 = 0.2$ flooded by the non-dimensional streamwise vorticity

Finally, iso-surfaces of normalized Q-criterion flooded by normalized streamwise vorticity are compared for both the cases to obtain an overview of how the HSV traverses around the wing (Figure 3.22). The previous observations from the streamwise vorticity plots are corroborated by the Q-criterion comparison. The greater spanwise separation of the HSV and also the further upstream location of the HSV in front of the wing can be observed for anti-fairing case. A secondary vortex, which originates in the region between the wing leading edge and the primary HSV is present in both the cases. The strength of the secondary vortex is relatively weaker compared to the primary HSV as can be seen from its smaller size and also by the vanishing of the vortex after about one-third of the wing chord. In the AF case, a small region of vortices can be observed at the start of the anti-fairing dent. This is probably caused due to the sudden change in the curvature of the anti-fairing, as observed in Figure 3.11a. Also, a smaller region of vortices can be observed at the trailing edge of the wing for both the cases. These are caused due to the corner separation observed previously. One important observation from the AF case is the fact that the HSV is pushed into the concave dent of the anti-fairing as it traverses around the wing. From the Q-criterion plot, it is apparent that the HSV originating upstream of the wing faces an increase in concavity of the bottom wall surface (due to the shape of the anti-fairing) until the HSV reaches the edge of the anti-fairing. Once the HSV reaches the anti-fairing edge, the spanwise location of the HSV is almost held constant for further downstream locations. This increase in concavity of the bottom surface can directly be linked to the increased turbulence within the HSV observed from the previous analysis. Similar to the explanation given previously for the convex curvature upstream of the wing which resulted in decreasing the turbulence kinetic energy production, the concave curvature have been known to increase the turbulence production. To show that, a simplified 2D turbulent flow over a concave curvature is taken. An example of a 2D concave surface is shown in Figure 3.11b. The normal Reynolds stress production terms for a 2D turbulent flow are reproduced again [45], which are shown below.

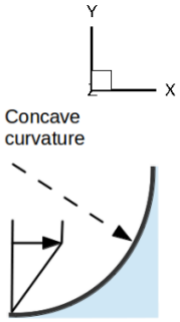

Figure 3.23: Example of flow over a 2D concave curvature

$$P_{11} = \quad -2\langle u'v'\rangle \frac{\partial\langle u\rangle}{\partial y} \qquad \left(\text{Prod. } \langle u'^2\rangle\right) \tag{3.5}$$

$$P_{22} = \quad -2\langle u'v'\rangle \frac{\partial\langle v\rangle}{\partial x} \quad \left(\text{Prod.}\langle v'^2\rangle\right) \tag{3.6}$$

$$P = \frac{1}{2}\left(P_{11}+P_{22}\right) = -\langle u'v'\rangle\left(\frac{\partial\langle v\rangle}{\partial x}+\frac{\partial\langle u\rangle}{\partial y}\right) \quad \left(\text{Prod.TKE} = \frac{1}{2}\left(\langle u'^2\rangle+\langle v'^2\rangle\right)\right) \tag{3.7}$$

As already seen from Figure 3.12, $-<u'v'>$ is positive throughout the boundary layer. For a concave curvature, the flow is turned upward as it moves over the curvature, which implies that $\frac{\partial\langle v\rangle}{\partial x}$ is positive and much greater than the case of a flat plate flow. Moreover, because of the presence of no-slip condition and absence of any flow reversal, $\frac{\partial\langle u\rangle}{\partial y}$ is also positive at the wall. Thus the net production of turbulence kinetic energy is greater in the case of concave boundary layer than the flat plate region. Unlike the convex curvature, the concave curvature supplements the kinetic energy production. This should be the reason for the increase in turbulent kinetic energy observed for the anti-fairing case. Similar behaviour of the concave surfaces have been reported by various authors [22, 23, 54] where the turbulent fluctuations tend to get increased due to the curvature. Specifically they report an increase in Reynolds stresses and consequently, increase in turbulent kinetic energy production. This seems to agree with the results obtained above, where an increase in both the Reynolds shear stress and turbulent kinetic energy is observed for the AF case when compared with BL case. This increased turbulence within the HSV should also be the reason for the increased streamwise vorticity of the HSV, since the HSV structure is dominated by the turbulent nature of the flow within it. However, it should be noted that this increase in the turbulent kinetic energy within the HSV is much smaller compared to the reduction achieved in the symmetry plane. This can be observed in the kinetic energy variation plot along the streamwise locations shown in Figure 3.19. It can be clearly seen that at $X/T = 0$, the two lines are much farther apart compared to the same at $X/T = 4.2$. Therefore, the net effect of the anti-fairing can be summarized as a greater reduction of upstream turbulence and the HSV size in front of the wing, with a slight increase of them imparted by the dented shape observed in the wake of the wing.

3.2.4. Flow quantities in the wake

In this section, contours of the mean streamwise velocity, mean streamwise vorticity and mean turbulent kinetic energy are investigated at two different streamwise locations in the wake: one within the anti-fairing, $X/T = 6$ and other well outside the anti-fairing, $X/T = 12$. The contour plot comparisons of all these quantities at these two streamwise locations are shown in Figures 3.25, 3.26,3.27. Note that the contour levels are different for the two streamwise locations. This is done to clearly isolate the HSV in the wake. Also, each quantity is shown in non-dimensional form as done before.

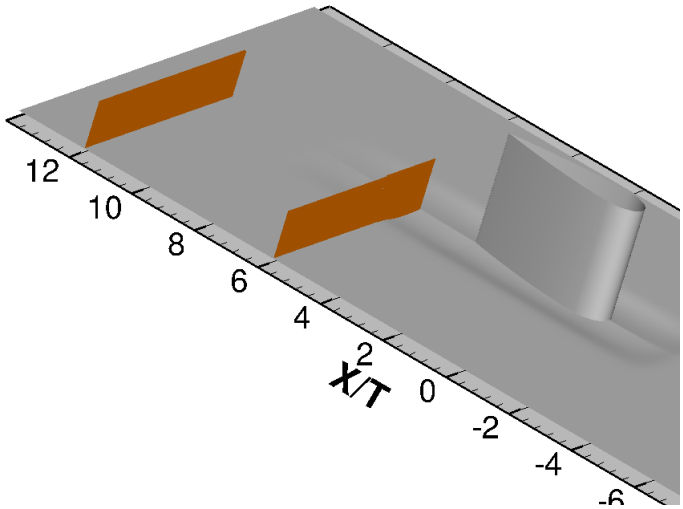

Figure 3.24: Overview of the two streamwise slices considered in the wake of the wing. Note that slice at $X/T = 6$ is within the anti-fairing region and $X/T = 12$ is well outside the anti-fairing region

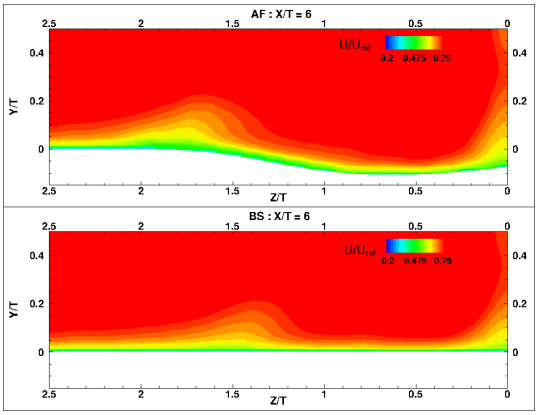

(a) $X/T = 6$

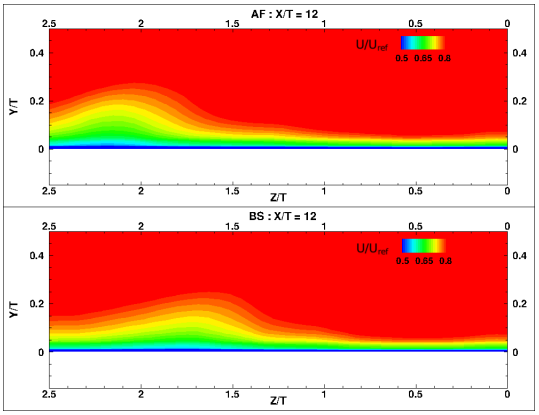

(b) $X/T = 12$

Figure 3.25: Normalized mean streamwise velocity comparison in the wake

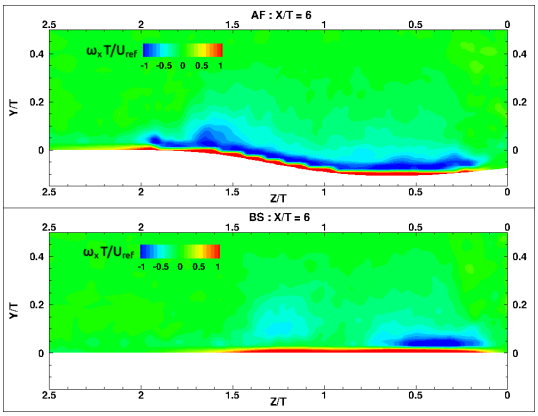

(a) $X/T = 6$

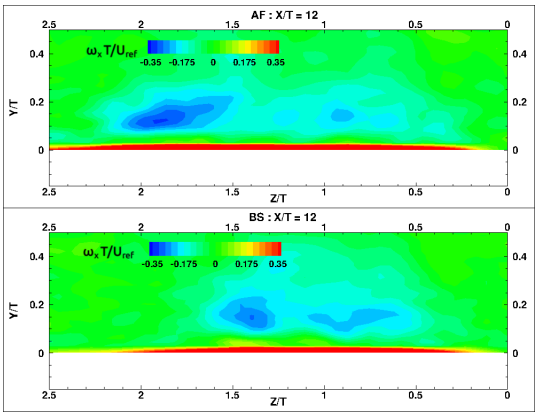

(b) $X/T = 12$

Figure 3.26: Normalized mean streamwise vorticity comparison in the wake

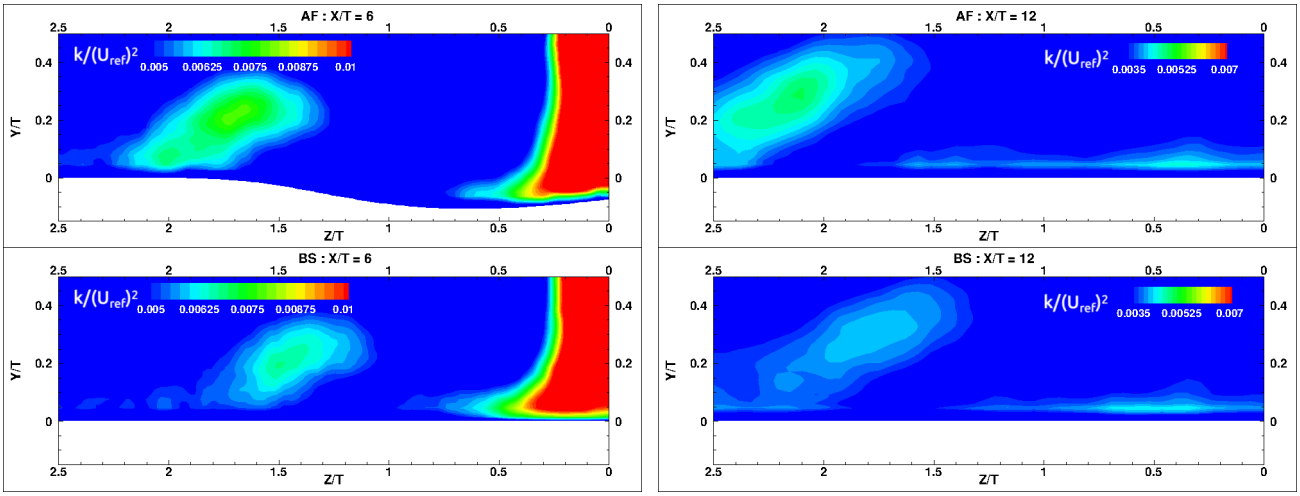

(a) $X/T = 6$ (b) $X/T = 12$

Figure 3.27: Normalized mean turbulent kinetic energy comparison in the wake

From the above plots, it is apparent that the footprint of HSV continues to be present in the wake, although with lesser magnitudes. At $X/T = 6$, the emanated corner vortex is still present. In fact, at this location, the magnitude of vorticity of this vortex is as much as the HSV, which can be observed for both the cases, as shown in Figure 3.26. This is also marked by greater turbulence kinetic energy at the position of the corner vortex, compared to the that of the HSV. Also, for the AF case, the HSV and this corner vortex seem to be connected by a strand of negative vorticity, just as observed at the trailing edge position of the wing ($X/T = 4.2$). However, at $X/T = 12$, the corner vortex is thoroughly diffused and its magnitude of vorticity is much lesser compared to the HSV. It is not clear how the corner vortex is dissipated while the HSV remains with a significant vorticity. With regards to the HSV, the magnitude of its vorticity and its corresponding turbulent kinetic energy is still higher for the AF case. This is expected, since the HSV is constrained to move along the anti-fairing curvature as long as it is within the dent, which would result in greater turbulent kinetic energy and vorticity magnitude as explained above. Once out of the dent, it moves over the flat plate surface similar to the BS case. Therefore, once out of the anti-fairing, vorticity and turbulent kinetic energy of the HSV would be dissipated at the same rate for both the BS and AF case, since no geometrical differences exist between the two cases. A similar behaviour was reported by Smits *et al* [54] in their experimental investigation of flow over a concave curvature. They observed that the recovery of the flow from the increased turbulence caused by the concave bend is very slow once the flow moves to the flat surface. Nevertheless, the magnitudes of vorticity and turbulent kinetic energy has significantly reduced between the two streamwise locations for both the cases, due to the action of viscosity.

3.2.5. Drag analysis

One of the objectives of this thesis is to investigate the drag reduction capabilities of the anti-fairing. In regards to that, integrated drag forces on the wall surfaces are investigated for both the cases. The integrated drag forces include both the wing and the bottom surface (flat plate or anti-fairing). The drag force is calculated using a method called Momentum Deficit Analysis (MDA) [60]. This involves fitting a control volume around the body on which the drag has to be determined, and using the integral momentum conservation equation to obtain the drag. This is employed to obtain the forces instead of integrating the pressure and viscous stresses on the surface because an immersed boundary mesh was used in the current LES study. Immersed boundary meshes do not perfectly resolve the wall surfaces which means that the pressure and viscous stresses have to be interpolated to the surfaces of interest and then integrated over all these surfaces. When this was initially tested, the viscous stresses were greatly under predicted because of interpolation errors. This motivated to employ the MDA method for drag force calculation. The control volume used in the current analysis is shown below.

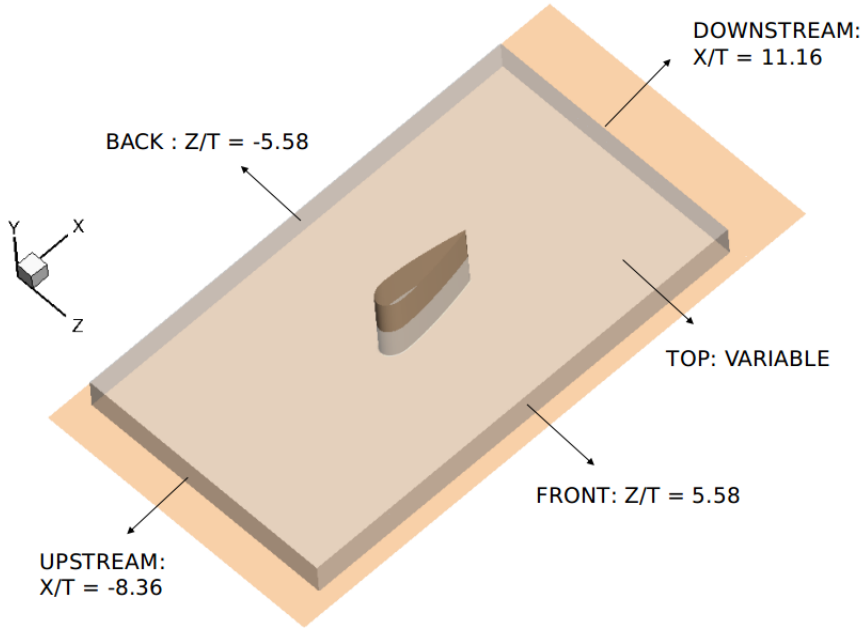

Figure 3.28: Control volume used for drag calculation

The bounding control volume consists of five planes. The upstream plane is situated at a streamwise location of $X/T = -8.36$, which is well upstream of the anti-fairing location. Similarly, the downstream plane is situated well outside the anti-fairing dent, at $X/T = 11.16$. The two spanwise planes are placed at $Z/T = \pm 5.58$ respectively. Finally, the top plane has a variable location which corresponds to the span of the wing considered. The different heights for the top plane considered in the study vary from $Y/T = 0.21$, which corresponds to almost half the inlet boundary layer thickness $Y/T = 0.39$, to $Y/T = 2.86$ which spans the entire length of the wing considered in the simulation. This was done to observe the variations in the drag forces for different lengths of the wing. The bottom surface is not considered, since it corresponds to a no-slip wall, and so net mass flux would be zero through that surface. The rest of the domain is not considered in the calculation as well. For such a control volume Ω, assuming incompressible fluid, the time averaged forces on the body enclosed by it is given by [60],

$$\overline{F}_i = -\rho \iint_s \overline{u}_i \overline{u}_j n_j \mathrm{d}s - \rho \iint_s \overline{u'_i u'_j} n_j \mathrm{d}s - \iint_s \overline{p} n_i \mathrm{d}s + \mu \iint_s \left(\frac{\partial \overline{u}_i}{\partial x_j} + \frac{\partial \overline{u}_j}{\partial x_i} \right) n_j \mathrm{d}s, \tag{3.8}$$

where s denote the surface boundary of the control volume Ω, n_j denote the normal to each of the surface which bound the control volume, $\overline{u}_i$ denote the time averaged velocities, $\overline{p}$ denote the time averaged pressure and $\overline{u'_i u'_j}$ denote the Reynolds stresses. Substituting $\tau_{ij} = \mu \left(\frac{\partial \overline{u}_i}{\partial x_j} \right) - \rho \overline{u'_i u'_j} n_j$ in the above equation and simplifying it for only drag direction (x) (overline symbols have been neglected for convenience),

$$D = -\int_s \left(\rho u (u n_x + v n_y + w n_z) + p n_x - \tau_{xx} n_x - \tau_{xy} n_y - \tau_{xz} n_z \right) \mathrm{d}S \tag{3.9}$$

An issue which would commonly arise with this method of drag calculation is the error in mass conservation within the control volume. As explained by Oudheusden *et al* [60], violation of integral mass conservation over the integration contour surface will be felt as an additional momentum flux and hence affects the loads determination. To remedy this, the integral can be subtracted by a force equivalent to the momentum flux generated by the net mass flux defect multiplied by the freestream velocity. Employing this, the final drag calculation is given as,

$$D = -\int_s \left(\rho (u - U_\infty)(u n_x + v n_y + w n_z) + (p - p_\infty) n_x - \tau_{xx} n_x - \tau_{xy} n_y - \tau_{xz} n_z \right) \mathrm{d}S, \tag{3.10}$$

Thus, evaluating this integral for each of the bounding surfaces and summing them up would give the drag force on the wing/surface system. Each of the flow quantities required to compute the drag are obtained from the time averaged data of LES. The calculated drag forces are then non-dimensionalized to obtain the

drag coefficient (C_d) using the freestream dynamic pressure ($1/2\rho_\infty U_{ref}^2$), reference boundary layer thickness taken well outside the influence of the wing or anti-fairing (here taken as δ_{inlet}) and the maximum thickness of the wing (T), given as

$$C_d = \frac{D}{\frac{1}{2}\rho_\infty U_{ref}^2 \delta_{inlet} T} \tag{3.11}$$

These two parameters were specifically chosen because they represent the geometry of the wing and the approach boundary layer. It has been reported by various authors [5, 18, 53] that the approach boundary layer and the geometry of the wing greatly affect the junction flow characteristics. This was also discussed in Chapter 1. MOreover, these two are also exactly the same for both the BS and AF cases resulting in the same normalizing parameter for both these cases. The drag calculated using Equation 3.10 for different heights of the top plane are plotted for both the cases and are shown as drag coefficients in Figure 3.29.

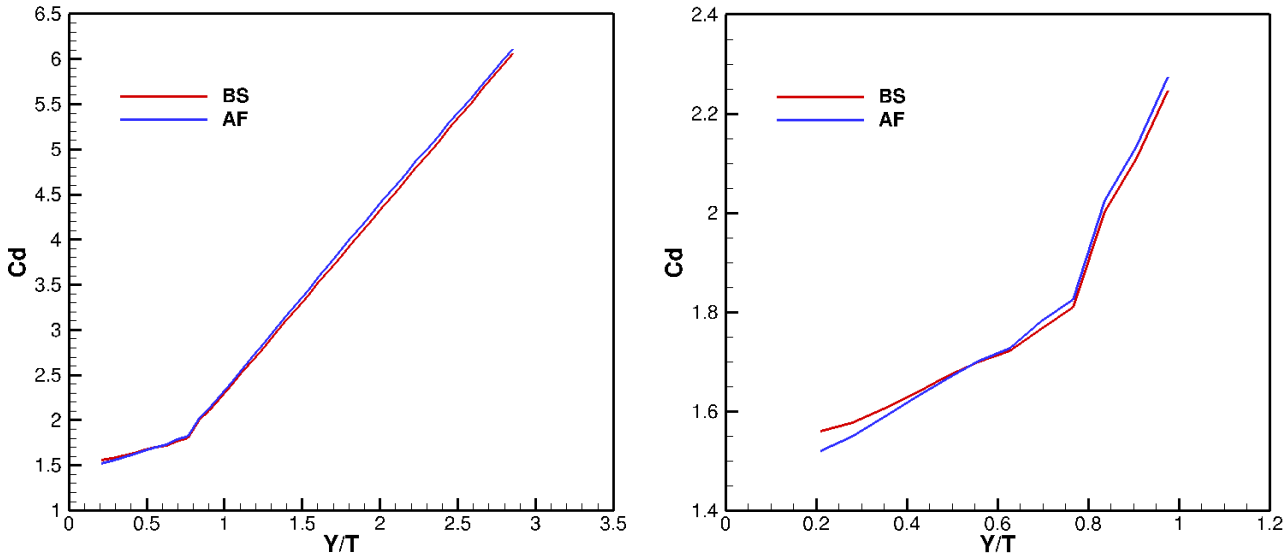

(a) (b)

Figure 3.29: Comparison of the total drag coefficient variation for different heights of the top plane (a) Overview of values for all heights (b) Closer look at the first few heights

The above shown figure denotes a weird behaviour in the variation of the drag coefficient for different lengths of the wing. The variation in Cd seems to have an approximate linear behaviour till about $Y/T = 0.8$ after which a drastic change in the gradient value is observed for both the cases. However, though the gradient is changed, the linear behaviour is maintained throughout afterwards. Figure 3.29b shows a closer look at the first few heights of the top plane. It can be observed that till about $Y/T = 0.5$, the drag is lesser for the AF case, after which the trend is gradually reversed and the drag stays higher for the AF case at all other heights. The abnormal behaviour cannot be attributed to the presence of the anti-fairing since this is seen in the baseline case as well. Since, exact same meshes were used for both the cases it is possible that it could be due to an unphysical numerical artifact that causes flow separation above $Y/T = 0.8$. To investigate the reason for this type of behaviour, surface streamlines on the symmetry plane are visualized just behind the wing . This is shown in Figure 3.30.

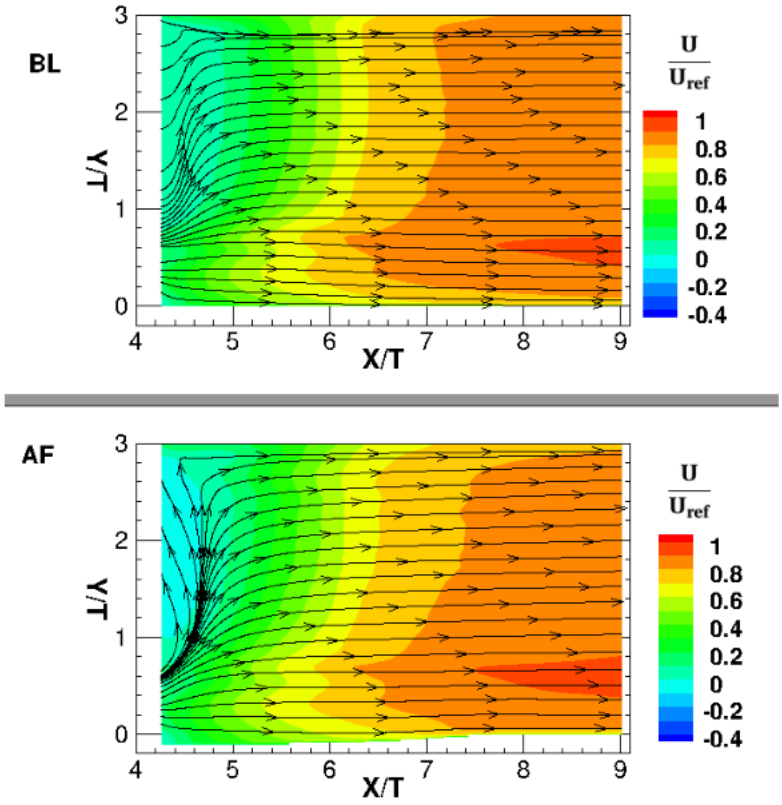

(a)

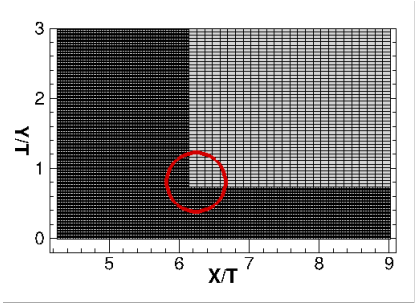

(b)

Figure 3.30: (a) Surface streamlines visualized on the symmetry plane just behind the wing. Contour is flooded by the normalized mean streamwise velocity. The wing trailing edge is at $X/T = 4.25$ (b) Mesh in the symmetry plane with possible problem causing area marked

The above figure confirms the suspicion that an unphysical flow phenomena is the cause of the sudden increase in drag after a certain height. The streamlines depict abnormally high vertical velocities in the wake of the wing, which seem to be at least as much as the streamwise velocity component. For the anti-fairing case, this behaviour is more profound depicted by the streamlines curving much more in the vertical direction. This must be the reason for higher drag prediction for the AF case above a height of about $Y/T = 0.6$. The unphysical vertical velocities would impart a higher momentum deficit in the wake of the wing, which would directly result in an increase of drag. This should be the reason for the sudden change in the gradient of the plot, shown in Figure 3.29. One positive observation however, is the fact that this spurious behaviour doesn't seem to affect the near wall flow phenomena to a greater extent, at least within the inlet boundary layer thickness $Y/T = 0.4$. Since all the flow physics discussed till now are very close to the wall and well within $Y/T = 0.4$, they should hold true to the best of the author's knowledge.

It is not completely clear what caused this type of behaviour in the LES. It is quite surprising that the pressure Poisson equation did not diverge during the simulation for such abnormal behaviour. However, it can be hypothesized that it is a mesh related issue. As shown in Figure 3.30b, there is a coarsening step in the mesh (marked in red), which almost exactly coincides with the height at which this abnormality occurs. As mentioned in the previous chapter, the mesh used in the current LES of both the cases, was generated using Adaptive Mesh Refinement (AMR), which automatically creates a Cartesian mesh based on certain user inputs. It could be that this coarsening step in the mesh is too close to the complex flow phenomena occurring in the junction and the wake of the wing, and the LES equations are too sensitive to the sudden increase in the cell size. Moreover, the complex shape of anti-fairing could have furthered this erroneous behaviour, which might have caused the greater vertical velocities for the AF case.

Since the entire wing could not be considered for the drag coefficient comparison, the presented drag results are computed by assuming a wing length of about $Y/T = 0.3$. At this height, the effect of the abnormality is minimal (Figure 3.30) and also, all the junction flow characteristics are encompassed well within this height.

Thus, the computed drag coefficients for a wing span of $Y/T = 0.3$ are given in Table 3.1.

Table 3.1: Drag coefficient comparison of both the cases

Case name	Cd	% Drag reduction
BS	1.559	-
AF	1.531	1.8

As can be seen, anti-fairing gives about 1.8% drag reduction when compared to the BS case. This is about the same order of magnitude of drag reduction reported by Koers [28] from the wall-resolved RANS analysis of the NACA 0015/anti-fairing combination in her Master thesis, which was about 3%. Apart from the total drag coefficient values reported above, it would also be helpful to analyze the effect of anti-fairing only on the drag due to the presence of junction. For this analysis, a parameter called "junction drag coefficient (Cd_{junc})" is defined. This is obtained by subtracting the drag coefficients corresponding to an isolated wing without any junction effects (which has a span of $Y/T = 0.3$) and also the drag coefficient corresponding to an isolated flat plate (which has the same area as the bottom wall) from the Cd obtained for both BS and AF cases.

$$Cd_{junc}^{AF/BS}(Y/T = 0.3) = Cd_{total}^{AF/BS}(Y/T = 0.3) - Cd_{\text{isolated flat plate}} - Cd_{\text{isolated wing}}(Y/T = 0.3)$$

This parameter is used to isolate the drag increase only due to the junction and compare the drag characteristics of BS and AF. This definition is similar to the definition of the interference drag, but there are some important differences :

- In the case of AF, the bottom wall actually consists of the anti-fairing. However, the anti-fairing area is substituted by a flat plate region just as the bottom wall of BS case and the drag due to the flat plate is calculated only on this completely flat surface
- The increase in wing span due to the depth of the anti-fairing is also not considered when calculating the drag of the isolated wing

Thus the drag due to the isolated flat plate and isolated wing are the same for both the BS and AF cases. It is defined this way to include the effects of the increased wetted area due to the anti-fairing in the calculation of junction drag of the AF case. Therefore, on comparing the junction drags of the two cases, it can be seen whether the anti-fairing produces a net drag reduction even with the included wetted area. The drag values of the isolated wing and flat plate are obtained by running coarse grid RANS simulations (5 million for the isolated wing and 1 million for the isolated flat plate) of each case separately. Thus, the computed junction drag coefficients for both the cases are shown below in Table 3.2.

Table 3.2: Junction drag coefficient comparison of both the cases

Case name	Cd_{junc}	% Junction drag reduction
BS	0.41	-
AF	0.382	6.83

As can be seen from the above table, the junction drag reduces by about 6.83% due to the presence of anti-fairing. This junction drag reduction gives a slightly clearer picture of the effect of anti-fairing compared to the total drag reduction. Since the isolated effects of the wing and the flat plate are removed, the obtained drag reduction suggests that the anti-fairing directly modifies the drag that is caused only due to the presence of the junction.

However, it is still not clear if there is any other mechanism apart from the prescribed propulsive pressure effect [7] that aids in the drag reduction. In the previous pages, a significant reduction in the turbulence upstream of the wing was observed in the AF case. It should be seen if this amounts to drag reduction as well. To test that, the respective pressure drags of the two cases obtained by considering the wing cut at $Y/T = 0.3$ are subtracted from the total drags shown in Table 3.1 to obtain only the viscous drag contribution of both the cases. In doing so, the propulsive pressure effect of the anti-fairing is neglected, thus it can be seen if drag is still lesser for the anti-fairing case. The obtained viscous drag of the two cases are shown below in Table 3.3.

Table 3.3: Viscous drag coefficient comparison of both the cases

Case name	Cd (total)	Cd (pressure)	Cd (viscous)	% Viscous drag reduction
BS	1.559	0.03	1.529	-
AF	1.531	0.0043	1.527	0.131

The viscous drag does seem to be decreased, suggesting that the propulsive pressure effect is aided by another drag reduction mechanism as well. It should be noted that despite having larger wetted area in the AF case, the skin friction drag is smaller. However, most of the drag reduction is still due to the propulsive pressure effect. This decrease in skin friction drag in the case of anti-fairing could be due to two effects:

- The increase in the upstream boundary layer momentum thickness because of the shape of the anti-fairing
- The reduction in the HSV size and the turbulence within the core upstream of the wing leading edge

Drag reduction for the case of junction flows due to the second effect have been reported by a number of authors [15, 24, 26, 29], which have been discussed in Chapter 1. This suggests that the second effect could be a major contributor in the viscous drag reduction. However, the effect due to the increasing momentum thickness cannot be neglected as well. Also, despite the fact that the vorticity magnitude and kinetic energy within the HSV are slightly higher as the HSV moves around the wing, it seems to be overcompensated by the greater reduction in the symmetry plane, resulting in a net reduction in viscous drag. Therefore, this acts as conclusive proof that the drag reduction mechanism due to the pressure effect (proposed by Belligoli *et al* [7]) is also aided by two secondary effects of the anti-fairing which result in a net skin friction drag reduction.

4

Results and discussion: RANS

In this chapter, the investigation regarding the performance and effectiveness of the anti-fairing is extended further by analysing the effect of different inlet boundary layer thicknesses and anti-fairing depths. Inlet boundary layer thickness is chosen as a parameter since it was reported [18] to be a major attribute in defining the junction flow HSV. Thus it was believed to have an impact on the performance of the anti-fairing as well. The reason for choosing the depth of the anti-fairing as another parameter is due to the fact that the primary drag reduction mechanism of the anti-fairing is the propulsive pressure effect caused due its upstream dent. This motivated to study the drag reduction capabilities of the anti-fairing for different depths of this dent. For this study, steady RANS simulations are employed, since a number of cases need to be studied and performing LES for every case is time-consuming and not feasible. With regards to that, the RANS setup is first validated for the exact domain and geometrical configurations used in the LES. Both the baseline and the anti-fairing cases are compared with the present LES results and literature. Following that, simulations are run for a NACA 0015 wing, using which the performance of anti-fairing is gauged for varying inlet boundary layer thicknesses and anti-fairing depths. The details regarding the setup of all these cases are discussed in Chapter 2.

4.1. Comparison between LES and RANS : Rood wing case

For comparing and validating the RANS flow case, the main flow features used are the upstream boundary layer profiles at specific streamwise locations, the mean spanwise vorticity, and the mean turbulent kinetic energy in the symmetry plane. These parameters are specifically chosen since these typically demonstrate the characteristics of the junction flows. From the boundary layer profiles, flow separation and subsequent flow reversal due to the adverse pressure gradient of the wing can be observed. The spanwise vorticity and mean turbulent kinetic energy profiles represent the HSV structure and its associated turbulence within the core. Thus comparing these parameters would give an idea of how effective RANS simulations are in capturing the important junction flow features. Each of these comparisons and their associated discussions are shown in the subsequent pages.

4.1.1. Comparison of upstream boundary layers

In this section, the upstream boundary layer profiles are compared with the LES results in the symmetry plane at specific streamwise locations. Both BS and AF cases are shown for comparison. Looking at the BS case, it is apparent that the LES profiles give superior prediction of the boundary layer at all the locations. The velocities are slightly over predicted by the RANS simulation, up to a height of about $Y/T = 0.5$, above which it merges back to the experimental and LES results. Moving closer to the wing, it can be seen that the profiles get further away from U/U_{ref}, denoting the slowing of the fluid as it approaches the wing. The last three locations have significant backflow indicating the flow reversal occuring due to the adverse pressure gradient imparted by the wing. At $X/T = -0.3$, a slight over estimation of the backflow is observed for the RANS results. Downstream of this position, the prediction is reasonably accurate. This exact behaviour was also reported by Ryu *et al* in their comparison of fine grid LES and coarse grid RANS. Interestingly, at the location closest to the wing, the RANS results are quite close to the experimental results and the LES. Thus overall, the performance of RANS seem to be reasonable when compared to the LES results. The discrepancies are to be expected, since the linear eddy viscosity models do not resolve the anisotropy in the turbulent stresses

[4, 45, 48], thus upstream boundary layers close to the wing leading edge, which is dominated by the highly turbulent and unsteady phenomenon such as formation of HSV cannot be accurately captured by a steady, linear eddy viscosity RANS turbulence model. Moreover, the inlet boundary condition for RANS is given as a fixed boundary layer generated from Spalding's law (refer Chapter 2), whereas LES had a more realistic inlet boundary layer from the rescaling/recycling boundary condition. This could also have contributed to the discrepancies in the RANS boundary layer profiles.

Looking at the AF case, the RANS behaviour is almost the same as observed for the baseline. It should be noted that the anti-fairing shape is not flat, and the wall position keeps changing for different streamwise locations, which are indicated by the shift of the boundary layer profiles in the negative y direction. Unfortunately, boundary layer profiles from the literature could not be found for cases of anti-fairing to have a comparison with them. As observed in the baseline case, the velocity values are consistently over estimated by RANS till a certain height, before falling on top of the LES results. Particularly, at $X/T = -0.1034$, the values are higher over the entire boundary layer. Apart from these, the results aren't too drastically different from the LES results.

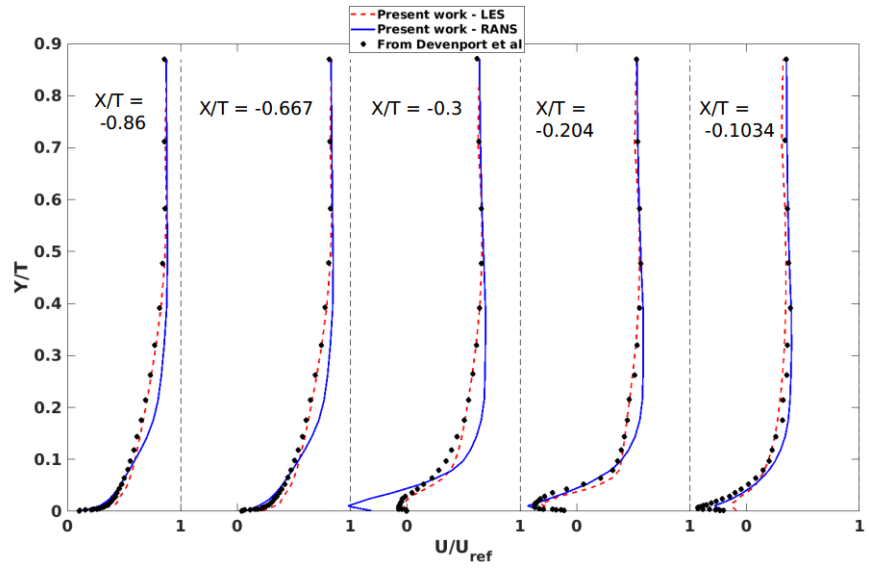

(a)

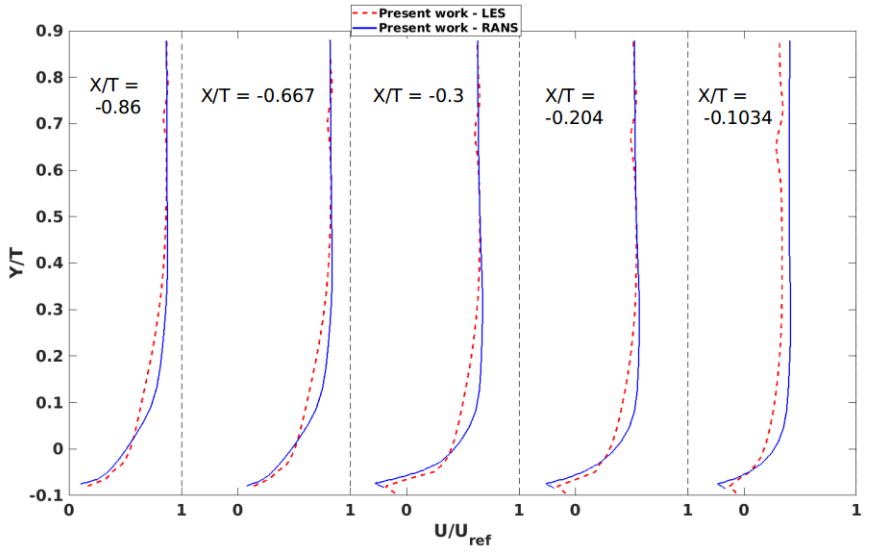

(b)

Figure 4.1: Comparison of boundary layer profiles obtained from RANS and LES (a) Baseline (b) Anti-fairing

4.1.2. Comparison of spanwise vorticity in the symmetry plane

Figure 4.2 shows the comparison of normalized spanwise vorticity in the symmetry plane obtained from LES and RANS. Both the BS and AF cases are shown. The results reported by Ryu *et al* are also attached for reference. Looking at the BS case, the magnitude of vorticity in the HSV is predicted lesser compared to the LES results. Also, the centre of the HSV core is also slightly upstream to the location predicted by RANS. However, comparing the RANS results of Ryu *et al*, the present results seem to be better. The HSV elliptical shape is predicted to some accuracy in the present work compared to a smooth blob of negative vorticity shown in the RANS results of Ryu *et al*. Moreover, the region of positive vorticity caused due to the flow reversal and no-slip condition of the wall is over estimated, with the reversed flow region starting much upstream compared to the LES results. This was observed in the boundary layer plots as well (Figure 4.1a) at $X/T = -0.3$, where a larger negative velocity is predicted. Also, at the wing leading edge position $X/T = 0$, a thin line of positive vorticity could be observed for RANS results, which is not present in the LES results. This is due to the boundary layer developing over the wing. The fact that it is not present in LES results could be attributed to the use of immersed boundary mesh, where the wall regions are not perfectly captured. In the case of RANS, a body-fitted mesh is used, where the mesh cells are fitted directly on the surface of the wall regions, which could have resulted in the prediction of the positive vorticity on the wing. In the anti-fairing case too, the performance of RANS is very similar to that of the BS case. The predicted negative vorticity magnitude of HSV is lesser and the positive magnitude below the HSV and on the wing leading edge are higher compared to LES. However, unlike the BS case, where the lift up of the boundary layer was predicted more upstream, for AF case, the lift up of the boundary layer to form the HSV is predicted slightly downstream compared to the LES.

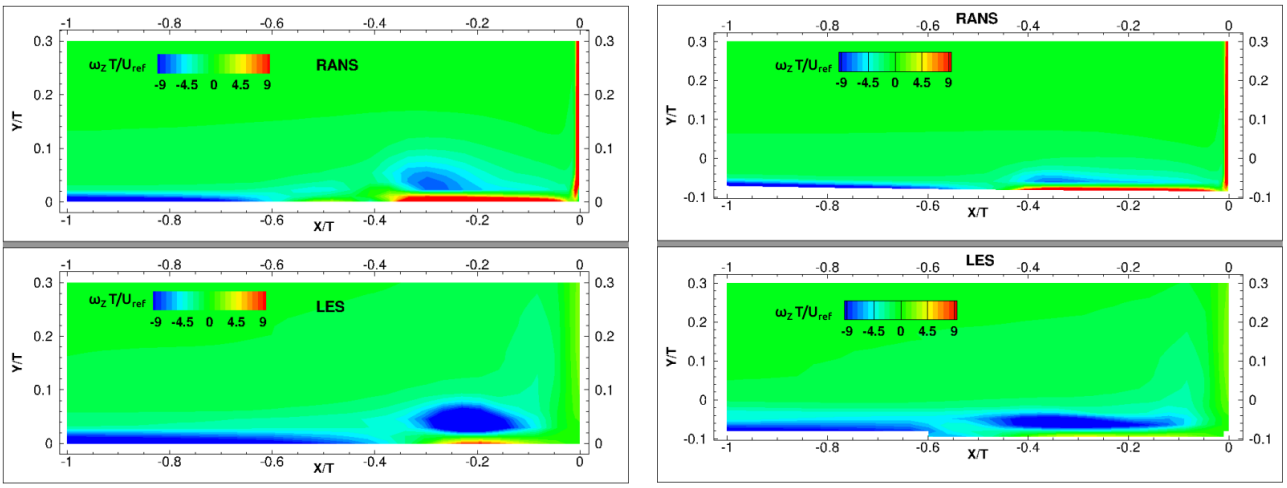

(a) BS

(b) AF

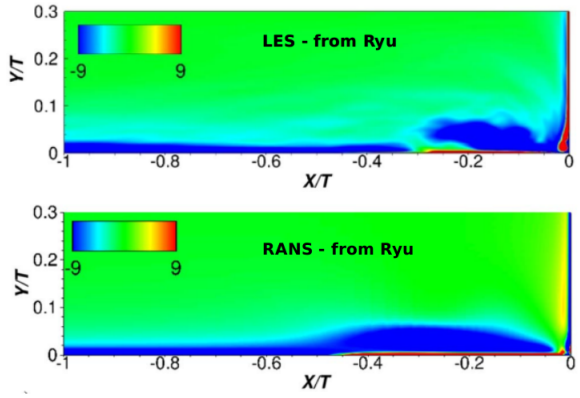

(c)

Figure 4.2: Comparison of normalized spanwise vorticity in the symmetry plane obtained from RANS and LES. (a) Present LES and RANS - Baseline (b) Present LES and RANS - Anti-fairing (c) LES and RANS results obtained for the baseline case from Ryu *et al* [48]

4.1.3. Comparison of turbulent kinetic energy in the symmetry plane

The turbulence kinetic energy plots reiterates the observations from the spanwise vorticity plots. Since the HSV location in the BS case is predicted slightly more upstream in RANS, the position of peak kinetic energy magnitude too is predicted further upstream compared to LES. Interestingly, for the BS case, the peak values of RANS are comparable to the values of LES of the present work, though much smaller compared to the LES results of Ryu *et al.* As discussed in the previous chapter, the lesser magnitude predicted in LES could be due to the non-availability of enough cells close to the wall. The peak values of RANS from Ryu *et al* are comparable to the values obtained in the present RANS study of the baseline configuration. Analogous to the observations from the spanwise vorticity plots, for the AF case, the region of high kinetic energy is more downstream, compared to the LES.

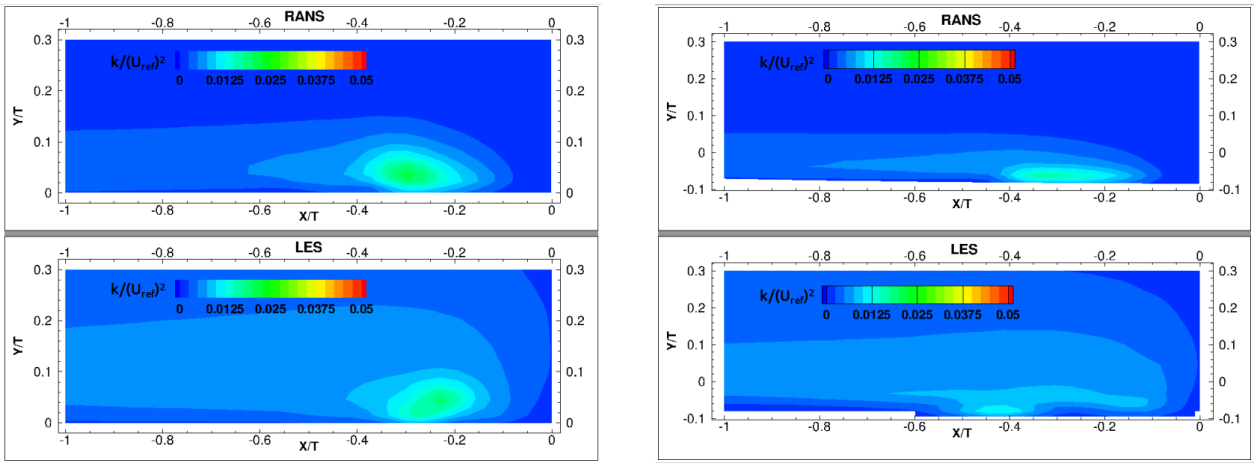

(a) BS

(b) AF

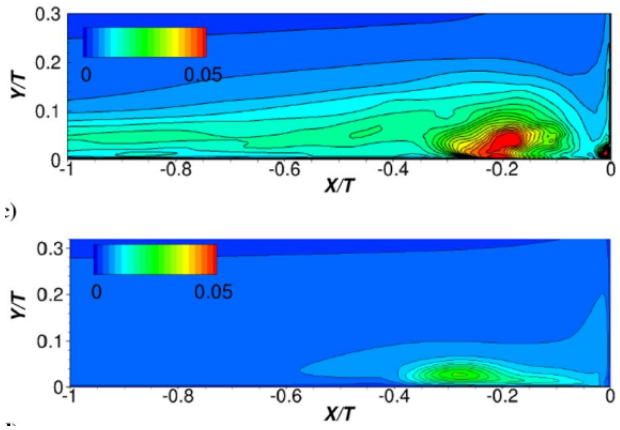

(c)

Figure 4.3: Comparison of normalized turbulent kinetic energy in the symmetry plane obtained from RANS and LES. (a) Present LES and RANS - Baseline (b) Present LES and RANS - Anti-fairing (c) LES and RANS results obtained for the baseline case from Ryu *et al* [48]

From the three comparisons, it is clear that RANS results under performs in comparison to LES results. However, given its extremely low computational cost relative to the LES, it does a reasonably good job at predicting the presence of the HSV, though the location and magnitude of vorticity is slightly incorrect. Also, the thinning of the HSV for the AF case is nicely captured by the RANS as well. Moreover, the near wall boundary layer profiles at the last two locations is not much different from the LES or experimental results. Thus, in conclusion, RANS results cannot be relied upon for any analysis related to the characteristics of the HSV core, whereas it is trustworthy for simple analysis such as integrated loads comparison. Furthermore, since only comparison studies are going to be performed, RANS results are more than enough for these analysis as they do capture the difference in the HSV structure between the baseline and anti-fairing cases.

4.2. Performance of anti-fairing for different depths and approach boundary layer thicknesses

In this section, the drag reduction capabilities of anti-fairing are gauged for different anti-fairing depths and approach boundary layer thicknesses. As mentioned in Chapter 2, a NACA 0015 wing is used for the analysis, with a chord length of $c = 0.2m$ and a maximum thickness of $T = 0.03m$. From here on, all the length scales are non-dimensionalized using $T = 0.03m$, instead of the maximum thickness of Rood wing used till now. The approach boundary layer thickness is varied by having different inlet boundary layer thicknesses at the domain inlet. These different inlet boundary layers would develop over the flat plate portion of the domain and would result in having different boundary layer thicknesses just upstream of the anti-fairing, thus obtaining different approach boundary layers. The different anti-fairing depths and the inlet boundary layer thickness used for the analysis are shown in their non-dimensional form in the Tables 4.1,4.2.

Table 4.1: Different anti-fairing depths considered

Case name	**Depth/T**
AF_0	0
AF_0.5	0.104
AF_0.75	0.156
AF_1	0.208
AF_1.25	0.26
AF_1.5	0.312

Table 4.2: Different inlet boundary layer thicknesses considered

Case name	δ_{inlet}**/T**
BL_0.5	0.552
BL_0.75	0.828
BL_1	1.103
BL_1.25	1.379
BL_1.5	1.655

Each of the case names have a number, which signifies the scale of the relevant parameter with respect to the _1 case, which is the baseline. For example AF_0.5 has its anti-fairing depth which is 0.5 times of that of AF_1 case. Similarly, BL_1.25 case has its δ_{inlet} value 1.25 times that of the BL_1 case. Thus, each of these cases are simulated for every other case, which resulted in a comprehensive set of 30 RANS simulations. Note that all the drag forces reported further are normalized by the freestream dynamic pressure $q = 0.5\rho_\infty U_\infty^2$ and a reference area calculated as the product of the maximum thickness of the wing T and a reference span of the wing(here taken as $h = 0.21m$) to obtain the drag coefficient C_d. It should also be noted that the normalizing parameter is the same for all the cases investigated. Moreover, the reference area used in the RANS analysis is different than the one used in LES (refer Equation 3.11) where inlet boundary layer thickness was used in the place of the reference wing span. This cannot be used in the current RANS analysis, since this inlet boundary layer thickness is itself a varying parameter and so would result in different normalizing parameters for different cases. Thus to use a common parameter for all the cases investigated, the reference area is calculated as such.

$$C_d = \frac{F_{drag}}{qTh}, \tag{4.1}$$

4.2.1. Effect of different anti-fairing depths

Firstly, the effects of varying the anti-fairing depths on the total drag of the anti-fairing/wing system are studied with a fixed inlet boundary layer thickness. The fixed δ_{inlet} corresponds to BL_1 case, with $\delta_{inlet}/T = 0.208$. The pressure drag, viscous drag and the total drag are computed for each of these cases and the variation in the coefficients are reported separately for the wing and the anti-fairing (which includes the flat part of the wall as well), and also for the combined system. These are shown in Figure 4.4. Note that the vertical

axes values are different for each plot. This was maintained to clearly observe the trend in each component of drag.

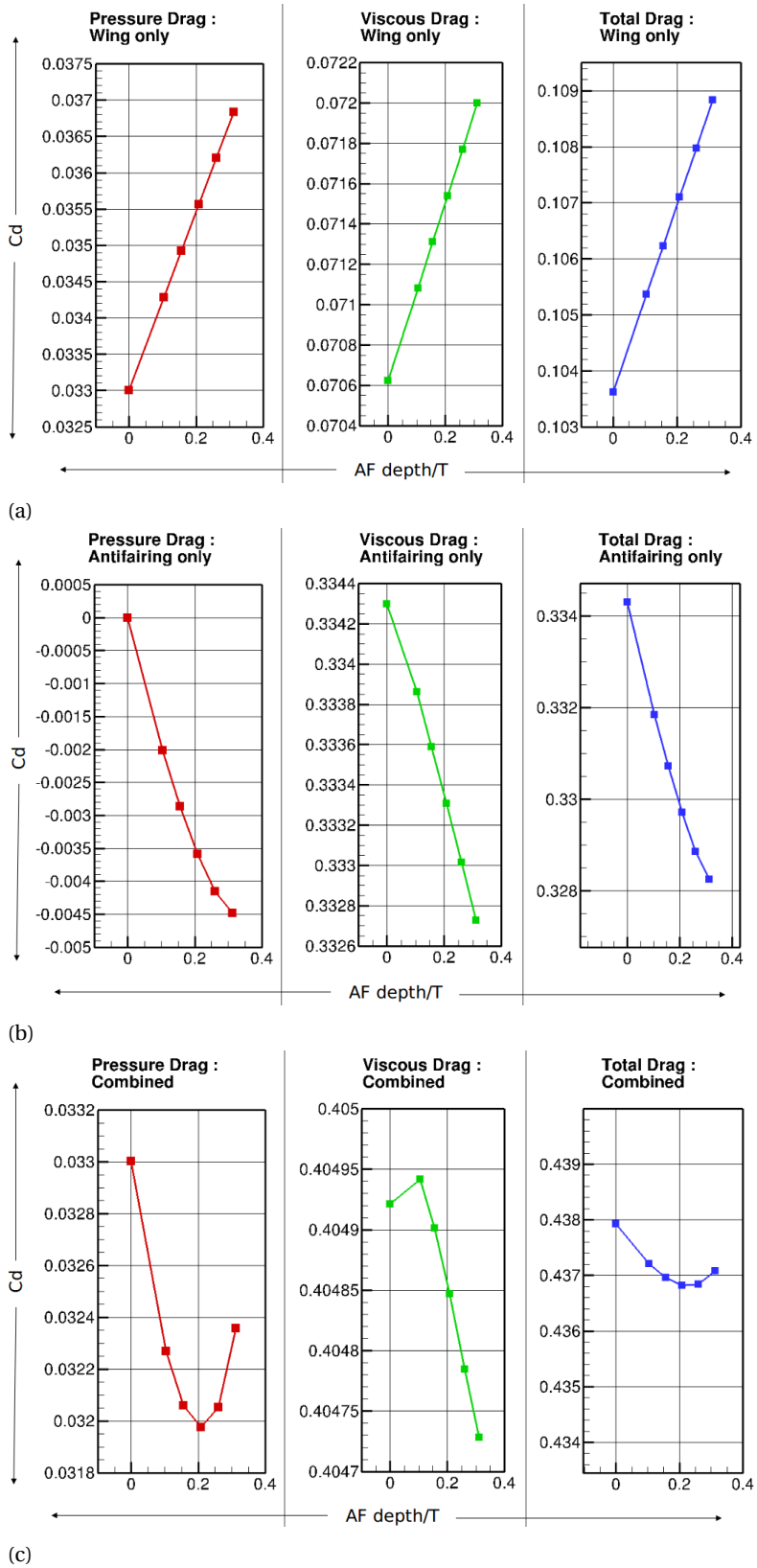

Figure 4.4: Variation of different components of drag for different anti-fairing depths

Figure 4.4a shows the effect of anti-fairing on the wing alone. As can be observed, as the anti-fairing depth increases, both the pressure and viscous drag increases linearly, resulting in a linear increase in the total drag as well. Linear increase in both the viscous drag and pressure drag suggests that it is primarily caused due to the increase in wetted area of the wing within the anti-fairing for higher depths. As the anti-fairing depth is increased, the top plane is kept at a constant y position, which would mean that the span of the wing is increased. Thus a boundary layer would develop over this extra part of the wing which contributes to the excess viscous drag. Similarly the pressure integrated over this excess area would result in higher pressure drag. The fact that the increase is linear further corroborates this explanation since, the wetted area is a linear function of the anti-fairing depth. A linear increase in both the viscous and the pressure drag ultimately results in a linear increase of the total drag over the wing.

As for the anti-fairing (Figure 4.4b), we see an exact opposite trend for both the drag components. Both the drag components continuously decrease for increase in the anti-fairing depth, although the decrease is not linear. It should also be noted that the pressure drag values are significantly lesser compared to the viscous drag. This is because, most part of the bottom wall is a flat plate region, with the anti-fairing shape occupying only a small area around the wing. Thus the pressure drag contribution is closer to zero for the flat plate part (as can be observed from the 0 value obtained for the complete flatplate case), and only the anti-fairing shape contributing to it. However, a boundary layer develops over the entire bottom wall, thus the viscous stresses act over a much bigger area, thereby having greater contribution to the total drag. The trend observed in the pressure drag plot can be explained from the higher upstream static pressures that is obtained for greater anti-fairing depths. As discussed previously, the flow slows down within the anti-fairing which creates a higher pressure in front of the wing compared to the flatplate case. As the anti-fairing depth is increased, the fluid flows over a greater diverging area, resulting in a further slowing down of the fluid to satisfy mass conservation. This would create a further rise in static pressure in front of the wing for increase in anti-fairing depths. As shown in Figure 1.10a, the anti-fairing shape is such that this high pressure would result in a force which has a component in the opposite direction of the drag, thus creating a propulsive force. This is the primary drag reduction mechanism of the anti-fairing, as explained by Belligoli *et al* [7]. This higher propulsive force would result in obtaining a smaller and smaller pressure drag on the anti-fairing. For the viscous drag, the decrease can be attributed to the two effects of the upstream convex curvature of the anti-fairing discussed in the previous chapter. These are the increase in the approach boundary layer momentum thickness and the decrease of the size and turbulence associated with the HSV. For greater anti-fairing depths, the convex curvature would be increased further resulting in strengthening the two effects, *i.e.* greater increase of momentum thickness and further decrease of the HSV size and turbulence associated with it. Increase in momentum thickness is due to the rise in static pressure for greater anti-fairing depths, as discussed before. Decrease in the turbulent kinetic energy can be associated with the reduction in vertical velocity gradient, which would consequently cause reduction in the turbulence production (refer Equation 3.4). Also, it should be noted that the viscous drag of the anti-fairing results in a continuous decrease in skin friction drag despite the increase in wetted area of the anti-fairing for higher depths. Since both the pressure and viscous drag decreases, the total drag for the anti-fairing reduces for increasing anti-fairing depths.

The combined wing/anti-fairing configuration shows interesting trends. The pressure drag curve has a U-shape with the least drag predicted for the AF_1 case. This means that the decrease in the pressure drag caused by the anti-fairing compensates the continuous increase in the drag over the wing only upto a depth corresponding to AF_1 case. Further increase in depth causes an increase in pressure drag, suggesting the drag increase over the wing overpowers the reduction caused due to anti-fairing. The combined viscous drag behaves differently. There is an initial spike in the plot, which corresponds to AF_0.5 case, after which the drag continuously decreases. Thus it seems that, for AF_0.5 case, the decrease in drag over the anti-fairing couldn't compensate the increased drag caused due to higher wetted area. A further increase in depth seems to provide a net viscous drag reduction. The combined total drag plot seems to follow the trend of the pressure drag curve, by having a minimum at the depth of AF_1 case. This result further corroborates the optimization performed by Belligoli *et al* [7] to arrive at an optimized shape of the anti-fairing.

4.2.2. Effect of different approach boundary layer thicknesses

In this section, the effects of different approach boundary layer thicknesses on the drag reduction capabilities of anti-fairing are discussed. For this analysis, the anti-fairing depth is kept constant, which corresponds to the depth of AF_1 case. As before, different components of drag are separately analyzed to get a clear under-

standing of the flow characteristics. The results are shown in Figure 4.5.

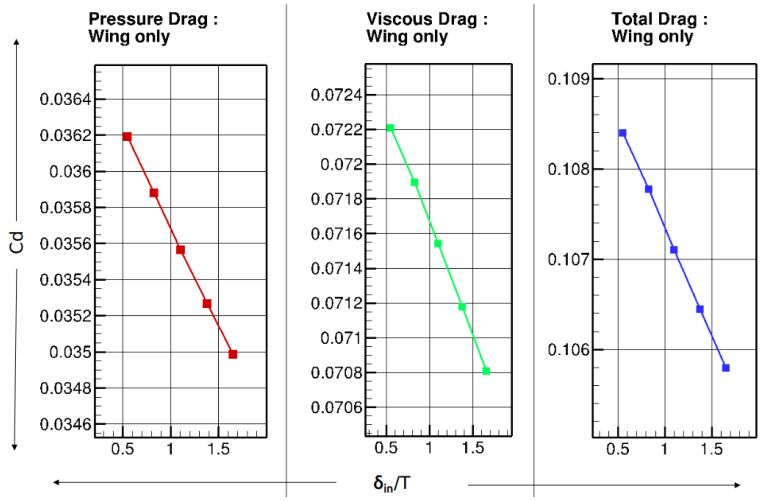

(a)

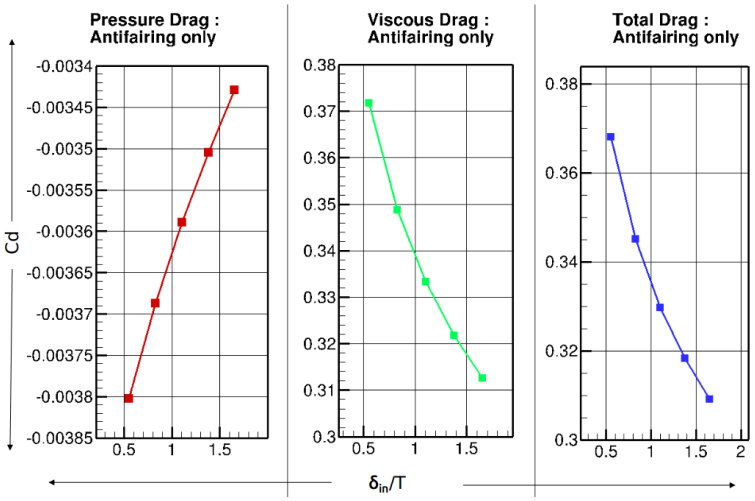

(b)

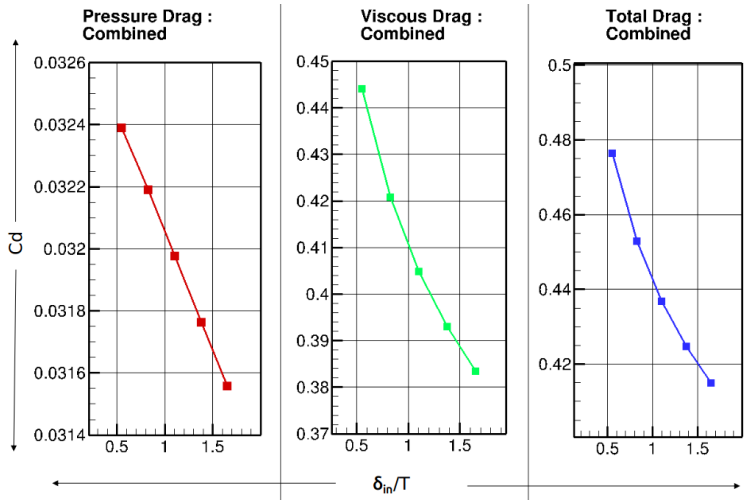

(c)

Figure 4.5: Variation of different components of drag for different approach boundary layer thicknesses

The first plot shows the variation of the drag components over the wing for increasing approach boundary layer thickness. The results are as expected. The viscous drag continuously decreases owing to the decrease in wall shear for higher boundary layer thickness, since the near wall velocity gradient gets reduced. The decrease in viscous drag appears to be linear. The pressure drag variation also follows the trend observed in the viscous drag plots. This linear decrease can be attributed to the fact that a fuller boundary layer would have a smaller momentum thickness or in other words, would have greater momentum associated with the boundary layer. The pressure that is imparted by the flow onto the wing acts by slowing this fluid to zero velocity on the surface of the wing to satisfy the no slip condition. This implies that the surface pressure of the wing is directly proportional to the momentum of the fluid impinging on the surface. Thus, for greater boundary layer thicknesses, lesser is the momentum within the boundary layer, consequently resulting in lesser surface pressure. This is the reason for the decreasing pressure drag on the wing. The story is very similar for the pressure drag of the anti-fairing only case shown in Figure 4.5b. As the boundary layer thickness increases the surface pressure on the anti-fairing reduces due to the lesser momentum. However, this smaller surface pressure would also reduce the propulsive force imparted by the anti-fairing shape, thereby increasing the pressure drag for greater boundary layer thicknesses. However, the increase is not linear as was the case with the wing. The reason for decrease in viscous drag for the anti-fairing could be the same as the reason explained for the decrease observed for the wing. A higher boundary layer thickness implies lesser near wall velocity gradient, and thus lesser friction drag. However, as reported by Fleming *et al* [18], increasing the approach boundary layer thickness increases the MDF (refer Equation 1.2), which would significantly affect the characteristics of the HSV. The vertical extent of the HSV above the wall would reduce and it would be concentrated closer to the near wall region. It is not clear as to how exactly this would affect the viscous drag characteristics of the anti-fairing, but it is believed to be much smaller compared to the reduction obtained by small wall shear. The trend for the total drag in the case of anti-fairing follows the trend of the viscous drag, since the increase in pressure drag is negligible compared to the decrease observed for the viscous drag. The combined drag (Figure 4.5c) plot shows a continuous decrease in both the pressure and viscous drags for greater boundary layer thickness. Interestingly, the decrease in pressure drag follows the trend of the linear decrease observed for the wing, whereas the decrease in viscous drag seems to follow the trend observed for the anti-fairing. Consequently, the total drag for the combined system decreases as well for greater boundary layer thicknesses.

Now that the isolated effects of the variation in approach boundary layer thickness and anti-fairing depths are explained, the total drag obtained for the combined configuration are plotted for all the investigated cases to get an overall picture of the drag variation. This is shown in Figure 4.6.

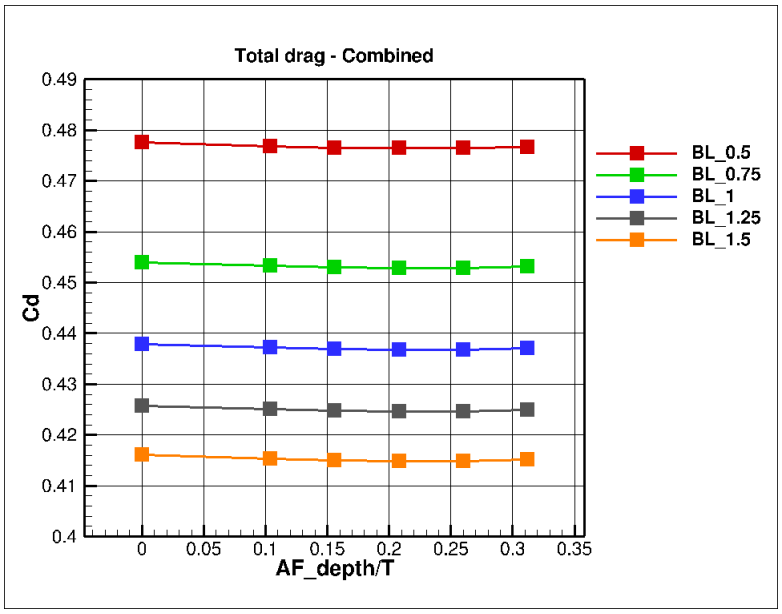

Figure 4.6: Total drag variation of the combined configuration for different anti-fairing depths and boundary layers

It should be noted that each trend shown in the figure follow the same variation observed in Figure 4.4c.

Since all the plots are plotted together, these trends are not apparent. Observing the variations shown above, it is apparent that changing the boundary layer thickness just shifts the line in the vertical direction without any significant effect on the trend of each line. This offset in the trend seems to be directly linked to the value at AF_0 case, *i.e.*, the case with no anti-fairing. This could mean that the effect of the approach boundary layer thickness is more on changing the base drag of the case where no anti-fairing is present, rather than actually affecting the performance of the anti-fairing at different depths. To test this hypothesis, the base drag obtained for $AF_{depth} = 0$ is subtracted from each of the BL cases and these drag differences (ΔCd) are plotted for different depths of anti-fairing. ΔCd is defined as

$$\Delta Cd_{BL_i}^{AF_j} = Cd_{BL_i}^{AF_j} - Cd_{BL_i}^{AF_0},$$

where i signifies the different BL cases (BL_0.5,BL_0.75,BL_1,BL_1.25,BL_1.5) and j signifies different AF cases (AF_0,AF_0.5,AF_0.75,AF_1,AF_1.25,AF_1.5). Figure 4.7 shows the variation of ΔCd for different anti-fairing depths and approach boundary layer thicknesses.

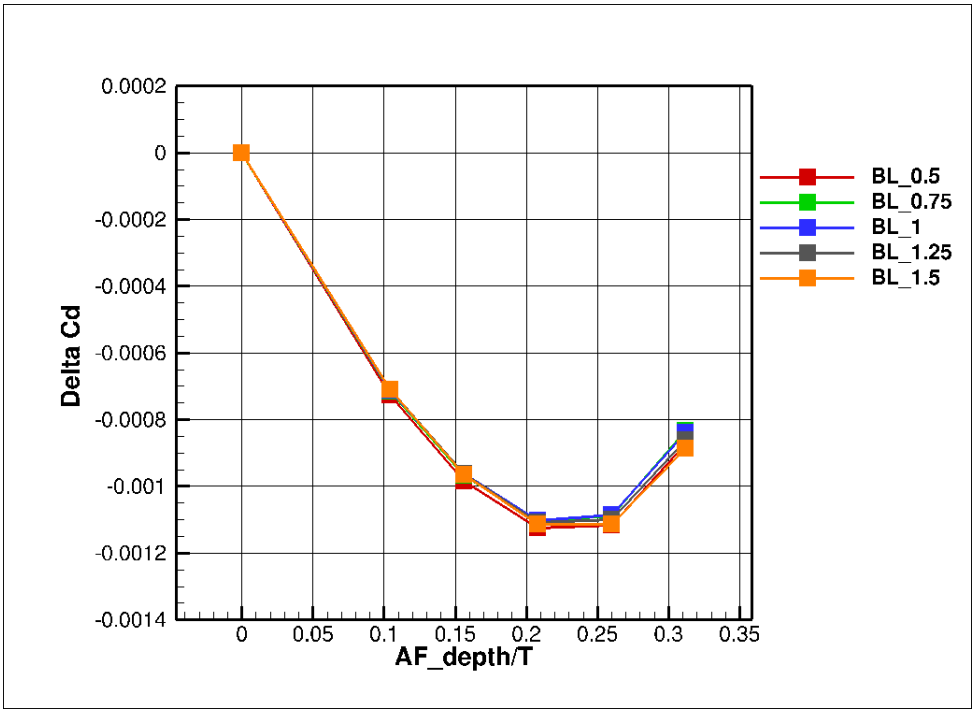

Figure 4.7: Total drag variation of the combined configuration for different anti-fairing depths and boundary layers

The above plot confirms the hypothesis that the approach boundary layer mostly affects the drag value obtained for AF_0 case. Once the drag value corresponding to no anti-fairing case was subtracted, all the lines signifying different approach boundary layer thicknesses fall on top of each other. However, the lines are not completely coincident, as it can be seen that for higher depths of anti-fairing, there seem to be slight differences in ΔCd between various BL cases.

5

Conclusions and recommendations

5.1. Conclusions

Junction flows are an important class of engineering flow phenomena due to their presence in a variety of practical situations. The most important characteristic of these flows is the formation of a unsteady, three-dimensional vortical structure called the horseshoe vortex (HSV). The presence of these in the junction flows result in many undesirable effects such as high turbulence intensities, surface pressure fluctuations and heat transfer rates. In the context of the wing/fuselage junction the HSV induces a specific type of drag called the interference drag, which forms a significant percentage of the total drag of the aircraft. Many scientists and researchers have endeavored to curb the formation of these vortices and subsequently, reduce the interference drag. With regards to that, several conventional methods of drag reduction exist such as use of leading edge fillets, suction, blowing, etc. Recently, aerodynamic shape optimization have been successful in redesigning the shape of the junction region, which would result in a net drag reduction. A similar shape optimization was performed by Belligoli *et al* [7] through which they came up with a new shape for the junction region, called the anti-fairing. This particular shape has shown much promise in terms of the interference drag reduction, as reported in [7, 28, 63]. However, not much information is reported on the effect of the anti-fairing on turbulent quantities in the junction area as well as the shape and size of the HSV. Therefore, the objective of the current thesis was formed to close this gap in the knowledge of the anti-fairing behaviour, given as :

Perform a numerical study of a novel design of wing/body junction, the Anti-Fairing, using Large Eddy Simulations to elucidate the complex turbulent phenomenon involved.

Apart from this main objective, a secondary objective include performing RANS analysis to study the effect of different anti-fairing depths and approach boundary layer thicknesses on the performance of anti-fairing. Thus, the conclusions that have been drawn from achieving these objectives are listed separately for the LES and RANS results in the subsequent pages.

5.1.1. LES results

The results obtained from LES were first validated for the baseline case using the available literature. The parameters used for validation were the upstream boundary layer profiles at specific streamwise locations, mean surface pressure coefficient, mean spanwise vorticity in the symmetry plane and the mean turbulent kinetic energy in the symmetry plane. All these parameters were validated satisfactorily, except for the turbulent kinetic energy, whose magnitude within the HSV was under predicted by the present LES results. After this, the baseline and the anti-fairing cases were compared to discern the differences in various flow parameters. The surface pressure coefficient comparison confirmed the existence of a propulsive force due to the higher upstream pressure in the case of anti-fairing, which would result in lesser drag for the AF case, as proposed by Belligoli *et al.* Comparing the symmetry plane statistics revealed that the presence of anti-fairing significantly reduced the magnitude and size of the HSV and also the mean turbulent kinetic energy associated with it. Specifically, the peak turbulent kinetic energy was reduced by about 40% due to the presence of the anti-fairing. Moreover, the HSV had its centre located further upstream of the wing in the AF case compared to the baseline. Also, the vertical distance of the HSV was reduced in the AF case, since the HSV was concentrated closer to the wall. This behaviour of the HSV in the anti-fairing case was found to be caused by

the convex curvature at the start of the anti-fairing geometry upstream of the wing leading edge. This convex curvature caused two primary effects : it increased the approach boundary layer momentum thickness and also decreased the production of the turbulent kinetic energy within the boundary layer. The turbulence dampening nature of convex curvatures were also reported by many authors [22, 54]. Also, according to Fleming *et al*, the increased momentum thickness would result in higher MDF, for which they observed that the size of the HSV was reduced and the vertical span of the HSV above the wall surface was also lessened. This exact behaviour was observed in the present study as well.

Comparing the flow quantities in streamwise planes around the wing, it was observed that the HSV is pushed further away from the wing in the AF case, similar to the reports of Fleming *et al* [18] for higher MDF. This further corroborated that one of the effects of the anti-fairing is to increase the MDF by increasing the momentum thickness of the incoming boundary layer upstream of the wing. Another interesting observation was the reversal in the trend of higher magnitudes of peak vorticity and mean turbulence quantities for the two cases. Till $X/T = 2.1$, the magnitudes of peak vorticity of the HSV was higher for the BS case, which was analogous to the observation made in the symmetry plane. Downstream of this the peak levels of vorticity got higher for the AF case. As for the mean turbulent kinetic energy, the peak value for AF case reduced till $X/T = 1.4$, after which it slowly started rising and became slightly greater than the baseline case. The exact same trend was also observed for the peak values of Reynolds shear stress. Moreover, a corner separation was predicted for both the cases, which was marked by the formation of the corner vortex. This vortex had comparable magnitude of vorticity as the HSV for a short distance in the wake, before getting dissipated further downstream. The reason for the corner separation prediction was attributed to the use of wall model in the current LES work, although further investigation is required regarding that. The trend reversal and the increase in the turbulence quantities as the HSV traverses around the wing were attributed to the concave dent in the spanwise direction for the anti-fairing. As the HSV moved within this dent, the turbulence seemed to get enhanced, which was marked by the rise in the Reynolds shear stress and the mean turbulent kinetic energy. This was attributed to the fact that unlike convex curvatures, concave curvatures enhanced the turbulent kinetic energy production. Similar behaviour of the concave surfaces were reported in [22, 23, 54] as well. This was also concluded to be the reason for the reversal in the trend of higher peak magnitude of streameise vorticity of the HSV between the two cases. However, the increase in the peak magnitudes of mean turbulent kinetic energy and mean streamwise vorticity were much lesser compared to the reduction observed in the symmetry plane upstream of the wing. Investigations of flow quantities in the wake revealed that the strength of the HSV continued to be greater for the anti-fairing case compared to the baseline. This was an expected behaviour because, once the HSV got out of the dented shape, the mean flow would carry the HSV over a flat surface in both the cases. Thus the magnitude of vorticity would get dissipated at the same rate for the two cases since there are no geometrical differences between them.

Computing drag coefficients using momentum deficit analysis for different wing spans, unphysical, spurious vertical velocities were observed in the wake of the wing for both the cases, above a height of about $Y/T = 0.4$. The magnitude of these vertical velocities were much higher in the AF case. Because of this, the drag analysis couldn't be performed over the entire wing span considered in the domain. Therefore, a smaller span of the wing was chosen, which corresponded to a height of $Y/T = 0.3$, at which the effect of the abnormality was minimal and also, the extent of the HSV was well within this height. Performing the drag analysis at this height gave a total drag reduction of about 1.8% for the anti-fairing. A new parameter called the junction drag coefficient was defined, which would give an estimate of drag only due to the presence of the wing/body junction. Comparing the values of junction drag coefficients for the two cases, it was observed that about 6.8% of junction drag reduction was obtained due to the presence of the anti-fairing. Furthermore, to observe if there existed another mechanism other than the pressure propulsive effect of the anti-fairing, the respective pressure drag contribution was subtracted from the total drag of both the cases and the resultant viscous drag were compared. It was seen that there was a net reduction in the skin friction drag observed for the anti-fairing case, which led to the conclusion that the propulsive pressure effect was aided by another mechanism which was caused by a combination of increase in approach boundary layer momentum thickness and dampening of the turbulence associated with the HSV upstream of the wing. However, the propulsive pressure effect was still found to be the dominant factor in reducing the total drag.

5.1.2. RANS results

The RANS setup was first validated by comparing the results obtained from the RANS simulation of the same Rood wing case used for LES study, with the LES results and RANS results from literature. It was observed that though the location, size and magnitude of vorticity of the HSV were not perfectly captured , satisfactory accuracy was achieved in the boundary layer profile comparison. Moreover, since only integrated loads were going to be compared between the cases, the accuracy of the RANS results were deemed sufficient. After this, the drag reduction capabilities of the anti-fairing for various approach boundary layer thicknesses and anti-fairing depths were compared using the drag coefficients obtained from RANS analysis of NACA 0015 wing/anti-fairing combination. The drag forces were analyzed separately on each wall surface component (wing only, anti-fairing only, wing+anti-fairing) and the effects of approach boundary layer thickness and anti-fairing depth can be summarized as follows :

Increasing the anti-fairing depth,

- Increases the pressure drag over the wing and reduces it over the anti-fairing region, resulting in the presence of a minimum point of pressure drag for the combined system at a particular anti-fairing depth (here at a depth of AF_depth/T = 0.208)
- Increases the viscous drag over the wing and reduces the same over the anti-fairing region, resulting in a slight increase in the combined viscous drag at the smallest anti-fairing depth, above which the combined viscous drag decreases further
- Results in the presence of a minimum point of total drag over the combined system for a particular anti-fairing depth (here at a depth of AF_depth/T = 0.208), due to the combination of above two trends. Results in a similar trend for all the approach boundary layer thicknesses investigated

Increasing the approach boundary layer thickness,

- Decreases both the pressure drag and viscous drag over the wing resulting in a decrease in the total drag
- Increases the pressure drag, while decreasing the viscous drag over the anti-fairing, resulting in an overall decrease in the total drag
- Decreases both the viscous and pressure drag over the combined system, resulting in an overall decrease in total drag
- Does not have any significant effect on the drag reduction capabilities of anti-fairing at different depths

5.2. Recommendations for future work

The following points can be considered for future works on the study of anti-fairing:

- As mentioned various times, wall modeled LES, though gave significantly better results compared to RANS, still had its problems with the prediction of near wall turbulence. Therefore, a wall-resolved LES could be performed for better accuracy in the prediction of junction characteristics
- Due to time constraints, only two parameters (approach boundary layer thickness and anti-fairing depth) were considered for investigating the drag reduction performance of anti-fairing. Therefore, many other parameters can be investigated to ensure that the anti-fairing works for all the cases. These can include different wing thicknesses, wing angle of attack, wing leading edge shapes, flow Mach number
- When the pressure coefficient distribution of the bottom surface was investigated for the anti-fairing case, it was observed that the concave dent downstream of the wing trailing edge resulted had higher pressure compared to the baseline case and also reduced the drag reduction due to the pressure propulsion effect. Therefore, it would be interesting to investigate the performance of an anti-fairing shape without this concave curvature
- Compressible LES could be tried for the same Rood wing/ anti-fairing configuration to see if the spurious vertical velocities that were predicted in the current LES is negated. Moreover, Ryu *et al* [48] had used compressible wall-resolved LES in their investigation of Rood wing/flat plate junction flow

A

Combined drag coefficients - RANS

All the drag coefficients shown below are calculated using Equation 4.1

Table A.1: Overview of combined viscous drag coefficients of all the investigated RANS cases

	BL_0.5	**BL_0.75**	**BL_1**	**BL_1.25**	**BL_1.5**
AF_0	0.444151	0.420783	0.404921	0.392983	0.383445
AF_0.5	0.444158	0.420801	0.404942	0.393004	0.383463
AF_0.75	0.444102	0.420754	0.404901	0.392964	0.383422
AF_1	0.444035	0.420699	0.404847	0.392910	0.383369
AF_1.25	0.443944	0.420625	0.404784	0.392851	0.383311
AF_1.5	0.443855	0.420560	0.404728	0.392799	0.383263

Table A.2: Overview of combined pressuredrag coefficients of all the investigated RANS cases

	BL_0.5	**BL_0.75**	**BL_1**	**BL_1.25**	**BL_1.5**
AF_0	0.033398	0.033209	0.033002	0.032797	0.032595
AF_0.5	0.032663	0.032475	0.032270	0.032066	0.031866
AF_0.75	0.032461	0.032269	0.032059	0.031853	0.031651
AF_1	0.032389	0.032190	0.031975	0.031763	0.031556
AF_1.25	0.032487	0.032279	0.032053	0.031831	0.031616
AF_1.5	0.032822	0.032599	0.032357	0.032120	0.031891

Table A.3: Overview of combined total drag coefficients of all the investigated RANS cases

	BL_0.5	**BL_0.75**	**BL_1**	**BL_1.25**	**BL_1.5**
AF_0	0.47755	0.45399	0.43792	0.42578	0.41604
AF_0.5	0.47682	0.45328	0.43721	0.42507	0.41533
AF_0.75	0.47656	0.45302	0.43696	0.42482	0.41507
AF_1	0.47642	0.45289	0.43682	0.42467	0.41493
AF_1.25	0.47643	0.45290	0.43684	0.42468	0.41493
AF_1.5	0.47668	0.45316	0.43708	0.42492	0.41515

B

Pseudo *MATLAB* code to compute drag using MDA

A *MATLAB* code was used to compute the drag using Momentum Deficit Analysis (MDA) from the LES flow field results. A separate function called *drag()* was defined, to which the flow field results over a single slice are passed in the form of a structure. The function computes the drag contribution of the slice and returns the drag value. Thus, all the slices are passed to this function and the total drag is obtained by summing the contribution of each of these slices. The pseudo-code is shown below.

```
% Slice - flow data in structure format
% n - coordinates of normal to the slice in form (nx,ny,nz)
% rho - Density
% mu - Dynamic viscosity
% Uref, Pref - Refernce velocity and pressure
% Nx, Ny, Nz - Number of cells in the three directions
function[D] = drag(Slice,n,rho,mu,Uref,Pref,Nx,Ny,Nz)

% Coordinates of the vector normal to the slice
nx = n(1); ny = n(2); nz = n(3);

walldist = Slice.data(:,:,24);

x = Slice.data(:,:,1);
y = Slice.data(:,:,2);
z = Slice.data(:,:,3);

u = Slice.data(:,:,4);
v = Slice.data(:,:,5);
w = Slice.data(:,:,6);

p = Slice.data(:,:,7);

% Velocity gradients
dudx = Slice.data(:,:,25);
dudy = Slice.data(:,:,28);
dudz = Slice.data(:,:,31);

dvdx = Slice.data(:,:,26);
dvdy = Slice.data(:,:,29);
dvdz = Slice.data(:,:,32);
```

```
dwdx = Slice.data(:,:,27);
dwdy = Slice.data(:,:,30);
dwdz = Slice.data(:,:,33);

% Turbulent stresses
uu = Slice.data(:,:,8);
uv = Slice.data(:,:,9);
uw = Slice.data(:,:,10);

% Compute the area of cells
if abs(nx)==1

ds = abs(min(min(y))-max(max(y)))/Ny * abs(min(min(z))-max(max(z)))/Nz;

elseif abs(ny)==1

ds = abs(min(min(x))-max(max(x)))/Nx * abs(min(min(z))-max(max(z)))/Nz;

elseif abs(nz)==1

ds = abs(min(min(x))-max(max(x)))/Nx * abs(min(min(y))-max(max(y)))/Ny;

end

% Compute the stresses
tau_xx = mu*2*dudx -rho*uu;
tau_xy = mu*(dudy + dvdx) -rho*uv;
tau_xz = mu*(dudz + dwdx) -rho*uw;

% Compute the drag
D = -sum(sum((rho*(u-Uref).*(u*nx + v*ny + w*nz)...
+ (p-Pref)*nx - tau_xx*nx - tau_xy*ny -...
         tau_xz*nz).*ds));



end
```

Bibliography

[1] ANSYS ICEM CFD brochure. URL `https://www.ansys.com/-/media/Ansys/corporate/resourcelibrary/brochure/ansys-icem-cfd-brochure.pdf`.

[2] NA Adams, S Hickel, and S Franz. Implicit subgrid-scale modeling by adaptive deconvolution. *Journal of Computational Physics*, 200(2):412–431, 2004.

[3] John David Anderson Jr. *Fundamentals of aerodynamics*. Tata McGraw-Hill Education, 2010.

[4] DD Apsley and MA Leschziner. Investigation of advanced turbulence models for the flow in a generic wing-body junction. *Flow, Turbulence and Combustion*, 67(1):25–55, 2001.

[5] TJ Barber. An investigation of strut-wall intersection losses. *Journal of Aircraft*, 15(10):676–681, 1978.

[6] D Barberis, P Molton, and T Malaterre. Control of 3d turbulent boundary layer separation caused by a wing–body junction. *Experimental thermal and fluid science*, 16(1-2):54–63, 1998.

[7] Zeno Belligoli, Annemiek J Koers, Richard P Dwight, and Georg Eitelberg. Using an anti-fairing to reduce drag at wing/body junctions. *AIAA Journal*, pages 1–13, 2018.

[8] Peter Bradshaw. Turbulent secondary flows. *Annual review of fluid mechanics*, 19(1):53–74, 1987.

[9] Joël Brezillon and Richard P Dwight. Applications of a discrete viscous adjoint method for aerodynamic shape optimisation of 3d configurations. *CEAS Aeronautical Journal*, 3(1):25–34, 2012.

[10] LS Caretto, AD Gosman, SV Patankar, and DB Spalding. Two calculation procedures for steady, three-dimensional flows with recirculation. In *Proceedings of the third international conference on numerical methods in fluid mechanics*, pages 60–68. Springer, 1973.

[11] G Castiglioni, JA Domaradzki, V Pasquariello, S Hickel, and M Grilli. Numerical simulations of separated flows at moderate reynolds numbers appropriate for turbine blades and unmanned aero vehicles. *International Journal of Heat and Fluid Flow*, 49:91–99, 2014.

[12] Haecheon Choi and Parviz Moin. Grid-point requirements for large eddy simulation: Chapman's estimates revisited. *Physics of fluids*, 24(1):011702, 2012.

[13] Richard Courant, Kurt Friedrichs, and Hans Lewy. On the partial difference equations of mathematical physics. *IBM journal of Research and Development*, 11(2):215–234, 1967.

[14] William J Devenport and Roger L Simpson. Time-depeiident and time-averaged turbulence structure near the nose of a wing-body junction. *Journal of Fluid Mechanics*, 210:23–55, 1990.

[15] William J Devenport, Roger L Simpson, Michael B Dewitz, and Naval K Agarwal. Effects of a leading-edge fillet on the flow past an appendage-body junction. *AIAA journal*, 30(9):2177–2183, 1992.

[16] Nitin S Dhamankar, Gregory A Blaisdell, and Anastasios S Lyrintzis. An overview of turbulent inflow boundary conditions for large eddy simulations. In *22nd AIAA computational fluid dynamics conference*, page 3213, 2015.

[17] F Ducros, F Nicoud, and T Poinsot. Wall-adapting local eddy-viscosity models for simulations in complex geometries. *Numerical Methods for Fluid Dynamics VI*, pages 293–299, 1998.

[18] Jonathan Lee Fleming, RL Simpson, JE Cowling, and WJ Devenport. An experimental study of a turbulent wing-body junction and wake flow. *Experiments in fluids*, 14(5):366–378, 1993.

[19] Song Fu, Zhixiang Xiao, Haixin Chen, Yufei Zhang, and Jingbo Huang. Simulation of wing-body junction flows with hybrid rans/les methods. *International Journal of Heat and Fluid Flow*, 28(6):1379–1390, 2007.

[20] Fabien Gand, Sébastien Deck, Vincent Brunet, and Pierre Sagaut. Flow dynamics past a simplified wing body junction. *Physics of Fluids*, 22(11):115111, 2010.

[21] Massimo Germano, Ugo Piomelli, Parviz Moin, and William H Cabot. A dynamic subgrid-scale eddy viscosity model. *Physics of Fluids A: Fluid Dynamics*, 3(7):1760–1765, 1991.

[22] MM Gibson, WP Jones, and BA Younis. Calculation of turbulent boundary layers on curved surfaces. *The Physics of Fluids*, 24(3):386–395, 1981.

[23] PH Hoffmann, KC Muck, and P Bradshaw. The effect of concave surface curvature on turbulent boundary layers. *Journal of Fluid mechanics*, 161:371–403, 1985.

[24] RF Huang, CM Hsu, and C Chen. Effects of an upstream tetrahedron on the circular cylinder–flat plate juncture flow. *Experiments in Fluids*, 56(7):146, 2015.

[25] M Johnson, K Ravindra, and R Andres. Comparative study of the elimination of the wing fuselage junction vortex by boundary layer suction and blowing. In *32nd Aerospace Sciences Meeting and Exhibit*, page 293, 1994.

[26] Khalil A Kairouz and Hamid R Rahai. Turbulent junction flow with an upstream ribbed surface. *International journal of heat and fluid flow*, 26(5):771–779, 2005.

[27] KJ Kang, T Kim, and SJ Song. Strengths of horseshoe vortices around a circular cylinder with an upstream cavity. *Journal of mechanical science and technology*, 23(7):1773–1778, 2009.

[28] Annemiek J. Koers. The Anti-Fairing:Reducing Drag in Junction Flows. Master's thesis, TU Delft, 2017.

[29] L Kubendran, A Bar-Sever, and W Harvey. Flow control in a wing/fuselage-type juncture. In *26th Aerospace Sciences Meeting*, page 614, 1988.

[30] LR Kubendran, H McMahon, and JE Hubbartt. Interference drag in a simulated wing-fuselage juncture. 1984.

[31] E Lenormand, P Sagaut, L Ta Phuoc, and P Comte. Subgrid-scale models for large-eddy simulations of compressible wall bounded flows. *AIAA journal*, 38(8):1340–1350, 2000.

[32] Thomas S Lund, Xiaohua Wu, and Kyle D Squires. Generation of turbulent inflow data for spatially-developing boundary layer simulations. *Journal of computational physics*, 140(2):233–258, 1998.

[33] Zhoujie Lyu and Joaquim RRA Martins. Aerodynamic design optimization studies of a blended-wing-body aircraft. *Journal of Aircraft*, 51(5):1604–1617, 2014.

[34] BW McCormick. Aerodynamics aeronautics and flight mechanics john wiley & sons inc, 1995.

[35] Florian R Menter, Martin Kuntz, and Robin Langtry. Ten years of industrial experience with the sst turbulence model. *Turbulence, heat and mass transfer*, 4(1):625–632, 2003.

[36] M Meyer, S Hickel, and NA Adams. Computational aspects of implicit les of complex flows. In *High Performance Computing in Science and Engineering, Garching/Munich 2009*, pages 133–146. Springer, 2010.

[37] Marcel Meyer, A Devesa, Stefan Hickel, XY Hu, and Nikolaus A Adams. A conservative immersed interface method for large-eddy simulation of incompressible flows. *Journal of Computational Physics*, 229 (18):6300–6317, 2010.

[38] Robert D Moser, John Kim, and Nagi N Mansour. Direct numerical simulation of turbulent channel flow up to re τ= 590. *Physics of fluids*, 11(4):943–945, 1999.

[39] Hideaki Mouri, Masanori Takaoka, Akihiro Hori, and Yoshihide Kawashima. Probability density function of turbulent velocity fluctuations. *Physical Review E*, 65(5):056304, 2002.

[40] KC Muck, PH Hoffmann, and P Bradshaw. The effect of convex surface curvature on turbulent boundary layers. *Journal of Fluid Mechanics*, 161:347–369, 1985.

[41] Semih M Olcmen and Roger L Simpson. Influence of wing shapes on surface pressure fluctuations at wing-body junctions. *AIAA journal*, 32(1):6–15, 1994.

[42] Joongcheol Paik, Cristian Escauriaza, and Fotis Sotiropoulos. On the bimodal dynamics of the turbulent horseshoe vortex system in a wing-body junction. *Physics of Fluids*, 19(4):045107, 2007.

[43] Sergey Peigin and Boris Epstein. Aerodynamic optimization of essentially three-dimensional shapes for wing-body fairing. *AIAA journal*, 46(7):1814–1825, 2008.

[44] DB Philips, John Michael Cimbala, and AL Treaster. Suppression of the wing-body junction vortex by body surface suction. *Journal of aircraft*, 29(1):118–122, 1992.

[45] Stephen B Pope. Turbulent flows, 2001.

[46] PE Roach and JT Turner. Secondary loss generation by gas turbine support struts. *International journal of heat and fluid flow*, 6(2):79–88, 1985.

[47] Patrick J Roache. Perspective: a method for uniform reporting of grid refinement studies. *Journal of Fluids Engineering*, 116(3):405–413, 1994.

[48] Sungmin Ryu, Michael Emory, Gianluca Iaccarino, Alejandro Campos, and Karthik Duraisamy. Large-eddy simulation of a wing–body junction flow. *AIAA Journal*, 54(3):793–804, 2016.

[49] Pierre Sagaut. *Large eddy simulation for incompressible flows: an introduction*. Springer Science & Business Media, 2006.

[50] Daisuke Sasaki, Guowei Yang, and Shigeru Obayashi. Automated aerodynamic optimization system for sst wing-body configuration. *Transactions of the Japan Society for Aeronautical and Space sciences*, 46 (154):230–237, 2004.

[51] CV Seal and CR Smith. The control of turbulent end-wall boundary layers using surface suction. *Experiments in Fluids*, 27(6):484–496, 1999.

[52] Tsan-Hsing Shih, Louis A Povinelli, and Nan-Suey Liu. Application of generalized wall function for complex turbulent flows. In *Engineering Turbulence Modelling and Experiments 5*, pages 177–186. Elsevier, 2002.

[53] Roger L Simpson. Junction flows. *Annual Review of Fluid Mechanics*, 33(1):415–443, 2001.

[54] Alexander J Smits, STB Young, and Peter Bradshaw. The effect of short regions of high surface curvature on turbulent boundary layers. *Journal of Fluid Mechanics*, 94(2):209–242, 1979.

[55] Wenbin Song and Peipei Lv. Two-level wing-body-fairing optimization of a civil transport aircraft. *Journal of Aircraft*, 48(6):2114–2121, 2011.

[56] Philippe R Spalart. Direct simulation of a turbulent boundary layer up to r θ= 1410. *Journal of fluid mechanics*, 187:61–98, 1988.

[57] Philippe R Spalart. Detached-eddy simulation. *Annual review of fluid mechanics*, 41:181–202, 2009.

[58] DB Spalding. A single formula for the "law of the wall". *Journal of Applied Mechanics*, 28(3):455–458, 1961.

[59] Bas W Van Oudheusden, Casper B Steenaert, and Loek M M. Boermans. Attachment-line approach for design of a wing-body leading-edge fairing. *Journal of aircraft*, 41(2):238–246, 2004.

[60] Bas W Van Oudheusden, Fulvio Scarano, Eric WM Roosenboom, Eric WF Casimiri, and Louis J Souverein. Evaluation of integral forces and pressure fields from planar velocimetry data for incompressible and compressible flows. *Experiments in Fluids*, 43(2-3):153–162, 2007.

[61] Bert Vreman, Bernard Geurts, and Hans Kuerten. Large-eddy simulation of the temporal mixing layer using the clark model. *Theoretical and computational fluid dynamics*, 8(4):309–324, 1996.

[62] Shenren Xu, Sebastian Timme, Orest Mykhaskiv, and Jens-Dominik Müller. Wing-body junction optimisation with cad-based parametrisation including a moving intersection. *Aerospace Science and Technology*, 68:543–551, 2017.

[63] Ka Hin Yeung. Characterization of junction flow under the influence of passive flow control devices. Master's thesis, TU Delft, 2017.

[64] Christian Zwerger, Stefan Hickel, Christian Breitsamter, and Nikolaus Adams. Wall modeled large eddy simulation of the vfe-2 delta wing. In *33rd AIAA Applied Aerodynamics Conference*, page 2572, 2015.